

**Towards Efficient MXene-based
Electrocatalysts for Electrochemical
CO₂ Reduction**



Samuel Thompson Robertshaw

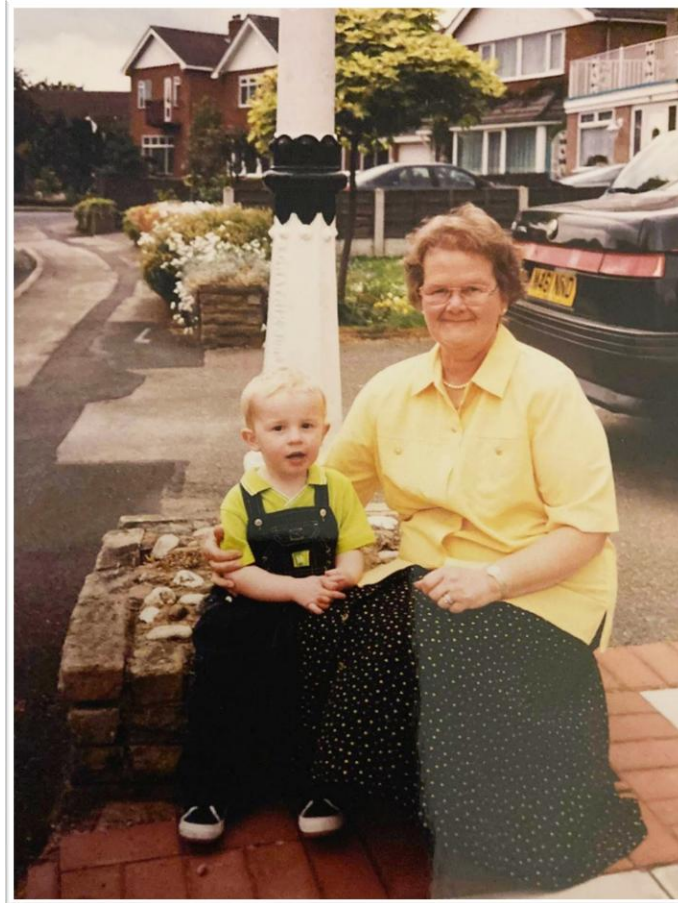
**This dissertation is submitted for the degree of Doctor of
Philosophy**

March 2025

Department of Chemistry

Dedication

This thesis is lovingly dedicated to the memory of my Grandma



Joan Campbell

1937 - 2006

Declaration

This thesis has not been submitted in support of an application for another degree at this or any other university. It is the result of my own work and includes nothing that is the outcome of work done in collaboration except where specifically indicated. Many of the ideas in this thesis were the product of discussion with my supervisor Dr Kathryn Toghill. Dr Hamza Annath assisted in the acquisition of experimental results in chapter 3. Dr Luis Pinho assisted in the acquisition of experimental results in chapters 3 and 4. Dr Daniel Smith assisted in the acquisition of experimental results in chapter 5.

Samuel Robertshaw, MChem

Lancaster University, UK

Abstract

The increased utilisation of non-renewable energy sources in recent decades has had a drastic impact on the Earth's climate. With significant anthropogenic carbon dioxide (CO₂) emissions causing drastic changes to the Earth's atmosphere, the decarbonisation of energy generation alongside renewable energy alternatives to fossil fuels is crucial. The electrocatalytic reduction of CO₂ (eCO₂RR) to value-added chemicals is an attractive and sustainable technology towards achieving a low-carbon economy. However, current electrocatalysts have been reported to suffer from low selectivity, poor stability, and high overpotentials, thus limiting their scale-up potential. There is a critical demand for the development of efficient novel electrocatalysts with high selectivity towards desired products. A new class of 2-dimensional materials known as MXenes has gained significant interest in the recent literature due to their unique structural and electronic properties. Several computational studies have highlighted Ti₃C₂T_x to be of significant interest as an eCO₂RR electrocatalyst. This thesis works towards evaluating Ti₃C₂T_x for the application of eCO₂RR catalysis, with a particular focus on the fabrication of MXene-modified electrodes using MXene powders. Additionally, the treatment and handling of Ti₃C₂T_x powders is reported herein, with the successful -O and -OH surface functionalisation of a commercial MXene also demonstrated via ozone modifications. Finally, the design and manufacture of bespoke electrochemical cells is reported, with the aim of accommodating a wealth of electrode morphologies while simultaneously optimising and improving current systems for accurate eCO₂RR product quantification.

Acknowledgements

First, I would like to thank my supervisor Professor Kathryn Toghil (Kass) for her support throughout this PhD. Your knowledge and guidance has been invaluable when navigating the novel world of MXenes. You have afforded me so many opportunities to grow as a scientist and as a person, for which I will be forever grateful. I would also like to thank Dr Luis Pinho, Dr Hamza Annath, and Dr Daniel Smith for their support and friendship. It has been a pleasure working with you all day-to-day, and I will truly miss the blaring of Bach and Shaun the Sheep throughout the lab. Dr Pinho, may you never be allowed the AUX cable again. Finally, I would like to thank all members, past and present, of the Toghil Group for providing such an enjoyable and collaborative environment to work in.

I would like to express my gratitude to Dr Nuno Bimbo for being invaluable in the procurement of MXenes, your contributions are greatly appreciated. This gratitude extends to his previous students, Dr Luc Bouscarrat and Dr Phil Maughan. I would like to thank also the Lancaster University Physics workshop for always sharing their time and expertise.

I would especially like to thank my family. Mum, Dad, Grandpa and Lesley, thank you all for your support and love throughout my journey as a scientist. You have always been my biggest cheerleaders, and so I thank you from the bottom of my heart.

My heartfelt thanks also extend to the Roberts family, diolch i chi gyd.

Finally, to my wonderful girlfriend Rhodd. Words cannot express my gratitude, but I will try my best. Diolch, Rhodd, am fod fy ynys o lonyddwch yn ganol môr garw. Mae dy gariad a dy gefnogaeth wedi fy ysbrydoli i lwyddo mewn pethnau ni allwn i feddwl bosib. Diolch am dy amynedd ddi ben drawa' adegau nad oeddwn yn ei haeddu. Ond yn fwy na dim diolch i chdi am fod yn chdi. Allwn i ddim gwneud hyn hebdat.

Thank you to the Department of Chemistry at Lancaster University and the funding bodies for this work.

Thank you for reading.

Contents

1	Introduction	1
1.1	Carbon Capture and Utilisation (CCU)	2
1.1.1	CO ₂ Capture.....	2
1.1.2	CO ₂ Conversion.....	3
1.1.2.1	Photocatalytic	3
1.1.2.2	Electrochemical.....	3
1.2	MXenes and MAX Phase - $M_{n+1}AX_n$.....	7
1.2.1	Acidic Etching of Ti ₃ AlC ₂ to Ti ₃ C ₂ MXene.....	8
1.2.3	MXene Synthesis – Acidic Etching	9
1.2.4	Hydrofluoric Acid-Free Synthesis of MXenes.....	10
1.2.5	Effects of Synthetic Methods on the Structure of MXenes	11
1.2.6	Surface Chemistry	11
1.2.7	Storage Conditions	12
1.2.8	Properties of MXenes	14
1.2.8.1	Electronic Properties.....	14
1.2.8.2	Mechanical Properties.....	15
1.2.9	Characterisation of MXenes	15
1.2.10	Intercalation and Delamination	16
1.3	MXenes in Electrochemistry.....	17
1.3.1	MXenes in Reduction Reactions.....	18
1.3.1.1	MXenes for CO ₂ RR.....	19
1.3.1.2	The ‘Copper’ Standard.....	22
1.4	Commercial MXenes	23
1.5	Thesis Scope.....	24
2	Materials, and Theory	25
2.1	Material Characterisation Techniques.....	25
2.1.1	Powder X-ray diffraction (XRD)	25
2.1.2	X-ray photoelectron spectroscopy (XPS).....	26
2.1.3	Raman Spectroscopy	26
2.1.4	Scanning Electron Microscopy	27
2.1.5	Surface Area Analysis – Gas Sorption	27
2.1.6	Thermogravimetric Analysis/Differential Scanning Calorimetry.....	28

2.2	Electrochemical Characterisation Techniques	28
2.2.1	Linear and Cyclic Voltammetry	29
2.2.3	Chronoamperometry	30
2.3	Product Analysis Techniques	31
2.3.1	Gas Chromatography	31
2.4	MXenes Samples	31
3	Max Phase and MXenes	35
3.1	Introduction.....	35
3.1.1	Ti ₃ AlC ₂ MAX Phase	35
3.1.2	Ti ₃ C ₂ MXene Synthesis and Surface Functionalisation	37
3.2	Materials and Methods.....	39
3.2.1	Reagents and Experiments	39
3.2.2	MAX Phase Synthesis	39
3.2.2.1	Maughan Method	39
3.2.2.2	Barsoum Method.....	40
3.2.3	Acidic Etching of Ti ₃ AlC ₂ to Ti ₃ C ₂ T _x via <i>in-situ</i> HF generation	40
3.2.4	Fluorine-Free Synthesis of Ti ₃ C ₂ OH.....	40
3.2.5	Surface Functionalisation of Ti ₃ C ₂ T _x	41
3.2.5.1	Acidic and Alkaline Treatments	41
3.2.5.2	Wet Ozone Treatment	41
3.2.5.3	Dry Ozone Treatment.....	41
3.3	Results and Discussion.....	42
3.3.1	MAX Phase Synthesis	42
3.3.2	Acidic Etching of Ti ₃ AlC ₂ to Ti ₃ C ₂ T _x via <i>in-situ</i> HF generation	51
3.3.3	Fluorine-Free Synthesis of Ti ₃ C ₂ T _{0,0H}	55
3.3.4	MXene Surface Functionalisation	60
3.3.4.1	Acid and Alkali Treatment of Ti ₃ C ₂ T _x	60
3.3.4.2	Ozone Treatments for -O and -OH Functionalisation.....	62
3.4	Conclusions	67
4	MXene Delamination and Electrode Modification	70
4.1	Introduction.....	70
4.1.1	Delamination and Intercalation	71
4.1.2	Electrode Fabrication.....	72
4.1.3	Electropolymerisation of EDOT	74

4.2	Materials and Methods	77
4.3	Results and Discussion	79
4.3.1	Delamination of $Ti_3C_2T_x$ and Intercalation.....	79
4.3.2	Drop Casting	83
4.3.3	Free-standing MXene Film	90
4.3.4	Electropolymerisation of EDOT	92
4.5	Conclusions	96
5	CO₂RR Electrochemical Cell Design	98
5.1	Introduction	98
5.2	Materials and Methods	101
5.2.1	Reagents and Equipment.....	101
5.3	Results and Discussion	102
5.3.1	3-Electrode Cell for Catalyst Evaluation	102
5.3.1.1	Design and Rationale	102
5.3.1.2	Prototyping.....	103
5.3.1.3	Assembly and Operation	103
5.3.1.4	Preliminary Results.....	104
5.3.2	Batch Electrolysis Cell for CO ₂ RR	107
5.3.2.1	Design and Rationale	107
5.3.2.2	Design Iteration 1. – Downstream Collection Vessel (DCV).....	107
5.3.2.3	Design Iteration 2. – Zero-Headspace Electrolysis Cell 1 (ZHEC1).....	111
5.3.2.4	Design Iteration 3. – Zero-Headspace Collection Vessel 2 (ZHEC2).....	114
5.4.2.5	Preliminary Batch Electrolysis Testing	117
5.4	Conclusions	119
6	Conclusions	121
6.1	Summary	121
6.2	Retrospectives	122
6.3	Future Work	123
	References	126

List of Tables

Table 1.1 Carbon Dioxide reduction standard electrochemical potentials at pH 7.0 vs SHE ¹⁴	4
Table 2.1 – Calculated specific surface areas via BET N ₂ sorption measurements..	33
Table 4.1– A table comparing the associated cost of SSE and DSE electropolymerisation experiments.....	77
Table 4.2 – Nafion binder amount evaluation	85
Table 4.3 – Drop cast volume evaluation using Nafion binder	85
Table 4.4 – PEDOT:PSS binder evaluation	88

List of Figures

Figure 1.1 Monthly Atmospheric Carbon Dioxide Concentration (ppm) Mar 1958-Apr 2024 at Mauna Loa Observatory, Hawaii; obtained from Scripps Institution of Oceanography at UC San Diego ¹	1
Figure 1.2 - Crystal structure of a M_3AX_2 MAX phase from a (a) perspective view (b) side view (c) top-down view, showing alternating layers of M_6X octahedra and A elements.....	8
Figure 1.3 Schematic representation of MXene synthesis via in-situ HF generation.	9
Figure 1.4 - Graphical data a) Publications by keyword, i) 'MXene' ii) 'MXene' [Cat: Energy Fuels] iii) 'MXene CO ₂ Reduction. b) MXene papers to date by Web of Science categories .	18
Figure 2.1 - Cyclic voltammogram of a quasi-reversible redox couple	29
Figure 2.2 – SEM images of $Ti_3C_2T_x^{PM}$ at a) x 15,000 b) x 20,000.....	32
Figure 2.3 – SEM images of $Ti_3C_2T_x^{NB}$ at a) x 1,600 b) x 3,700	33
Figure 2.4 – SEM images of a commercial $Ti_3C_2T_x^{CM}$ powder MXene at a) x 1,100 b) x 1,600 c) 2,000 d) x 3,300.....	34
Figure 3.1 – SEM Images of 1) M-MAX at a) x5000 b) x15,000 2) B-MAX at a) x 5000 b) x1000	42
Figure 3.2 - EDX Analysis of Ti_3AlC_2 [M-MAX] a) Al, C, and Ti (Combined), b) aluminium, c) carbon, d) titanium. Scale bars represent 25 μm	44
Figure 3.3 - EDX Analysis of Ti_3AlC_2 [B-MAX] a) Al, Ti, and C (Combined), b) aluminium, c) titanium, d) carbon. Scale bars represent 25 μm	45
Figure 3.4 - XRD diffraction pattern for a) red - Ti_3AlC_2 [B-MAX], b) black – Ti_3AlC_2 [M-MAX]	46

Figure 3.5 – Elemental composition of the surface oxide layer post-synthesis, MAX phase [Maughan method, 1350 °C]. Inset – Image of Maughan method MAX phase following calcination.....	48
Figure 3.6– XRD diffraction patterns for a) red - $Ti_3AlC_2^{1350}$ b) black - $Ti_3AlC_2^{CU}$	49
Figure 3.7 – SEM Images of 1) $Ti_3AlC_2^{1350}$ at magnification of a) $\times 10,000$ b) $\times 25,000$, and 2) $Ti_3AlC_2^{CU}$ at magnification of a) $\times 5,000$ b) $\times 10,000$	50
Figure 3.8 - TGA/DSC Curves for 1) $Ti_3AlC_2^{1350}$ a) TGA – Green b) DSC – Blue and 2) $Ti_3AlC_2^{CU}$ a) TGA – Red b) DSC – Purple.....	51
Figure 3.9 – SEM Images of 1) $Ti_3C_2T_x$ 1 st synthesis at a) $\times 3,700$ b) $\times 12,000$, and 2) $Ti_3C_2T_x$ 2 nd synthesis at a) $\times 3,700$ b) $\times 4,300$	52
Figure 3.10 – XRD diffraction patterns of a) top – $Ti_3C_2T_x^{NB}$, b) middle – $Ti_3C_2T_x$ (LiF + HCl), c) bottom – Ti_3AlC_2 MAX Phase.....	54
Figure 3.11– XRD diffraction patterns of a) top - $Ti_3C_2T_x^{NB}$, b) middle - $Ti_3C_2T_{0,OH}$ c) bottom - Ti_3AlC_2 MAX phase	56
Figure 3.12 – XRD diffraction patterns of $Ti_3C_2T_{0,OH}$ dried in a) top - static air oven, b) bottom - vacuum oven.....	58
Figure 3.13 - XRD Diffraction patterns of $Ti_3C_2T_{0,OH}$ synthesised with a soaking time of a) black – 4 hours, b) red – 8 hours, c) blue – 12 hours, d) 24 hours	59
Figure 3.14 – Photographs depicting the alkaline and subsequent acidic treatment of $Ti_3C_2T_x$ to yield -O and -OH terminations respectively	61
Figure 3.15– Raman Spectroscopy patterns for a) Untreated $Ti_3C_2T_x$ b) wet ozone treated Ti_3C_2 c) dry ozone treated Ti_3C_2	63
Figure 3.16 – High resolution (a) survey, (b) F 1s, (c) Cl 2p, (d) O 1s XPS spectra of (1) $Ti_3C_2T_x$, (2) dry ozone-treated Ti_3C_2	66
Figure 3.17 – X-ray diffraction patterns for a) black - $Ti_3C_2T_x$ MXene b) red - Ti_3C_2 -Ozone	67

Figure 4.1– Schematic showing Li ⁺ ion intercalation between ML-MXenes.....	72
Figure 4.2 – Schematic showing the drop casting of catalyst particles on an electrode culminating in the coffee ring effect.....	73
Figure 4.3 – Reaction scheme of the electropolymerisation of EDOT to PEDOT	75
Figure 4.4 – Settling times of a) black - Ti ₃ C ₂ T _x b) red- DMSO-intercalated Ti ₃ C ₂ T _x inks as a function of agitation time.....	81
Figure 4.5 – Settling times of various Ti ₃ C ₂ T _x inks as a function of the delamination method.....	83
Figure 4.6 – Aqueous Ti ₃ C ₂ T _x dispersion following EtOH addition.....	86
Figure 4.7 – Nafion/Ti ₃ C ₂ T _x modified GCE electrodes with a) 5 μL of Nafion drop cast layer b) 50% Nafion solution.....	88
Figure 4.8 – SEM images of a) Nafion(500 μL/mL)/MXene-modified electrode, x 270 b) PEDOT:PSS(100 μL/mL)/MXene-modified electrode, x 500)	89
Figure 4.9 – Images of the washing of a vacuum-filtered Ti ₃ C ₂ T _x MXene film.....	91
Figure 4.10 – Bespoke electropolymerisation cell with a glassy carbon electrode (red), Ag/Ag ⁺ reference (blue), and Pt counter electrode (black).....	92
Figure 4.11 - Chronoamperogram of electropolymerised PEDOT for 480s in MeCN on a) black – Glassy carbon electrode, b) red – Ti ₃ C ₂ T _x -modified GCE.....	93
Figure 4.12– Images of the electropolymerised PEDOT/MXene-modified GCE a) before washing with water b) after washing with water	94
Figure 4.13 – SEM images of an electropolymerised PEDOT/MXene-modified glassy carbon electrode at a) ×150 b) × 1,000 c) × 4,300 d) × 3,300.....	95
Figure 5.1 - [Left] Traditional three-electrode cell with a Pt counter electrode, Ag/AgCl reference electrode, and glassy carbon working electrode [Right] Glassy carbon electrode (GCE) surface	98

Figure 5.2 - 3D render of a bespoke 3-electrode electrochemical cell modelled in Fusion360.....	102
Figure 5.3 - Cyclic voltammogram of $[\text{Ru}(\text{NH}_3)_6]^{3+/2+}$ in 0.1 M KHCO_3 , scan rate of 100 mV/s.....	104
Figure 5.4 – Cyclic voltammogram of a) black – bare glassy carbon electrode b) red – Nafion-modified GCE c) blue – $\text{Ti}_3\text{C}_2\text{T}_x$ /Nafion-modified GCE	105
Figure 5.5 – [Left] Cyclic voltammogram of $[\text{Ru}(\text{NH}_3)_6]^{3+/2+}$ in 0.1 M KHCO_3 , scan rate of 100 mV/s. [Right] Image of fully assembled redesigned 3-electrode cell ..	106
Figure 5.6 – 3D render of the downstream collection vessel (DVC) modelled in Fusion360.....	111
Figure 5.7 - 3D render of working compartment open view with electrode positions a) side-mounted [red] b) back-mounted [green] modelled in Fusion360	113
Figure 5.8 - 3D render of a photopolymer resin printed support bracket modelled in Fusion360.....	114
Figure 5.9 – Gas-tightness calibration of ZHEC2 over 120 minutes using i) carbon dioxide ii) nitrogen ii) calibration gas.....	115
Figure 5.10 – 3D render of ZHEC2 modelled in Fusion360	117
Figure 5.11 – Gas chromatograms for CO_2RR at -1.8 V (Ag/AgCl) for 60 minutes on a $\text{Ti}_3\text{C}_2\text{T}_x$ /Nafion-modified sigracell electrode using a) top - Glass electrolysis cell [Inset] – Image of a traditional electrolysis H-cell. b) bottom – ZHEC2 [Inset] – Image of fully assembled ZHEC2	118

List of Abbreviations and Acronyms

Acronym / Abbreviation	Definition
3EC	3-Electrode Cell
AEM	Anion Exchange Membrane
BID	Barrier Discharge Ionisation Detector
CE	Counter Electrode
CEC	Counter Electrode Compartment
CCU	Carbon Capture and Utilisation
CV	Cyclic Voltammetry/Voltammogram
COF	Covalent Organic Framework
DCV	Downstream Collection Vessel
DFT	Density Functional Theory
DSE	Dual-Step Electropolymerisation
EDOT	3,4-ethylenedioxythiophene
EDX	Energy-Dispersive X-ray Spectroscopy
eCO ₂ RR	Electrochemical Carbon Dioxide Reduction Reaction
EPOL	Electropolymerisation
FL-MXenes	Few-Layer MXenes
FSMF	Free-Standing Film Electrode
g-C ₃ N ₄	Graphitic Carbon Nitride
GC	Gas Chromatography
GCE	Glassy Carbon Electrode
GCC	Gas Collection Compartment
HCOOH	Formic Acid
HER	Hydrogen Evolution Reaction
HF	Hydrofluoric Acid
SHE	Standard Hydrogen Electrode
LIB	Lithium-Ion Battery
LSV	Linear Sweep Voltammetry
MILD	Minimally Intensive Layer Delamination
ML-MXenes	Multi-Layer MXenes
MOF	Metal Organic Framework
MEA	Monoethanolamine

N ₂ RR	Nitrogen Reduction Reaction
PEDOT	poly(3,4-ethylenedioxythiophene)
PEM	Proton Exchange Membrane
PEEK	Polyether Ether Ketone
PPM	Parts Per Million
PSS	Polystyrene Sulfonate
RE	Reference Electrode
RHE	Reversible Hydrogen Electrode
SAC	Single Atom Catalysts
SEM	Scanning Electron Microscopy
SSE	Single-Step Electropolymerisation
TCD	Thermal Conductivity Detector
VDW	Van der Waals
V _{ti}	Titanium Vacancy Defect
WE	Working Electrode
WEC	Working Electrode Compartment
XRD	X-ray Diffraction
ZHEC1	Zero-Headspace Electrochemical Cell (1st Iteration)
ZHEC2	Zero-Headspace Electrochemical Cell (2nd Iteration)

1 Introduction

Since the Industrial Revolution, a huge reliance on non-renewable energy sources has seen an unprecedented impact on the earth's climate. With over 80% of the global energy use being sourced from the combustion of fossil fuels, atmospheric CO₂ levels have increased by more than 50% in the last 2 centuries, reaching a record high of over 428 ppm at the Mauna Loa Observatory in April 2024.¹ Annual atmospheric CO₂ concentration data obtained from Scripps Institution of Oceanography at UC San Diego¹ is plotted in Figure 1.1.

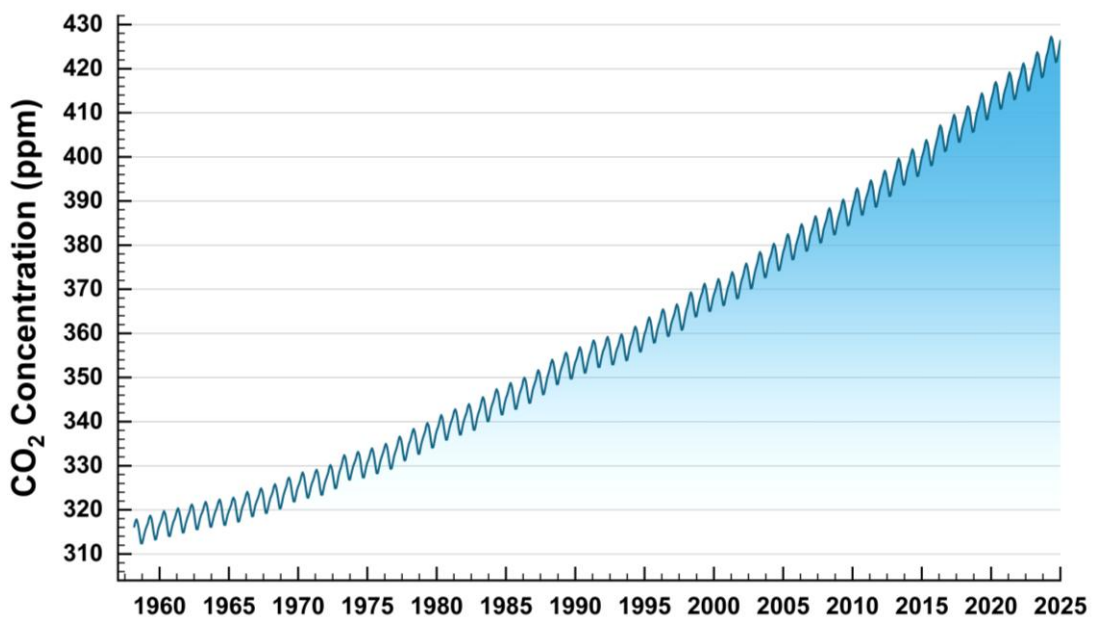


Figure 1.1 Monthly Atmospheric Carbon Dioxide Concentration (ppm) Mar 1958- Apr 2024 at Mauna Loa Observatory, Hawaii

In 2015, the UN Climate Change Conference (COP21) was held in Paris, France which gathered 196 parties from across the globe with the aim of tackling climate change via the newly drawn 'Paris Agreement'.² The legally binding international treaty detailed goals of limiting the average global temperature to well below 2 °C above

pre-industrial levels, with further challenges to limit to only 1.5 °C above pre-industrial levels.

Following the international treaty, increased efforts have been made globally to move towards the decarbonisation of energy generation via the utilisation of renewable energy in place of fossil fuels. Despite renewables growing rapidly, it will take a significant amount of time to fully replace fossil fuels; therefore, carbon capture and utilisation can help bridge this gap by reducing industrial emissions during this transition.

1.1 Carbon Capture and Utilisation (CCU)

Carbon capture and utilisation (CCU) refers to the process of capturing CO₂, both from the atmosphere and directly from industrial waste streams, primarily flue gas, and transforming it into value-added fuels, chemicals and building materials.

1.1.1 CO₂ Capture

Flue gas is a complex mixture of several components, with nitrogen making up the largest share sourced from air used for combustion. The burning of fuels adds the carbon dioxide and water vapour to the stream alongside carbon monoxide and particulate matter from any incomplete combustion throughout the process. Separating CO₂ from this complex mixture can be achieved by several methods. The most mature technology used to capture anthropogenic CO₂ utilises aqueous monoethanolamine (MEA) as a chemical scrubber.³ During MEA scrubbing, flue gas enters an adsorber in which the MEA solvent selectively absorbs the CO₂ exothermically. The dissolved CO₂ passes through a heat exchanger where the MEA is heated until the CO₂ desorbs from the solvent and is captured at the stripper outlet.

A more recent alternative approach to capturing CO₂ from waste streams is utilising high-porosity solid materials, such as zeolites⁴ or activated carbon,⁵ to attract and adsorb CO₂ molecules. The CO₂ molecules can then be released with a change in pressure or temperature. This is an economically attractive alternative to MEA scrubbing as it requires less energy to regenerate, suggesting adsorption has the potential to become the dominant technology as the field advances.

1.1.2 CO₂ Conversion

The fight against climate change has seen a drastic increase in CO₂ conversion research over recent years, with photocatalytic, electrocatalytic, and thermochemical approaches showing significant promise.

1.1.2.1 Photocatalytic

Inspired by photosynthesis, the photocatalytic conversion of CO₂ aims to utilise solar energy to activate a catalyst which will in turn convert CO₂ to value-added chemicals.⁶ The basic principles of this process involve an initial light absorption by the photocatalyst in which photons interact with electrons in the valence band providing a significant amount of energy. This energy will excite electrons from the valence band to the conduction band, each leaving behind a positively charged electron-hole. Electron-hole pairs possess redox properties, with the electron acting as a reducing agent, and the hole acting as an oxidising agent. In the case of CO₂ reduction, these electron-hole pairs can provide both reduction and oxidation pathways depending on the specific catalyst material and reaction conditions.

A plethora of photocatalysts have been explored for the conversion of CO₂, including the 'classic photocatalyst' TiO₂ and its doped-variants,⁷⁻⁹ alongside more modern materials such as metal-organic frameworks (MOFs)^{10,11} and graphitic carbon nitride (g-C₃N₄).^{12,13} A strategic advantage of utilising photocatalysis is the ability to harness solar energy mitigating the need for additional energy input from non-renewable sources; however, low conversion efficiencies and the competing parasitic hydrogen evolution reaction (HER) are key challenges which need to be addressed for the advancement of the field.

1.1.2.2 Electrochemical

The electrochemical reduction of CO₂ essentially reverses hydrocarbon combustion to yield a range of carbon-based products. Thermodynamically, the energy necessary to achieve this chemical transformation is quite moderate, corresponding to the standard reduction potentials indicated in Table 1.1. However, as multielectron and proton-coupled reactions, the reactions are more complicated than thermodynamics implies.

Reduction potentials of CO₂	E° / V (vs SHE, pH 7)
$2\text{CO}_2 + 2\text{H}^+ + 2\text{e}^- \rightarrow \text{CO} + \text{H}_2\text{O}$	-0.52
$\text{CO}_2 + 2\text{H}^+ + 2\text{e}^- \rightarrow \text{HCOOH}$	-0.61
$\text{CO}_2 + 4\text{H}^+ + 4\text{e}^- \rightarrow \text{HCHO} + \text{H}_2\text{O}$	-0.51
$\text{CO}_2 + 6\text{H}^+ + 6\text{e}^- \rightarrow \text{CH}_3\text{OH} + \text{H}_2\text{O}$	-0.38
$\text{CO}_2 + 8\text{H}^+ + 6\text{e}^- \rightarrow \text{CH}_4 + 2\text{H}_2\text{O}$	-0.24
$2\text{CO}_2 + 12\text{H}^+ + 12\text{e}^- \rightarrow \text{C}_2\text{H}_4 + 4\text{H}_2\text{O}$	-0.34
$2\text{H}^+ + 2\text{e}^- \rightarrow \text{H}_2$	-0.42

Table 1.1 Carbon Dioxide reduction standard electrochemical potentials at pH 7.0 vs SHE¹⁴

The electrochemical reduction of CO₂ is infamously plagued by two major obstacles - complex reaction dynamics and sluggish kinetics leading to a high overpotential. Slow reaction kinetics are observed due to the slow binding of CO₂ molecules to the catalyst surface, while the excess energy requirement is attributed to the formation of CO₂^{•-} radical anion intermediate during the early stages of CO₂ reduction.¹⁵

In order to achieve a successful and commercially relevant eCO₂ reduction, there are three key requirements that need to be addressed: optimising faradaic efficiency, enhancing selectivity, and ensuring system stability. Achieving a high faradaic efficiency will ensure greater utilisation of input electrons, minimising energy waste and maximising product generation. An enhanced selectivity will preferentially form desired products while significantly reducing the cost of product separation following electrolysis. Finally, achieving a stable system will enable continuous CO₂ reduction without the need for frequent system maintenance or catalyst regeneration.

The mechanism of electrochemical CO₂ reduction (eCO₂RR) is complex and has been under investigation for many years. While there have been different CO₂RR mechanisms proposed, it is well-founded that both the catalyst material and experimental conditions have a significant effect on the reaction products observed. Some of the influential factors on eCO₂RR include both intrinsic and extrinsic parameters. Intrinsic factors, inherent to the electrochemical system, include the electrode material, electrolyte composition, and applied potential. Extrinsic factors,

external to the electrochemical system, include temperature, concentration of CO₂, electrolyte pH, catalyst support, electrode morphology, and reactor design. Understanding and optimising these factors is crucial for developing stable and efficient eCO₂RR processes.

Due to their intrinsic cost-effectiveness and sustainable nature, low-concentration aqueous electrolytes are often favoured for eCO₂RR. This decision, however, presents potential drawbacks, specifically regarding the solubility of CO₂ in aqueous media, which is reported to be ~34 ppm (25 °C, 1 atm) by volume.¹⁶ Although certain parameters can increase the solubility of CO₂ in water, such as increased temperature and pressure, the additional engineering and energy requirement is often deemed unjustified. The low solubility of CO₂ in aqueous electrolytes often necessitates higher current densities to maintain a sufficient supply of CO₂ at the electrode surface. However, an increased current density will likely lead to the parasitic hydrogen evolution reaction (HER), as it is more thermodynamically favoured over the initial CO formation step of CO₂RR – thus dramatically reducing the faradaic efficiency of the process.¹⁴ Various strategies can be employed to suppress the HER, such as the use of alkaline electrolytes;¹⁷ however, the influence of an intelligently designed catalyst will ultimately be the key player in promoting the selectivity of CO₂RR. A good catalyst will inhibit the HER by either reducing the overpotential necessary to drive the CO₂RR thus making it the more kinetically favourable process; or by providing a surface that has an affinity to bind CO₂ molecules more strongly than protons or OH⁻ ions.

Alternatively, non-aqueous electrolytes offer several advantages over traditional aqueous electrolytes for the purposes of CO₂ reduction. In addition to superior ionic conductivity, non-aqueous electrolytes typically possess a higher CO₂ solubility than water. This is due to the absence of hydrogen bonding present between CO₂ and water molecules. Acetonitrile (MeCN) is a commonly used non-aqueous electrolyte for CO₂RR as it boasts a CO₂ solubility of 2700 ppm (1 atm, 25 °C), approximately 80 times greater than aqueous-based electrolytes.¹⁸ The use of non-aqueous electrolytes experimentally, and consequentially industrially, can be challenging and presents significant drawbacks. For example, in addition to its high cost and high toxicity, acetonitrile has been shown to limit the selectivity to two-electron

reduction preventing the formation of certain CO₂RR products such as ethylene and ethanol.¹⁹

To date, the most efficient and widely reported catalyst for eCO₂RR is copper. Due to its abundance, low cost, and diverse range of products, copper is the most commonly used electrocatalyst for CO₂ reduction.²⁰ Although a diverse range of products is observed from Cu-catalysed CO₂RR, this presents inherent challenges via the separation and purification of reaction products. Due to poor selectivity, Cu can produce a multitude of products in both the gas and liquid phases which require separation; a complex and costly process which impedes industrial implementation. In addition to poor selectivity for desired CO₂RR products, copper can be susceptible to degradation over time, especially under harsh conditions often used for CO₂RR. This catalyst degradation can manifest as dissolution, surface oxide formation, and carbonaceous species formation, ultimately leading to a loss of Cu active sites and thus reduced catalytic activity.²¹

Alternative metal-based electrocatalysts have been explored for CO₂ reduction including MOFs,²²⁻²⁴ single-atom catalysts (SACs),²⁵⁻²⁸ and heterogeneous bimetallic catalysts,²⁹⁻³¹ however, those reported typically suffer from low faradaic efficiencies. The development of highly tuneable catalysts is crucial for precisely directing reaction pathways and maximising both the selectivity towards desired products and overall catalytic activity. This ongoing pursuit necessitates the exploration of novel materials with readily modifiable properties to achieve optimal catalytic performance.

In the search for optimal CO₂RR catalysts, it is increasingly frequent that computational modelling techniques, such as density functional theory (DFT), are employed to identify novel classes of materials with significant potential. In recent years, 2D materials have been the focus of many computational studies due to their high surface areas, superior electronic conductivities, and excellent stability under harsh reaction conditions.³² DFT-based studies have reported the activity and selectivity of various 2D materials for eCO₂RR, including covalent-organic frameworks (COFs),^{33,34} chalcogenide-based 2D materials,³⁵ and MXenes.

Early studies of a new class of 2-Dimensional carbides and nitrides, known as MXenes, have identified them computationally and experimentally as being advantageous for CO₂RR due to their unique properties, which lend themselves to being ideal candidates as electrocatalysts.³⁶⁻³⁹ Specifically, their high electrical conductivity, tuneable surface chemistry, and large surface area are particularly advantageous when intelligently designing novel electrocatalytic materials. The intrinsic properties of a MXene will be further discussed in Chapter 1.2.8. While there are early indications of MXenes being promising for CO₂RR, experimental evidence supporting these computational findings is significantly lacking. The MXene literature to date is comprehensively discussed in Chapter 1.3, with particular focus on the limited experimental MXene-catalysed eCO₂RR publications.

In order to intelligently design efficient MXene catalysts, a thorough understanding of how synthesis methods for both MXenes and their MAX phase precursors affect the resulting catalyst is essential.

1.2 MXenes and MAX Phase - $M_{n+1}AX_n$

MAX-Phase materials have a general formula $M_{n+1}AX_n$ where M is a transition metal, A is an A-group element, and X is C and/or N, $n = 1 \dots 3$. Although originally discovered in the 1960s by Jeitschko and named 'H-phases',⁴⁰ it was not until the late 1990s that MAX phase research progressed significantly with Barsoum reporting the discovery of new MAX phase subgroups.⁴¹ To date, more than 340 MAX phases have been reported in the literature, with over half of them being experimentally synthesised.⁴²

All reported MAX phases have a hexagonal crystal structure exhibiting $P6_3/MMC$ symmetry with close-packed M layers, and X atoms filling the octahedral sites.⁴³ These M-X bonds have mixed covalent/metallic/ionic character. Between $M_{n+1}X_n$ layers are layers of A-group element atoms with the resulting M-A bonds having metallic character. The crystal structure of a M_3AX_2 MAX phase is shown in Figure 1.2, drawn using crystallographic data reported by Fu et al.⁴⁴

Due to the intrinsic strength of the interlayer bonding present in MAX phases – a mechanical breaking of these bonds is not possible and therefore an alternative exfoliation method should be employed.

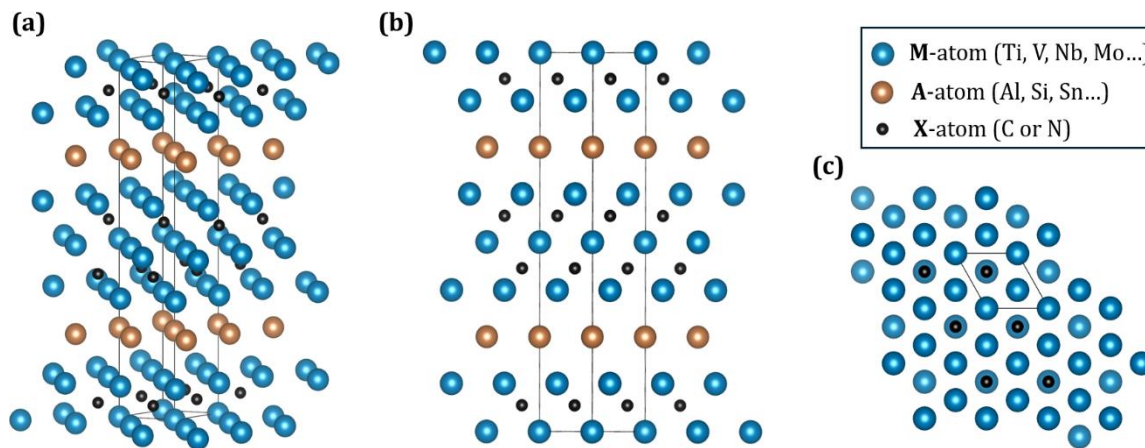


Figure 1.2 - Crystal structure of a generic M_3AX_2 MAX phase from a (a) perspective view (b) side view (c) top-down view, showing alternating layers of M_6X octahedra and A elements

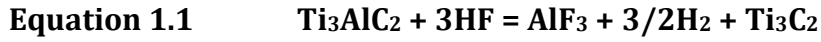
Due to their layered structure, MAX phases exhibit the properties of ceramic materials as well as metals – demonstrating a high yield strength and significant plasticity at high temperatures while also displaying good electrical conductivity and high thermal conductivity. In addition, MAX phase materials offer a high level of oxidation resistance, high melting points, and corrosion resistance.

MAX Phases are typically synthesised in bulk via the mixing and subsequent high-temperature sintering of either elemental or compound powders. The ambient pressure sintering of MAX Phase materials is an effective and scalable method of synthesis and has been reported for Ti_2AlC ,⁴⁵ $MoTi_2AlC_2$,⁴⁶ and Ti_3AlC_2 ,⁴⁷ among others. Due to the volatility of aluminium; it is crucial that the proper ratio of precursor powders is used during the synthesis.

1.2.1 Acidic Etching of Ti_3AlC_2 to Ti_3C_2 MXene

In 2011, Barsoum reported the selective etching of the A-layer of Ti_3AlC_2 via immersion in a 50% concentrated hydrofluoric acid (HF) solution to yield Ti_3C_2 – a 2D-like material comprising the remaining pristine M and X layers.⁴⁸ A year later, Barsoum demonstrated that the selective etching of the A-layer via HF could be applied to many other MAX phases.⁴⁹ These materials were so-called MXenes; with the M and X denoting the transition metal and carbon and/or nitrogen layers respectively. The “ene” suffix was used to highlight the material’s likeness to graphene, the Nobel prize-winning monolayer material discovered in 2004.^{50,51} During the acidic synthesis of MXenes; the A-layer is selectively removed by breaking

the comparatively weak metallic A-M bonds via hydrofluoric acid etching leaving the strong M-X bonds intact. When A atoms are removed during the etching process, they are replaced by a combination of -O, -OH, and -F atoms which are present in the etching solution. These terminating groups are often denoted by T_x. Using Ti₃AlC₂ as an example, the HF synthesis of Ti₃C₂ MXene proceeds via the following reaction:



To date, over 100 MXenes have been predicted via theoretical calculations, with over 40 MXenes having been experimentally realised.⁵² This thesis will focus on the most popular MXene; Ti₃C₂T_x, which is synthesised from Ti₃AlC₂.

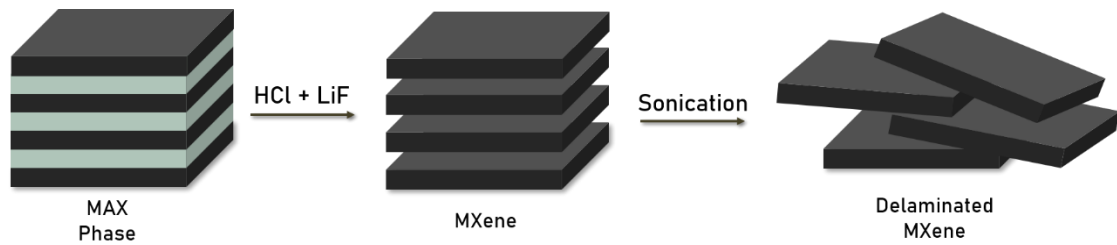
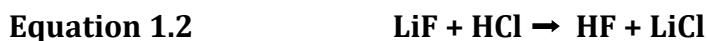


Figure 1.3 Schematic representation of MXene synthesis via in-situ HF generation

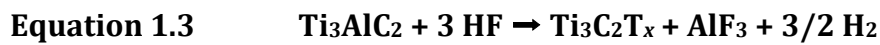
Due to the surface terminations previously described, the MXene multilayers are held together by hydrogen bonds and, similarly to graphene, Van der Waal forces.

1.2.3 MXene Synthesis – Acidic Etching

Due to the critical hazards associated with HF, alternative etching solutions are necessary to reduce the amounts of HF handled and thus reduce the overall hazard associated with the synthesis. The *in-situ* generation of HF is an attractive alternative to direct addition as this mitigates the direct handling of HF and reduces the exposure. Reactions of fluoride-containing salts with acid for HF generation have been reported previously including sodium bifluoride, potassium bifluoride, and ammonium bifluoride.^{53,54} In 2014, Ghidui reported a method of synthesising Ti₃C₂ using *in-situ* generated HF via the addition of LiF to HCl.⁵⁵ The HF generated during the reaction selectively etched the Al layer and was subsequently consumed during the process. The first of the two-step reaction is described via the following:



Once HF has been generated; it will proceed to etch the Al layer of the Ti_3AlC_2 MAX phase via the following reaction:



Aluminium fluoride is produced as a byproduct via the reaction between the etched Al atoms and dissociated F- ions from HF molecules. As aluminium fluoride is soluble in water; it is successfully removed during the subsequent washing of the MXene. Notably, due to the presence of Cl^- ions in the etching solution, sourced from HCl; the surface terminations of the resulting MXene sheets will be exclusively -Cl, -F, -OH, and -O. Ghidiu also claimed that Li^+ ions present in the etchant solution would act as intercalants and therefore delaminate the material with ease into single Ti_3C_2 flakes. This method would later be modified to yield large area flakes of $\text{Ti}_3\text{C}_2\text{T}_x$ by increasing the LiF to MAX Phase ratio – this technique is known as the minimally intensive layer delamination (MILD) method.⁵⁶

1.2.4 Hydrofluoric Acid-Free Synthesis of MXenes

In the interest of avoiding the use of HF entirely, various fluorine-free synthetic methods have been reported for the etching of Ti-based MXenes. These include the use of molten-salt etchants,⁵⁷⁻⁵⁹ electrochemical exfoliation,⁶⁰⁻⁶² and highly alkaline etchants.⁶³ In the case of alkaline etching; MXene synthesis can be particularly challenging kinetically due to the formation of some oxide/hydroxide layers on the surface of the MAX phase. In 2018, Li et al reported the fluorine-free synthesis of Ti_3C_2 via alkaline treatment, in which Ti_3AlC_2 was etched using 27.5M sodium hydroxide (NaOH) at 270°C.⁶³ Inspired by the Bayer process, Li attempted to utilise higher temperatures and higher NaOH concentrations to help dissolve the Al oxides and hydroxides formed on the MAX phase surface. The effects of both temperature and NaOH concentration on the resulting MXene were reported. It was found that a temperature of 270°C was necessary for a successful etching, while concentrations of 20 M and 27.5 M at this temperature gave Ti_3C_2 of 81% and 92% purity respectively. Although the soaking time of the synthesis was reported as 12 hours, there appears to be no justification for this seemingly crucial parameter. Notably, due to the lack of fluorine and chlorine atoms in the etching solution, there will be no -F

or -Cl surface terminations on the resulting MXene; instead, the MXene surface will be populated exclusively with -O and -OH terminations.

When a MXene with specific surface terminations is required, chlorine- and fluorine-free etching methods can avoid the need for post-etch surface treatments. For example, $\text{Ti}_3\text{C}_2\text{Cl}_2$ MXene was synthesised by Sarfraz et al. for the purposes of electrochemical water splitting.⁶⁴ The electrochemical performance of both $\text{Ti}_3\text{C}_2\text{T}_x$ and $\text{Ti}_3\text{C}_2\text{Cl}_2$ was evaluated for the hydrogen evolution reaction (HER). $\text{Ti}_3\text{C}_2\text{Cl}_2$ exhibited excellent HER behaviour; requiring a 259 mV [vs RHE] overpotential to deliver 10 mA cm^{-2} current density; calculated to be 185 mV less of an overpotential than the T_x terminated MXene. Finally, the $\text{Ti}_3\text{C}_2\text{Cl}_2$ MXene was reported to be inherently more electrochemically stable than the HF-synthesised MXene.

1.2.5 Effects of Synthetic Methods on the Structure of MXenes

Although the chemical etchant used in the synthesis of MXenes will selectively etch the A-layer from the MAX structure, the conditions used for the synthesis can greatly affect the structure and chemistry of the MXene produced. For example, the chemical composition and concentration of etchant solutions,^{63,65,66} etching time,^{67,68} and MAX phase particle size has been reported to greatly influence the morphology and properties of the resulting MXene.⁶⁹

1.2.6 Surface Chemistry

According to several reports, the functional groups terminating the surface of MXene sheets play an important role in both the physical and chemical behaviour of the material.^{70,71} As previously stated, the surface termination groups of any synthesised MXene material will be influenced by the etchant solution used and the species present within it. A typically synthesised Ti_3C_2 MXene via HF etching will be terminated with a mixture of -O, -OH, and -F in similar ratios; however, these ratios can be adjusted by altering the concentration of HF – with a higher concentration increasing -F terminations and vice-versa.

Early DFT studies have reported the surface termination groups of MXenes to be of significant importance in the role of these materials as catalysts.⁷²⁻⁷⁴ A particular focus on hydroxyl terminations (-OH) has been seen in the literature due to their

Lewis acidity, promoting the adsorption and activation of molecules – a requirement for efficient and selective catalysis.^{72,75}

Wei et al. have reported the -OH functionalisation of MXenes by immersing HF-synthesised Ti_3C_2 in various strong bases.⁷⁶ $Ti_3C_2T_x$ was immersed in 1M solutions of LiOH, NaOH, and KOH to replace terminating -F groups with -OH groups. EDS analysis of the base-treated MXenes showed an overall increase of oxygen by approximately 10% across multiple sites on the MXene sheets; and an overall reduction of fluorine by approximately 20% when compared to $Ti_3C_2T_x$. The most effective base treatment was NaOH, giving an increase in oxygen content of 11.74% and a decrease in fluorine content of 19.74%. Although the EDS analysis strongly suggests a successful -OH functionalisation; the utilisation of x-ray photoelectron spectroscopy (XPS) would provide a more comprehensive insight into the Ti-bonding and therefore surface groups present.

There have been several reports of alternative species being used to functionalise the surface of MXenes for various applications.⁷⁷⁻⁷⁹ One particularly comprehensive study was published by Kamysbayev in 2020 which detailed the successful termination of Ti_3C_2 and Nb_2C with Br, S, Se, Te, and NH_2 .⁸⁰ This was achieved by the addition of Lewis acidic $CdBr_2$ via the molten salt synthetic method. From here, $Ti_3C_2Br_2$ was dispersed in a second molten solvent and added to Li_2Se , Li_2S , Li_2Te , or $NaNH_2$ to give -Se, -S, -Te, or NH_2 terminations respectively. This paper was the first time a $Ti_3C_2Br_2$ MXene was reported in the literature and holds huge significance due to the ease at which non-traditional terminations can be added to MXene surfaces.

1.2.7 Storage Conditions

Oxidative degradation of a MXene is a common phenomenon which can have drastic effects on the inherent characteristics and subsequent uses of the MXene. Although the oxidation stability of a MXene can be increased via adaptations to the synthetic method, the simplest way to avoid the degradation of a MXene is via the proper storage and handling of the material. Due to the harsh chemical etching of a MXene, atomic defects can often be found at both the edge planes and basal planes of the MXene sheets. The reaction of oxygen and/or water with these exposed M or X sites

can lead to the formation of transition metal oxides and amorphous carbon, which will drastically alter the inherent properties of the MXene.

In 2016, Sang et al reported the characterisation and resulting influence of Ti vacancies in an HF prepared $\text{Ti}_3\text{C}_2\text{T}_x$ MXene.⁸¹ HF in the etchant solution was attributed to the removal of termination groups from the MXene surface, exposing the underlying bare Ti atoms. Oxygen then reacts with the Ti vacancies (V_{Ti}) and Ti vacancy clusters ($\text{V}_{\text{Ti}}^{\text{C}}$) present following the HF synthesis to form TiO_2 . It was reported that an increase in HF etchant concentration directly increased the observed Ti vacancies.

In theory, the opportunity to avoid the presence of both water and oxygen via storing them as a dry powder is a very attractive solution; however, in practice, there are distinct disadvantages attributed to the filtering and drying of a MXene.

Owing to the strong van der Waals forces present between MXenes sheets, a restacking phenomenon occurs when MXenes are filtered and dried. Not only can restacking drastically reduce the active surface area thus limiting the accessibility of surface terminating groups, but it has also been proven to drastically alter a material's electronic conductivity due to a change in the interlayer spacing. Several attempts have been made to overcome this electrostatic attraction present in $\text{Ti}_3\text{C}_2\text{T}_x$ predominantly via the widening of the interlayer channels between restacked sheets. The pillaring of MXene materials, intercalation of ions, and external stimuli have all been reported to increase the interlayer spacing between MXene sheets and reduce the adverse effects of restacking.

Although the delamination of MXene sheets can be attempted following restacking, the repeated wetting and drying of MXenes can have detrimental effects on the material itself and may lead to severe structural changes and potentially complete degradation. Additionally, the loss of functional groups, increased contamination risk, and reduced dispersion can all be attributed to a repeated wetting and drying of MXenes.

The ability to store a MXene stably without the need for extensive processing is of great significance. Shuck et al. have provided comprehensive instructions for the storage of MXenes which highlight key strategies for prolonging the shelf-life of a

MXene:

1. Temperature – The storage of MXenes at low-temperature will inhibit the oxidation mechanism and prolong the MXenes lifetime; cryogenic freezing can be used to preserve the MXene indefinitely.
2. Concentration – If stored as a solution, an increase in MXene concentration will correlate to an increased shelf-life.
3. Atmosphere – The removal of oxygen from any MXene sample is crucial, and therefore saturating an aqueous MXene dispersion or replacing the atmosphere of a powder sample with Ar or N₂ is highly recommended.
4. Light – UV light has the potential to damage and degrade MXenes; therefore they must be stored in a dark environment and exposed to light as infrequently as possible.
5. Flake quality – Defect sites on the surface of a MXene flake will promote rapid oxidation, so less-harsh etching conditions are recommended for a long-lasting MXene.
6. Washing – Any remaining impurities from the synthesis or chemical treatment of a MXene will promote degradation, especially those of acidic or basic nature.⁸²

1.2.8 Properties of MXenes

As discussed earlier, MXenes have gained significant research interest since their discovery, due to their unique combination of properties.

1.2.8.1 Electronic Properties

MXenes have been explored for their electronic properties in applications such as supercapacitors, electromagnetic interference shielding materials, sensors, electrocatalysts, field effect transistors, photocatalysts, and electrochemical energy storage. The electronic conductivity of MXenes is regarded as one of their most desirable properties and a primary motivation for the advancement of MXene-based materials.³⁷

In 2021, Zeerati et al reported the electronic behaviour of Ti₃C₂T_x synthesised via a modified MILD synthetic method.⁸³ The Evaporated-Nitrogen Minimally Intensive Delamination Method (EN-MILD) synthetic approach involved the purging of the reaction vessel with dry nitrogen throughout the synthesis; this led to the partial

evaporation of the LiF-HCl etching solution thus increasing the salt and acid concentration over the course of the reaction. The resulting $\text{Ti}_3\text{C}_2\text{T}_x$ was reported to exhibit electrical conductivity of up to $2.4 \times 10^4 \text{ S cm}^{-1}$; which is still the highest reported conductivity for a Ti-based MXene to date. Zeerati attributed this increased conductivity to the high purity of the MXene as well as a larger flake size. Several papers published since detailing the electronic properties of Ti-based MXenes have supported the claims that flake size and quality have a significant effect on conductivity.^{84,85}

1.2.8.2 Mechanical Properties

MXenes exhibit impressive mechanical characteristics, particularly when compared to traditional ceramics - boasting high tensile strength, high degree of flexibility, low plastic deformation, and practically relevant thermal stability. These unique physical characteristics have led to their inclusion in a wide range of applications such as flexible electronics, structural composites, protective coatings, and aerospace implementation. A recent review of the mechanical properties of MXenes published by Wyatt et al. demonstrates how the mechanical properties of a MXene can be enhanced/modified for a particular application via changes via synthetic adaptations.⁸⁶

1.2.9 Characterisation of MXenes

MXene characterisation is crucial due to their inherent versatility and sensitivity to external factors. A comprehensive suite of analytical techniques is required to unveil the full spectrum of their unique properties. Comprehensive characterisation not only grants insight into the quality of a MXene sample, verifying purity and level of delamination but also evaluates individual properties through various techniques.

Powder X-ray diffraction (XRD) is the most common analytical technique used to characterise a MXene, with a focus on its crystal structure. In addition to crystallographic insight, XRD can be used to determine the degree of interlayer spacing, sample purity, and flake orientation.⁸⁷

X-ray photoelectron spectroscopy (XPS) is a complex surface-sensitive analytical technique which provides insight into the specific surface chemistry of a MXene and

the bonding present between surface functional groups. XPS is particularly valuable when evaluating any surface treatments of a MXene, as changes in the surface chemistry can be monitored and quantified post-treatment.⁸⁷

Although Raman spectroscopy is a powerful analytical tool capable of probing both the surface chemistry of a MXene and its structural properties, it is not as readily reported as other characterisation techniques mentioned herein. Different MXene layers can exhibit characteristic Raman shifts, allowing the identification of single-flake and multilayer MXenes. Additionally, Raman is sensitive to functional groups on the MXene surface and can be used to identify groups such as hydroxyl (-OH) and oxygen (-O).⁸⁷

Scanning electron microscopy (SEM) is a powerful visual characterisation method for the reporting of MXenes as their unique accordion-like structure can be observed with surface features clearly resolved. A vast amount of information can be obtained using SEM, including lateral flake size, degree of delamination and stacking, interlayer spacing, and degree of oxidation.⁸⁷

Brauner-Emmett-Teller (BET) surface area analysis is commonly used to determine the specific surface area of MXenes. This technique is particularly useful when evaluating the degree of delamination in a MXene sample, as a higher degree of delamination will drastically increase the surface area of the material.⁸⁷

Thermogravimetric Analysis/Differential Scanning Calorimetry are two important techniques for characterising the thermal stability and phase transitions of MXenes. In addition, TGA/DSC can also provide information regarding the nature of terminating groups on the MXene surface, as functional groups such as -F, -Cl, and -OH will all desorb at different temperatures.⁸⁷

Only by employing a multi-faceted approach, with a comprehensive suite of analytical techniques, can a holistic understanding of the MXene material be obtained.

1.2.10 Intercalation and Delamination

Owing to the weak Van der Waals forces between MXene sheets, delamination of ML-MXenes can yield single flakes or few-layered MXenes, depending on the desired

application. Delaminating MXenes can alter their electronic properties and drastically increase the catalytic surface area, providing more active sites for reactions and potentially enhancing catalytic performance. In recent work, Thakur et al. evaluated the effects of temperature and reaction environment during delamination on MXenes following acidic etching. Interestingly, under certain conditions, few-layered MXenes were achieved drastically varying in size – with flakes over 3 times larger comparatively. Small MXene flakes are considered undesirable as they are more prone to edge-driven oxidation, thus degrading the MXene at a much faster rate. Additionally, under certain conditions, a significant number of defects were observed on the smaller MXene flakes, which will also promote the oxidation of bare Ti atoms on the surface.

MXene delamination plays a significant role in the behaviour of the resulting material and must be done in a controlled manner to ensure optimal catalytic performance and negate undesirable consequences. Methods of delamination and the intercalation of chemical species will be discussed in Chapter 4.1.1.

1.3 MXenes in Electrochemistry

To date, over 18,000 scientific articles have been published on MXenes, reflecting their rapid growth in popularity. In recent years, MXenes have gained significant attention in the field of electrochemistry, with over 1000 publications exploring their properties and applications through either computational or experimental means. Nearly one-third of these studies focus on their applications within the discipline of energy fuels. Figure 1.4 presents graphical data obtained from derived from Clarivate™ (Web of Science™)⁸⁸ summarising publications with MXene-related keywords by publication count and journal categories.

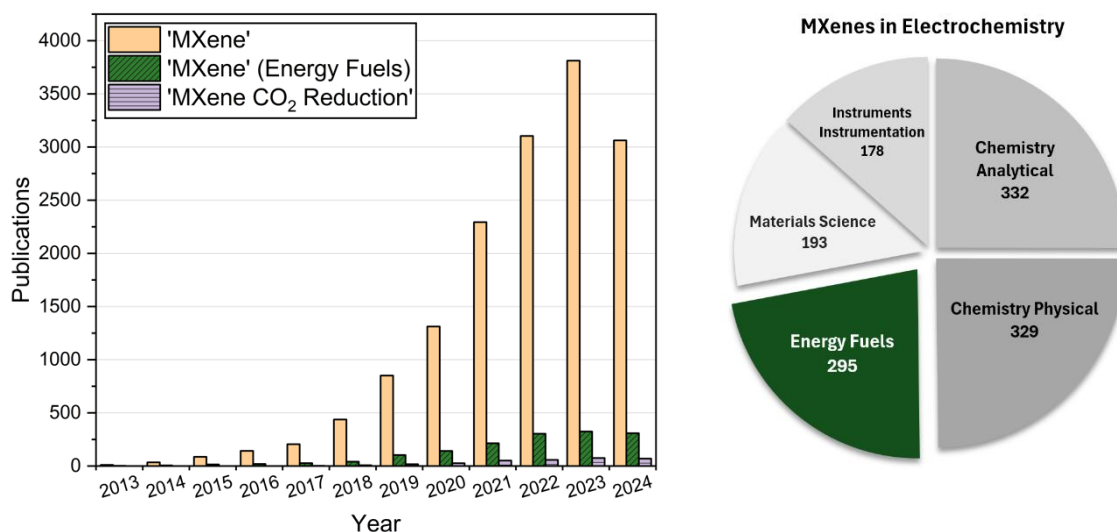


Figure 1.4 Graphical data a) Publications by keyword, i) 'MXene' ii) 'MXene' [Cat: Energy Fuels] iii) 'MXene CO₂ Reduction' b) MXene papers to date by Web of Science categories

Due to their superior electronic properties, MXenes have been widely reported in both computational and experimental research within the field of electrochemistry. Their exceptional electrical conductivity allows for an efficient transport of electrons, while their increased surface area provides an ideal platform for facilitating reactions at the electrode-electrolyte interface. The highly tuneable surface of a MXene allows the strategic introduction of tailored functional groups to enhance the MXene/target molecule interaction. This level of control affords intelligent catalyst design via computational modelling, which can then be realised and further optimised experimentally.

Recent advances in solid-state battery research have seen a significant increase in MXene-incorporated lithium-ion battery (LIB) papers, with MXenes reportedly suppressing dendrite formation, enhancing ionic conductivity of electrolytes, and improving the energy density and cycle life of solid-state LIBs.⁸⁹⁻⁹¹ For these solid applications, MXene electrodes were reportedly synthesised via hydrothermal, sol-gel, and vacuum filtration methods.

1.3.1 MXenes in Reduction Reactions

MXenes have emerged as promising materials for a variety of reduction reactions, such as the nitrogen reduction reaction (N₂RR), to synthesise ammonia, the

hydrogen evolution reaction (HER), and the aforementioned carbon dioxide reduction reaction (CO₂RR).

The synthesis of ammonia is a crucial industrial process, which has been dominated by the Haber-Bosch process since the early 20th century. In recent years, the electrocatalytic N₂RR has been reported as a promising new method to synthesise ammonia efficiently and sustainably, harnessing renewable energy sources to do so. Within the last 5 years, Ti₃C₂ MXene has been reported to efficiently convert N₂ to NH₃ achieving both a high activity and selectivity.⁹² Previously, comprehensive DFT calculations suggested that a moderate proportion of fluorine terminations were beneficial in the eN₂RR due to their affinity to adsorb and activate N₂ molecules in the surface of the MXene.⁹³ These predictions were later confirmed experimentally by the work of Ding et al. in which they modified the surface of Ti₃C₂ with fluorine terminations to find the optimal F-termination density for N₂RR activity.⁹⁴ A medium F-termination population was reported to give the highest NH₃ yield, with the authors suggesting that with further surface functionalisation development, N₂ fixation may be improved.

In the pursuit of efficient hydrogen evolution reaction (HER) catalysts, titanium-based MXenes have gathered attention over recent years as promising alternatives to traditional platinum-based materials. Li et al have reported the theoretical evaluation of Ti₂C for HER in acidic media, with an -F termination-rich surface calculated to require the lowest overpotential.⁹⁵ Contrastingly, Handoko et al. have reported the undesirable effect of -F functionalisation for HER on Ti₃C₂.⁹⁶ Experimental data, supported by DFT calculations, suggested that a fully O-terminated basal plane gave the ideal HER overpotential – a finding which was not exclusive to Ti-based MXenes, with further investigation revealing Mo-based MXenes also exhibit ideal HER performance when fully O-terminated. These findings were later confirmed by Jiang et al, who reported significantly higher HER activity for O-terminated Ti₃C₂ than that of the mixed termination MXene, Ti₃C₂T_x.⁹⁷

1.3.1.1 MXenes for CO₂RR

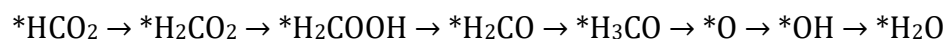
To date, investigations into MXenes as efficient CO₂RR catalysts have been overwhelmingly theoretically based, with studies emerging since only 2017.

In 2019, Chen et al, utilised first-principle simulations to screen various hydroxyl-terminated MXenes for the electrocatalytic conversion of CO₂ to CH₄.⁹⁸ Mechanistic insight suggested the H atom in -OH terminations to be active, stabilising CO₂RR reaction intermediates and lowering the overpotential. Notably, Ti₃C₂ was excluded from this study, despite being the most widely reported and commercially available MXene.

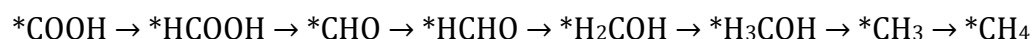
A very recent study by Meng et al. utilised DFT calculations to assess the stability and impact of different surface groups terminating Ti₃C₂ on resulting CO₂RR performance.⁹⁹ It was calculated that a larger -O termination content requires a smaller activation potential, attributed to the role of both -O and -OH terminations acting as H-acceptors and donors, respectively. When compared to the traditional Cu electrocatalysts, the authors suggested a reduced activation potential of up to 0.6 V could be observed for -O and -OH terminated Ti₃C₂.

In early 2020, Xiao and Zhang published a computational study evaluating Ti₃C₂OH MXene for the purposes of CO₂RR, assessing its activity and selectivity alongside a range of other M₃C₂ MXenes.¹⁰⁰ The study published gave significant insight into the mechanisms present, while also providing reasoning as to why different transition metals may affect the product selectivity of hydroxyl-terminated MXene catalysts. Firstly, it was proposed by the pair that two possible conversion pathways are present; with the nature of the transition metal determining down which pathway the reaction will proceed. The first pathway is shown in pathway 1 and is predicted to be the primary pathway for all but two MXenes studied; Ta₃C₂ and W₃C₂, which are predicted to follow the second pathway, detailed in pathway 2.

Pathway 1)



Pathway 2)



Following pathway 1, *HCO₂ is formed during the first protonation step, which then proceeds to *H₂CO₂ as a result of being stabilized by the H-atom sourced from the -OH terminating groups. Following several further reaction steps, CH₄ is desorbed

from the surface of the catalyst when the intermediate *H_3CO is protonated. This lone adsorbed *O is finally protonated twice to complete the pathway and yield H_2O . When observing pathway 2, this reaction appears to yield CH_4 also; however, this was deemed not the case experimentally. Following the second protonation step yielding *HCOOH , it was indicated that formic acid ($HCOOH$) may easily desorb as a liquid from the surface of the catalyst under standard conditions, thus preventing the continuation of the pathway and eventual production of CH_4 . Crucially, the determination of which pathway a reaction will proceed depends exclusively on the carbophilicity or oxophilicity of the transition metal. With a more oxophilic transition metal MXene, M-T_x-O-C binding will be favoured, and the reaction will therefore proceed via pathway 1; equally, with a more carbophilic transition metal MXene, M-T_x-C-O binding will be present and pathway 2 will be favoured. Due to titanium's highly oxophilic nature, Ti_3C_2OH MXene has been predicted to proceed via pathway 1 and possess the ability to greatly reduce CO_2 to CH_4 .

In one noteworthy theoretical study, Li et al. utilised DFT calculations to elucidate the mechanism of CO_2 reduction on various M_3C_2 -type MXenes.¹⁰¹ All evaluated MXenes, including Ti_3C_2 , were confirmed to be capable of catalysing CO_2 conversion to hydrocarbons in the presence of moisture, being selective towards the formation of methane. Additionally, the influence of terminating groups on CO_2 to CH_4 conversion was also reported, with -O and -OH surface terminations drastically reducing the energy cost by up to 0.75 eV during certain steps of the reaction. These findings necessitate the experimental testing and evaluation of Ti_3C_2 with -O and -OH terminations for the purposes of electrochemical CO_2 reduction in aqueous media.

Despite overwhelming computational evidence for the effectiveness of Ti_3C_2 MXene and the importance of -OH terminations in eCO_2RR , very few experimental studies have been able to support these individual claims, with none reporting the CO_2RR activity of -OH terminated Ti_3C_2 .

One of a select few papers reporting experimental data using MXenes as eCO_2RR electrocatalysts was published by Handoko et al. in 2020, investigating both Ti_2CT_x and Mo_2CT_x in non-aqueous electrolytes.¹⁰² Ti_2CT_x was prepared via both HF etching and fluoride salt etching to achieve higher and lower -F termination populations

respectively. The authors reported that fluoride-salt etched Ti₂C produced formic acid as the main product with the highest faradaic efficiency observed exceeding 56% at -1.8 V vs SHE. CO, CH₄, and other carbon products were detected in small amounts but not quantified. It was also found that CO₂RR activity was strongly correlated to the amounts of -F and -O surface termination groups, with greater amounts of -O terminations (less -F) displaying greater CO₂RR activity and selectivity. This finding correlates well with existing theoretical literature, however, Handoko et al. interestingly did not consider the role of -OH terminations on the resulting electrochemistry which would certainly be present on the surface of the MXene, nor the -Cl terminations that would be present on the fluoride salt-etched MXene surface. Finally, the use of a non-aqueous electrolyte limits the potential scale-up of the process due to its inherent safety hazards and increased cost.

1.3.1.2 The 'Copper' Standard

As previously discussed, copper-based electrocatalysts are the gold standard for electrochemical CO₂RR in the current literature, primarily due to their C₂+ product formation.¹⁰³ While several alternative CO₂RR catalysts have been reported over recent years, the optimisation of Cu-based materials accounts for the majority of literature, with a particular focus on enhancing their selectivity towards desired products.¹⁰⁴

Copper-based catalysts are reported to naturally facilitate key intermediate binding steps in the CO₂RR pathway that lead to C₂+ products, owing to their favourable surface chemistry and optimal binding energies.¹⁰⁵ While pristine MXene surfaces are considered not to possess an ideal surface chemistry for achieving C₂+ products, the high-tunability of a MXenes surface chemistry provides opportunity to modulate the adsorption energies of critical intermediates.⁷² While only a select few of these surface modifications have been experimentally realised in recent years, the literature is still in its infancy, with a wealth of opportunities to optimise the surface chemistry of a MXene to match and surpass the activity and selectivity of Cu-based catalysts.

An additional consideration when using copper-based electrocatalysts, is often the necessity to pretreat the catalyst, converting copper from its oxide into metallic

state, capable of catalysis.¹⁰⁶ In the case of MXenes, no such pretreatment is necessary as they can be used as prepared.

Finally, MXenes have demonstrated excellent stability in standard electrochemical conditions due to their structural stability and corrosion resistance over extended periods of time.³⁸ Conversely, copper catalysts have been well documented to often degrade in performance over time due to corrosion, and thus a loss of active sites.¹⁰⁷

While there is limited experimental data for MXene-catalysed CO₂RR to date for a comprehensive comparison with leading Cu-based catalysts, the compelling advantages of MXenes and promising initial results strongly justify their extensive evaluation as next-generation CO₂RR catalysts.

1.4 Commercial MXenes

In the overwhelming majority of cases, the fabrication of MXene-based electrodes is achieved using in-house synthesised MXene directly following etching. In order to mitigate the inherent safety risks of hydrofluoric acid etching, commercial samples can be obtained in powder form. It is therefore essential to understand the behaviour, handling, and processing of commercial MXene powders to realise their full potential as electrocatalysts.

At the beginning of this piece of work, in 2019, the commercial availability of MXenes was significantly lacking, with only a handful of vendors offering a limited selection of MXenes, such as accordion-like Ti₃C₂T_x costing over £400 per gram. This intrinsic cost was attributed to the hazardous nature of the MXene synthesis, likely necessitating the addition of HF solution to obtain suitably pure samples. At this time, the demand for MXenes was comparatively low, with the materials synthesised to order. Over the last 5 years, the rise in MXene popularity has seen a drastic reduction in the price of commercially available samples, likely due to the development of MXene mass production methods alongside the introduction of new suppliers. As of August 2024, the cost of accordion-like Ti₃C₂T_x was ~ £14 per gram, a staggering 30 times reduction in price than 5 years previous.

Commercial MXene materials are often cheapest and more readily available as dry powders due to the ease of transportation, minimal handling requirements and low

oxidation potential. MXene powders offer unparalleled versatility, enabling researchers to tailor to their specific applications. These powders can be effortlessly dispersed in various solvents, delaminated into few-layer (FL)/single flakes, or employed directly in their powder form.

When this body of work commenced, there was a strong emphasis on minimizing costs and using small amounts of catalyst to ensure the catalytic process remained economically viable. The inherently high cost of high-quality MXene samples often posed a significant hurdle when considering potential research directions. However, the recent drastic reduction in MXene prices is likely to open up numerous research avenues that were previously inaccessible due to cost constraints.

1.5 Thesis Scope

This thesis aims to elucidate the electrocatalytic potential of the new class of materials, MXenes, with a specific focus on $\text{Ti}_3\text{C}_2\text{T}_x$. This work will encompass both synthesised and commercially available $\text{Ti}_3\text{C}_2\text{T}_x$ to understand the synthetic challenges and cost implications associated with MXene procurement and how these have changed since the beginning of this study [Q3 2019]. Chapter 3 will detail the synthesis, characterisation, delamination, and functionalisation of both in-house synthesised and commercially sourced $\text{Ti}_3\text{C}_2\text{T}_x$. Chapter 4 will evaluate and compare various methods for fabricating and preparing novel MXene-based electrodes from dried powders. Chapter 5 will detail the development of bespoke electrochemical systems optimised for MXene-based electrode integration and will provide early evaluation of these in the context of CO_2RR .

2 Materials, and Theory

This chapter details the materials characterisation techniques used throughout this thesis and outlines the underpinning electrochemical methods and theory employed in the electrochemical characterisation of MXene-modified electrodes. Additionally, product analysis techniques are described herein which are utilised to identify and quantify the gas and liquid phase products of electrochemical CO₂ reduction.

2.1 Material Characterisation Techniques

2.1.1 Powder X-ray diffraction (XRD)

Powder X-ray diffraction (XRD) is a popular characterisation technique which can provide information on the crystalline structure of powdered materials, such as catalysts. Typically, X-rays are directed at a powder sample which are diffracted by the atoms within the materials crystal lattice.¹⁰⁸ The angles and intensities of diffracted beams are measured, resulting in a diffraction pattern which can provide vital information regarding a material's crystal structure and phase composition. XRD is the most commonly used analytical technique for characterising a MXene, with a focus on crystal structure elucidation. In addition to crystallographic insight, XRD can be used to determine the degree of interlayer spacing, sample purity, and flake orientation.

In this work, XRD patterns were obtained using a Rigaku SmartLab X-ray diffractometer with a 9 kW rotating anode Cu-source equipped with a high-

resolution Vertical θ/θ 4-Circle Goniometer and D/tex-ULTRA 250 High-Speed Position-Sensitive Detector System in reflectance mode. The system was configured with parallel-beam optics and a Ge(220) 2 bounce monochromator on the incident side. Powdered solid samples were prepared on glass slides. The measurements were performed as $\theta/2\theta$ scans with a step size of 0.01 degrees.

2.1.2 X-ray photoelectron spectroscopy (XPS)

X-ray photoelectron spectroscopy (XPS) is a complex surface-sensitive analytical technique which provides insight into the specific surface chemistry of a material. This method involves the irradiation of a sample with X-rays, causing the emission of photoelectrons from the surface.¹⁰⁹ The kinetic energy of the emitted photoelectrons is then measured to determine the binding energy of the electrons within the atoms of the material. This information can be used to understand the specific chemical environments present on the surface of a material. In the case of MXenes, XPS is useful when probing the bonding present among surface functional groups. It is also particularly valuable when evaluating the effects of any surface treatments of a MXene, as changes in the surface chemistry can be monitored and quantified post-treatment.

All XPS measurements were performed using a Kratos AXIS Supra spectrometer with a monochromatic Al $K\alpha$ x-ray source, operating at 15 kV, 15 mA and equipped with an electron gun for charge neutralisation. The spectra were referenced to the C 1s peak centred at 285.0 eV. Data was smoothed during analysis to allow for accurate peak fitting.

2.1.3 Raman Spectroscopy

Similarly to XPS, Raman spectroscopy is another surface-sensitive technique used to provide information regarding the nature of surface species and bonding present on the surface of a material. Raman spectroscopy utilises the interactions between light and matter, specifically the scattering of light by different molecular species. When light is scattered by a molecule, most photons will be elastically scattered, also known as 'Rayleigh scattering'. A small percentage of photons, however, will be inelastically scattered, where the molecule will gain or lose energy, thus transitioning to a different vibrational state. This change in energy can be monitored

via the frequency shift between the incident and scattered light to produce the Raman spectrum.¹¹⁰ As every molecule will have a unique set of vibrational modes, this can be used to identify specific species on the surface of a material and occasionally information about the bulk composition. Although Raman spectroscopy is a powerful analytical tool capable of probing both the surface functional groups of a MXene and its structural properties, it is not as readily reported as other characterisation techniques mentioned herein. Different MXene layers can exhibit characteristic Raman shifts, allowing the identification of single-flake and multilayer MXenes. Additionally, Raman is sensitive to functional groups on the MXene surface and can be used to identify groups such as hydroxyl (-OH) and oxygen (=O).

Raman Spectroscopy was performed using the SAFER (Scanning electron microscope Analysis with Fib, Ebsd/Eds and Raman) system using a 2 mW laser with an excitation wavelength of 532 nm.

2.1.4 Scanning Electron Microscopy

Scanning electron microscopy (SEM) is a powerful imaging technique that utilises focused beams of electrons to scan the surface of a material to provide high-resolution images of the structure and topography of the sample.¹¹¹ As SEM utilises electron beams as opposed to visible light, it affords a much higher resolution and magnification of the sample than traditional optical microscopy, operating typically in the nanometre range. SEM is particularly useful for the characterisation of MXenes as their unique accordion-like structure can be observed with surface features clearly resolved. A vast amount of information can be obtained using SEM, including lateral flake size, degree of delamination and stacking, interlayer spacing, and degree of oxidation.

Scanning Electron Microscopy was performed using a JEOL JSM-7800F field emission SEM under high vacuum conditions with accelerating voltages between 5 kV and 10 kV, with a working distance of 10 mm.

2.1.5 Surface Area Analysis – Gas Sorption

Brauner-Emmett-Teller (BET) surface area analysis is commonly used to determine the specific surface area of a material, typically used for catalysts and other porous

materials. BET relies on the adsorption of an inert gas, such as nitrogen, by a sample at increasing pressure. The amount of gas adsorbed by the material can be directly attributed to the specific surface area of the material.¹¹² This technique is particularly useful when evaluating the degree of delamination in a MXene sample, as a higher degree of delamination will drastically increase the surface area of the material.

Micromeritics Gas sorption isotherms were measured on a Micromeritics ASAP 2020Plus gas sorption analyser 2020 (Micromeritics Instrument Corporation, Georgia, USA) using high-purity nitrogen gas at 77 K. BET surface areas were calculated over a relative pressure range of 0.05-0.15 P/P₀.

2.1.6 Thermogravimetric Analysis/Differential Scanning Calorimetry

TGA/DSC is a combined analytical technique that is used to probe the thermal properties of a material. TGA is a gravimetric technique in which the mass of a sample is monitored over time as the sample is heated or cooled. Specific mass losses or gains can then be attributed to processes such as decomposition/dehydration or oxidation respectively.¹¹³ DSC actively monitors the heat flow in or out of a sample as it is heated or cooled to detect events such as melting, glass transitions, and oxidation.¹¹⁴ Combining these techniques provides a comprehensive overview of a sample's thermal properties. TGA/DSC is an important coupled technique for characterising the thermal stability and phase transitions of MXenes. In addition, it can also provide information regarding the nature of terminating groups on the MXene surface, as functional groups such as -F, -Cl, and -OH will all desorb at different temperatures.

In this work, TGA/DSC measurements were conducted using a Netsch - STA 449 F3 Jupiter (Netzsch, Selb, German)

2.2 Electrochemical Characterisation Techniques

Electrochemical processes can be either galvanostatic or potentiostatic. In a galvanostatic process, such as battery discharge, the current is controlled and the potential is measured. In a potentiostatic process, such as the majority of techniques

detailed herein, the potential is controlled by a potentiostat and the current is then monitored. A potentiostat maintains a constant potential difference between the working electrode and a reference electrode, mitigating changes in the reference potential. To accommodate the counter current, a third electrode is used known as a counter electrode. Evidently, a system that requires the control of a potential via a potentiostat requires a three-electrode set-up as a minimum; the working electrode, counter electrode, and reference electrode.

This thesis involves electrochemically characterising and evaluating the performance of the MXene electrodes produced, using potentiostatic methods.

2.2.1 Linear and Cyclic Voltammetry

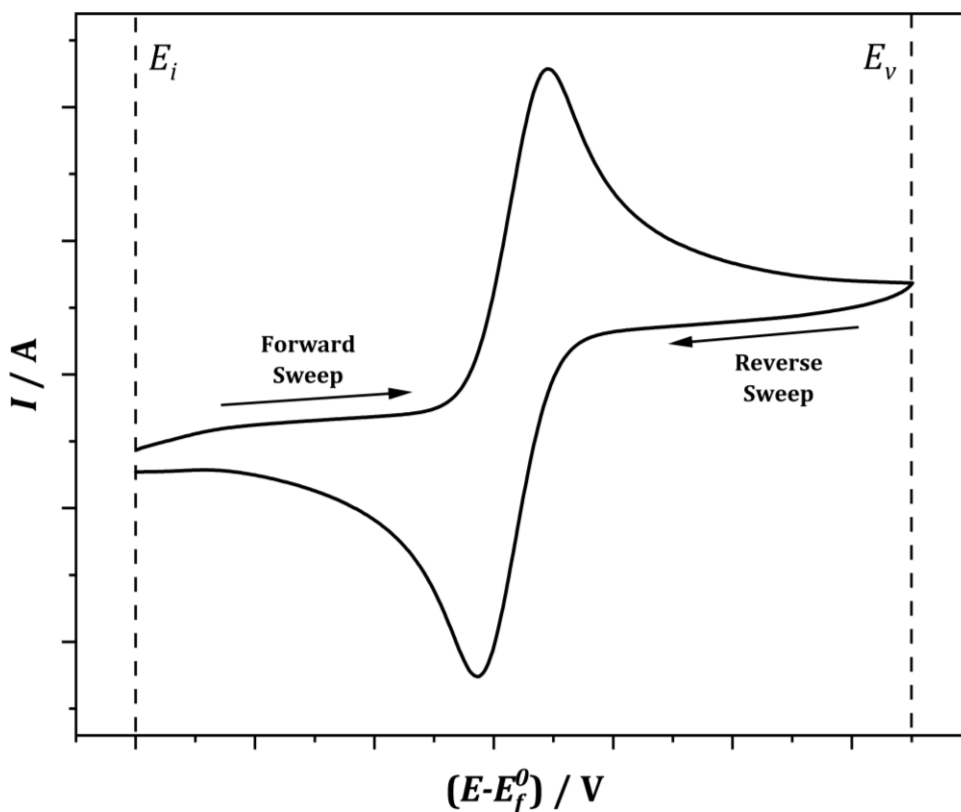


Figure 2.1 - Cyclic voltammogram of a quasi-reversible redox couple

Voltammetry is a dynamic electrochemical technique, whereby potential is controlled and modulated at a specific scan rate and the current response is measured. Cyclic voltammetry (CV) is a rapid electrochemical technique used to study the electrochemical behaviour of a system. In a typical cyclic voltammetry experiment, a starting potential (E_i) is applied to the working electrode and the

potential is swept linearly to a more negative potential (E_v), thus defining the potential window ($E_i - E_v$). During the forward sweep, species A, which is stable at E_i , undergoes electron transfer with the electrode, generating species B as a result. The potential is then swept back to E_i , causing species A' to reform via electron transfer in the opposite direction.¹¹⁵ Throughout the experiment, the current, I, is recorded as a function of potential, and a cyclic voltammogram is output. Example cyclic voltammetry data for a quasi-reversible redox couple is presented in Figure 2.1. The resulting CV shape can provide important information regarding the electrochemical processes occurring at the electrode surface. The parameters of the cyclic voltammetry are significant in obtaining the desired information and can be altered to provide valuable insight into the electrochemical behaviour of a system. While cyclic voltammetry is often used to assess the redox behaviour of species in solution, it can also be utilised to investigate the kinetics of electron transfer at an electrode surface while also evaluating the electrochemical properties of conductive materials and electrocatalysts. For the applications and experiments within this work, known redox-active molecules will be used to assess the activity, stability, and kinetics of MXenes as electrocatalysts.

While cyclic voltammetry sweeps both forwards and backwards in the defined potential window while recording the current response, Linear sweep voltammetry (LSV) sweeps linearly in only one direction, transforming species A to species B via electron transfer without the subsequent reformation of A.¹¹⁵ This technique is particularly useful for quickly determining the overpotential required for reduction reactions, allowing the rapid evaluation of electrocatalysts.

2.2.3 Chronoamperometry

Chronoamperometry is a potentiostatic technique used to measure the current response (amperometry) of a system at a fixed potential as a function of time (chrono).¹¹⁶ This technique is primarily used for electrolysis experiments at fixed potentials, therefore in a three-electrode configuration with a reference electrode and can be utilised to evaluate the activity and selectivity of a catalyst by performing chronoamperometry over a range of potentials and analysing product distribution.

2.3 Product Analysis Techniques

2.3.1 Gas Chromatography

Gas chromatography (GC) is a useful analytical technique for the identification of gas-phase CO₂RR products. In principle, a gas sample is injected into the inlet before it is vapourised and carried through a column by an inert carrier gas. The individual components of the sample mixture will interact differently with the stationary phase of the column, causing them to be retained at different rates.¹¹⁷ These now-separated components will then be detected as they elute from the column, with different detectors able to qualify and quantify different products. Traditionally, one of two detectors is found in a GC system - a thermal conductivity detector (TCD) which is able to qualify inorganic gases, such as CO₂, oxygen, and hydrogen; and a flame ionisation detector (FID) which can detect organic compounds such as hydrocarbons and alcohols. In recent years barrier ionisation discharge (BID) detectors have emerged as promising alternatives due to their ability to provide a universal response to a broad spectrum of compounds including both inorganic gases and organic compounds. Moreover, BID detectors have been reported to exhibit much higher sensitivities compared to TCDs and FIDs, particularly for low-concentration analytes. GC was performed utilising a Shimadzu 2030 equipped with a dielectric-barrier ionisation detector (BID) and ResTek Shin Carbon ST 80/100 column.

2.4 MXenes Samples

Throughout this body of work, 3 different samples of Ti₃C₂T_x were obtained and used. These are in exception to the synthesised MXenes presented in Chapter 3. The MXene sample used in each individual experiment will be highlighted in the relevant section for each experiment, denoted as one of the following.

Ti₃C₂T_x^{PM} – This MXene sample was obtained in Jan 2020 and was provided by Phil Maughan of Lancaster University.

Shortly following the procurement of this material, the global COVID-19 pandemic halted research. Following the reopening of labs at Lancaster University, Ti₃C₂T_x MXene provided by P. Maughan was subject to SEM characterisation in Dec 2020.

The resulting images show a significantly layered material with infrequent signs of delamination. The interlayer spacing of the sheets appeared to be significantly less than expected for MXene materials. Shortly after the imaging of these materials, a new MXene sample was sought to contrast both the morphology and physical properties of both materials.

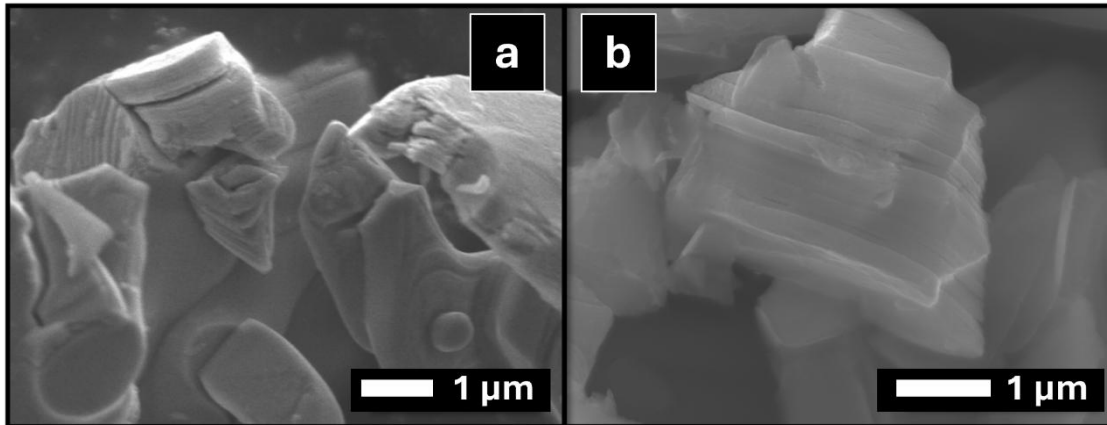


Figure 2.2 – SEM images of $\text{Ti}_3\text{C}_2\text{T}_x^{\text{PM}}$ at a) x 15,000 b) x 20,000

$\text{Ti}_3\text{C}_2\text{T}_x^{\text{NB}}$ – This MXene sample was obtained in Apr 2021 and was provided by Dr Nuno Bimbo, formerly of Lancaster University.

The $\text{Ti}_3\text{C}_2\text{T}_x^{\text{NB}}$ MXene provided by Dr Nuno Bimbo had been synthesised via the $\text{LiF} + \text{HCl}$ etching method detailed herein by Dr Phil Maughan and Dr Luc Bouscarrat of Lancaster University Engineering Department.

Following the procurement of the new MXene powder sample, SEM images were obtained. The resulting images varied drastically compared to those previously obtained for $\text{Ti}_3\text{C}_2\text{T}_x^{\text{PM}}$. Throughout the sample, distinct layering was observed with large interlayer spaces highlighting the edge places of the ML-MXenes present in the sample. Upon higher magnification, individual MXene layers can be seen with interlayer spacing varying significantly throughout the sample. It was apparent that the newly obtained sample was a MXene of significantly higher quality than previously observed if the previous sample was in fact MXene.

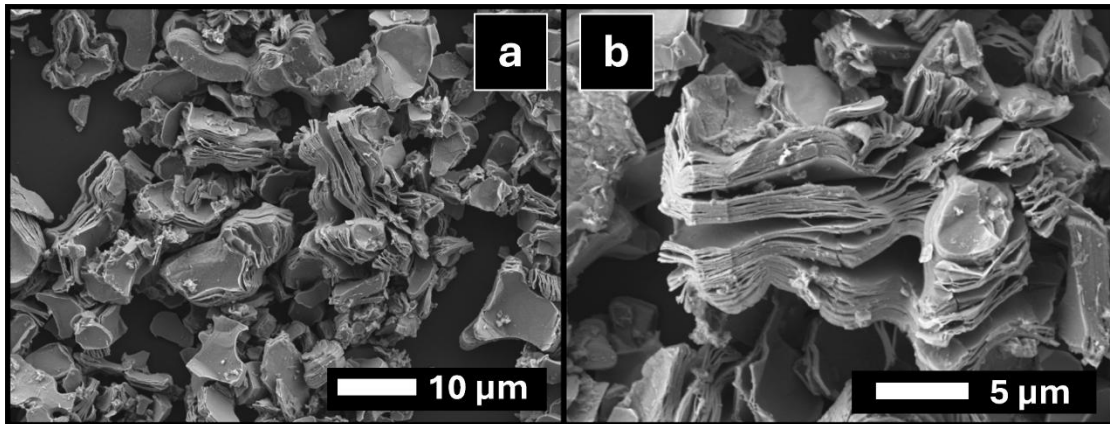


Figure 2.3 – SEM images of $Ti_3C_2T_x^{NB}$ at a) x 1,600 b) x 3,700

BET surface area analysis was conducted on the new $Ti_3C_2T_x^{NB}$ and compared to the commercial Ti_3AlC_2 MAX phase supplied by Dr Nuno Bimbo.

Sample	BET Surface Area (m^2/g)
$Ti_3AlC_2^{CU}$ MAX Phase	77.22
$Ti_3C_2T_x^{NB}$ MXene	1025.78

Table 2.1 – Calculated specific surface areas via BET N_2 sorption measurements

As seen from their calculated surface areas, there is a substantial difference between the MAX and MXene samples, with the MXene displaying a vast surface area. This suggests significant levels of delamination are seen, with large interlayer spacing present which corroborates well with the SEM imaging previously discussed.

$Ti_3C_2T_x^{CM}$ – This MXene was obtained in June 2023 and is an HF-etched commercial sample provided by Laizhou Kai Kai Ceramic Materials Co., Ltd. with the assistance of Dr Nuno Bimbo, formerly of Lancaster University.

Towards the end of this body of work, a MXene commercial sample was procured with the help of Dr Nuno Bimbo. Due to recent price decreases, the affordability of MXene commercial samples makes them an economically viable solution to the replacement of HF synthesis. Scanning electron microscopy images were taken of the commercial MXene powder.

The SEM images obtained present unprecedented levels of layering, unseen in any previously characterised samples. The overall sample showed particles of varying sizes with the largest exceeding 20 μm in diameter. The interlayer spacing was significant, however, individual MXene flakes were visible more so than in the

previous samples. From initial observations, the etching solution appears to have a significant impact on the resulting MXene material, with HF etching producing the highest quality MXenes observed of a large, defect-free nature.

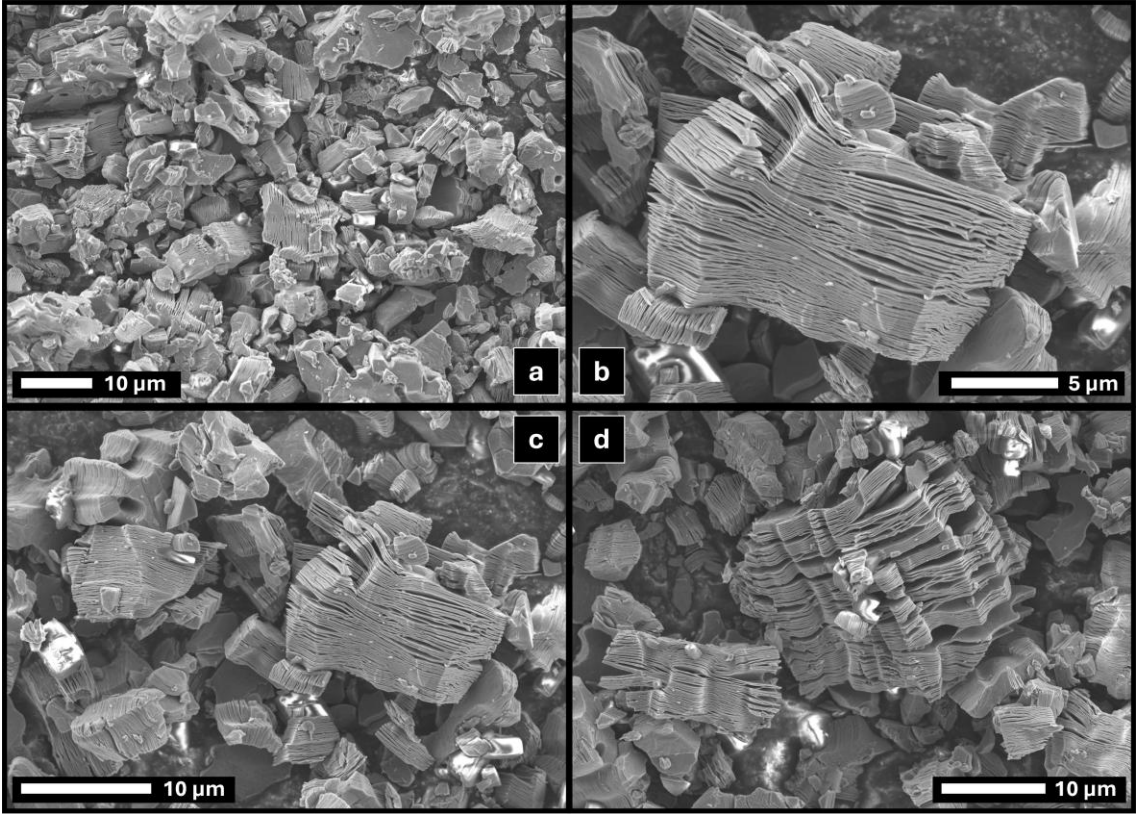


Figure 2.4 – SEM images of a commercial $Ti_3C_2T_x^{CM}$ powder MXene at a) x 1,100 b) x 1,600 c) 2,000 d) x 3,300

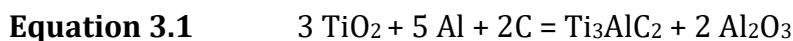
3 Max Phase and MXenes

3.1 Introduction

3.1.1 Ti₃AlC₂ MAX Phase

The quality of a MAX phase precursor has been reported to directly influence the quality of the resulting MXene.¹¹⁸ Impurities or defects in the precursor material can lead to compromised properties and significant defects in the resulting MXene, often promoting severe oxidation at defect sites following synthesis.

In 2016, Barsoum et al. reported the fabrication of high-quality Ti₃AlC₂ MAX phase powder via the pressureless sintering of MAX-containing powders.¹¹⁹ Powders of TiO₂, aluminium, and graphite were mixed in varying stoichiometric ratios with the goal of synthesising Ti₃AlC₂ via the following reaction:



The mixed powders were then heated to 1500 °C at a rate of 10 K/min under flowing Ar for 2 hours. The resulting powders contained various amounts of the desired Ti₃AlC₂ and Al₂O₃, TiC, and Al₃Ti impurities. Barsoum reported that an increase in the Al-content was beneficial to the formation of Ti₃AlC₂ thus reducing the impurities present, which was concurrent with the earlier findings of Hendaoui in 2008.¹²⁰

It was later reported that the use of TiO₂ as a precursor material in MAX phase synthesis introduces challenges relating to the reduction of TiO₂ to Ti, typically requiring high temperatures and potentially leading to the formation of unwanted secondary phases.¹²¹

An alternative synthetic method, proposed by Maughan in 2019, detailed the synthesis of Ti_3AlC_2 MAX Phase from an alternative precursor powder mixture of Ti, Al, and TiC in a 1:1.2:1.9 molar ratio.¹²² This powder mixture was calcined at 1,350 °C for 2 hours under flowing Ar with a heating rate of 5 K/min; which is notably 150 °C lower than the aforementioned Barsoum method. The resulting MAX phase was reported to be of high purity, confirmed by large characteristic Ti_3AlC_2 peaks with few impurity peaks present in the obtained XRD (X-ray diffraction) pattern. This method published by Maughan is of great relevance to obtaining a low-cost MXene as the calcination temperature, and consequentially the cost is drastically lower. Moreover, a recent study by Kim & Lim assessed the quality of commercial MAX phases synthesised from elemental Ti, Al, and TiC and those synthesised from a TiO_2 -containing mixture.¹²³ A significantly higher number of oxides were found in the TiO_2 -derived MAX phase, reported to exhibit poor microstructural characteristics, thus negatively influencing the MAX phase's properties.

It is well reported that calcination temperature plays a crucial role in MAX phase synthesis. In 2006, Peng evaluated key influential factors of a Ti_3AlC_2 synthesis, including holding temperature and soaking time.¹²⁴ Additionally, the MAX-containing powder was also evaluated to determine the optimal precursor materials. The MAX-containing powder mixtures selected were TiC/Ti/Al in a 2:1:1 molar ratio denoted 2TiC/Ti/Al; and Ti/Al/C in a 3:1:2 molar ratio denoted 3Ti/Al/2C. Firstly, Peng employed DTA analysis on the two powder mixtures and reported a vast contrast between the DTA curves obtained. For the 3Ti/Al₂C system, a sharp exothermal peak was reported at around 650 °C, which was been attributed to the thermal explosive reaction between Ti and C. This observed peak was not present in the 2TiC/Ti/Al curve and instead was an endo- and exothermal peak of much smaller magnitude indicating the melting of Al and formation of TiAl respectively. Peng concluded that the 2TiC/Ti/Al powder system yields a more suitable and promising material to avoid intense thermal explosion during synthesis.

Using the 2TiC/Ti/Al powder mixture Peng next evaluated the effects of holding temperature on the resulting MAX phase, using the temperature range 1200 °C to 1500 °C. It was reported that the impurity peaks for TiC were comparatively least intense for temperatures between 1300 °C and 1400 °C. Additionally, Ti_2AlC peaks

were present at a holding temperature of 1200 °C but absent at 1300 °C indicating a reaction between Ti_2AlC and TiC to generate Ti_3AlC_2 at 1300 °C. For these reasons, the temperature between 1300 °C and 1400 °C was chosen as the optimal temperature range for Ti_3AlC_2 synthesis. Finally, the effects of soaking time were observed at 1300 °C for up to 60 minutes. Peng reported no obvious change in the relative intensity of TiC peaks between 15 and 30 minutes; however, increased TiC formation was observed when the soaking time was increased to 60 minutes. Peng concluded that a high-purity Ti_3AlC_2 MAX phase could be synthesised successfully using a 2 $TiC/Ti/Al$ powder blend which was calcined at 1300 °C -1400 °C for 15-30 minutes.

To reduce the overall cost of the MXene synthesis *ab initio*, synthesising the Ti_3AlC_2 MAX phase can avoid the relatively high cost of commercially available MAX powders while also minimising the risk of impurities that typically arise from commercial production.¹²⁵

To assess the quality and intrinsic properties of the subsequent Ti_3C_2 MXenes, Ti_3AlC_2 MAX phase was synthesised according to both the Barsoum and Maughan methods for comparative purposes. Commercial samples of Ti_3AlC_2 were also obtained and characterised for comparison.

3.1.2 Ti_3C_2 MXene Synthesis and Surface Functionalisation

Due to the hazardous nature of an HF-containing etchant solution for MXene synthesis, the intrinsic cost of a commercial MXene sample (Jan 2020) is in excess of £500 per gram. Therefore, minimising costs requires researchers to take on the inherent risks of synthesis. Hydrofluoric acid (HF) is widely recognised as one of the most hazardous chemicals, with even low concentrations leading to severe injuries and potential fatalities despite small affected bodily surface areas.¹²⁶⁻¹²⁸ It is therefore in the interest of minimising risk to the user, to reduce, and in some cases, remove the presence of HF in the synthetic procedure.

As previously mentioned, in 2014, Ghidui et al. reported MXene synthesis via the in-situ generation of HF via the addition of LiF to an HCl solution.¹²⁹ This method has since been adopted by a significant number of studies, making the etching of MXenes significantly more accessible. It is strongly suggested within the literature that in

order to retain a MXene's superior physical and chemical properties, they should be utilised directly following synthesis, as the MXene structure may be compromised, and oxidation can occur.

Alternatively, the alkaline etching of MXenes provides an opportunity to negate any HF usage whether direct addition or *in-situ* generation. This method, first reported by Li et al., also carries significant hazards by employing high pressure and significantly high alkaline concentrations to etch the MXenes.⁶³ Despite the soaking time of this method being reported as 12 hours, there is no documented justification for this. Herein we report the effects of soaking time on the MXene purity following a 27.5 M NaOH etching at 270 °C, with scope to improve upon the 92% Ti₃C₂ purity previously reported.

Finally, the option to store MXenes stably as dry powders presents significant benefits over using freshly synthesised 'wet' MXenes. Firstly, the ability to store MXenes negates the necessity of repeating hazardous syntheses. Additionally, the presence of moisture has been reported to promote TiO₂ formation at defect sites on MXene basal planes,¹³⁰ whereas storing the materials as a dry powder avoids moisture entirely. The handling of MXene powders, whether synthesised in-house or as commercial samples, is scarcely documented in the literature. The overwhelming majority of experimental MXene literature evaluates the materials directly following synthesis, with very few reports on how to handle, utilise, and modify MXene powders for bespoke applications. With the cost of commercial MXene powder at an all-time low, there is an ever-growing need for the effective delamination, functionalisation and utilisation of powder MXenes.

The functionalisation of a MXene surface has been identified as a key parameter in the optimisation of these materials for intended applications. Typically, MXenes are functionalised during synthesis, as the etching process exposes previously occupied surface sites on the basal planes of MXene sheets.¹³¹ While the nature of the etching solution can be modified to introduce specific surface terminations, this methodology cannot be utilised for MXenes in powder form as a re-etching may significantly damage the material.¹³² There is a noticeable scarcity of reports within MXene literature regarding the surface functionalisation of powder samples, a growing area in which significant attention may soon be drawn due to the drastic

price reduction in MXenes over recent years. As hydroxyl (-OH) terminated MXenes have shown significant promise in electrocatalytic applications, herein we report the surface functionalisation of Ti_3C_2 with -OH terminations via various synthetic methods including acid, base, and ozone treatments.

3.2 Materials and Methods

3.2.1 Reagents and Experiments

Titanium, aluminium, and carbon powders were purchased from Sigma Aldrich (UK). Titanium carbide and titanium dioxide were purchased from Fisher Scientific.

Hydrochloric acid (HCl, 37%), sodium hydroxide (NaOH) and lithium fluoride were purchased from Fisher Scientific (UK). Ti_3AlC_2 MAX Phase was received from Dr Nuno Bimbo, originally purchased from Carbon Ukraine (Ukraine).

A 100 mL hydrothermal synthesis autoclave reactor with a 10 MPa blow-off seal and polyphenyl polymer liner was purchased from Cambridge Energy Solutions (UK)

Dry ozone treatments were performed using a Novascan PSD Series UV Cleaner. Wet ozone treatments were performed using a Triogen O₃ Ozone system.

Parameters for characterisation methods are detailed in Chapter 2.1.

3.2.2 MAX Phase Synthesis

3.2.2.1 Maughan Method

With the aim of producing high-purity Ti_3AlC_2 , a pressureless synthesis method was followed according to P. Maughan.¹²² Powders of Ti, Al, and TiC were mixed in stoichiometric molar ratios of 1:1.2:1.9 in a pestle and mortar for 5 minutes under an oxygen-free atmosphere. The blended powders were then heated at 5 K/min before reaching a soaking temperature of 1200 °C** and held for 2 hours under flowing Ar before being cooled to room temperature. The sintered compacts were finally crushed in a mortar and pestle and ground for 5 minutes to achieve uniform particle size.

*Due to equipment limitations; a maximum temperature of 1200 °C was used instead of 1350 °C as reported by Maughan.

** Following equipment acquisition, the soaking temperature was increased to 1350°C where indicated.

3.2.2.2 Barsoum Method

A second MAX phase was synthesised according to the Barsoum literature method, with adaptations made due to equipment limitations. The method reported by Barsoum utilises a holding temperature of 1500 °C, which was reduced to 1200 °C for the purposes of this study. Powders of TiO₂, Al, and C were used in a stoichiometric molar ratio of 3:1:2.¹¹⁹ The powdered mixture was ground in a pestle and mortar for 5 minutes under an oxygen-free environment. The blended powders were then heated at 5 K/min before reaching a soaking temperature of 1200 °C and held for 2 hours under flowing Ar before being cooled to room temperature. The sintered compacts were finally crushed in a mortar and pestle and ground for 5 minutes to achieve uniform particle size.

3.2.3 Acidic Etching of Ti₃AlC₂ to Ti₃C₂T_x via *in-situ* HF generation

An etching solution was prepared via the addition of 1.6g of lithium fluoride to hydrochloric acid [9 M, 20 mL] in a 250 mL PTFE container. 1 g of Ti₃AlC₂ MAX phase powder was slowly added to the etching solution. Etching was carried out for 30 h at 50 °C. The resulting dispersion was washed with deionised water by repeated centrifugation at 3500 rpm for 5 min per cycle (5 mL of dispersion diluted with 45 mL of DI in each centrifuge tube x 4) until self-delamination occurred at a supernatant pH~6. Self-delaminated flakes were then collected by centrifugation at 1500 rpm for 30 min. The dark grey supernatant was further centrifuged at 4500 rpm for 20 min and the sediment containing large MXene flakes was collected.

3.2.4 Fluorine-Free Synthesis of Ti₃C₂OH

Deionised water was first degassed in a sonic bath before being heated to boil and kept for 30 min under flowing Ar. Then, NaOH (55 g) was dissolved in 50 mL of DI in a 100 mL polyphenyl polymer (PPL) liner within an autoclave. After that, 200 mg of Ti₃AlC₂ MAX Phase powder was added to the NaOH solution before the autoclave was sealed and purged with flowing Ar gas. The autoclave was then heated to 270 °C

at a rate of 5 °C/min at kept at temperature for 12 h. Upon completion of the hydrothermal process, the resulting suspension was separated into two layers; a transparent upper layer, which was decanted and disposed of, and a black suspension in the lower layer. This suspension was filtered with a filter membrane (PVDF, 0.055 µm pore size) followed by several washes with DI. The resulting powder was then dried in a vacuum oven at 65 °C for 12 h. Following drying, the newly synthesised powder was cooled to room temperature and used immediately.

3.2.5 Surface Functionalisation of $Ti_3C_2T_x$

3.2.5.1 Acidic and Alkaline Treatments

The surface functionalisation of $Ti_3C_2T_x$ MXene was attempted via alkaline and acidic treatments following Maughan's suggested method.⁵

Firstly, MXene (200 mg) was added to a NaOH solution (1M, 40 mL) before being stirred for 4 hours at 300 rpm. Following alkaline treatment, the supernatant was decanted and the material was washed with DI via centrifugation (5 x 40 mL) before drying. The MXene was then immersed in an HCl solution (1M, 40 mL) before being stirred for 4 hours at 300 rpm. Following acidic treatment, the supernatant was decanted and the material was washed with DI via centrifugation (5 x 40 mL) before drying.

3.2.5.2 Wet Ozone Treatment

Firstly, MXene (50 mg) was dispersed in deionised water (Xx mL) via manual agitation. Once fully dispersed, ozone was bubbled through the container at a rate of xx mL/min for XX min. Following ozonation, the MXene was xx filtered and dried in a xx oven for xx hours. The ozone-modified MXene sample was then subject to Raman spectroscopic analysis

3.2.5.3 Dry Ozone Treatment

Firstly, a 5 mg/mL MXene ink was prepared via the addition of $Ti_3C_2T_z$ (25 mg) to nitrogen-sparged deionised water (5 mL). The ink was then probe sonicated for 30 minutes, pulsing 6 seconds on, and 10 seconds off. 100 uL of the MXene ink was then drop-cast onto a Sigracell plate and left to dry under ambient conditions. Once dry, the modified Sigracell plate was placed in a UV ozone cleaner before being sealed. Flowing compressed air was then attached to the cleaner to provide a constant

supply of oxygen. Finally, the UV cleaner was turned on for a total of 30 minutes, with an additional 30 minutes of compressed air flowing over the sample to dissipate any remaining ozone. The ozone-modified MXene was then subject to Raman spectroscopy and XPS analysis.

3.3 Results and Discussion

3.3.1 – MAX Phase Synthesis

A Ti_3AlC_2 MAX phase was synthesised according to two separate methods referred to herein as the Maughan method and Barsoum method yielding M-MAX and B-MAX respectively. Both methods detail the pressureless sintering of homogenous elemental powders mixed in stoichiometric ratios.

Scanning electron microscope (SEM) images taken of the synthesised MAX phases B-MAX and M-MAX are presented in Fig 3.1.

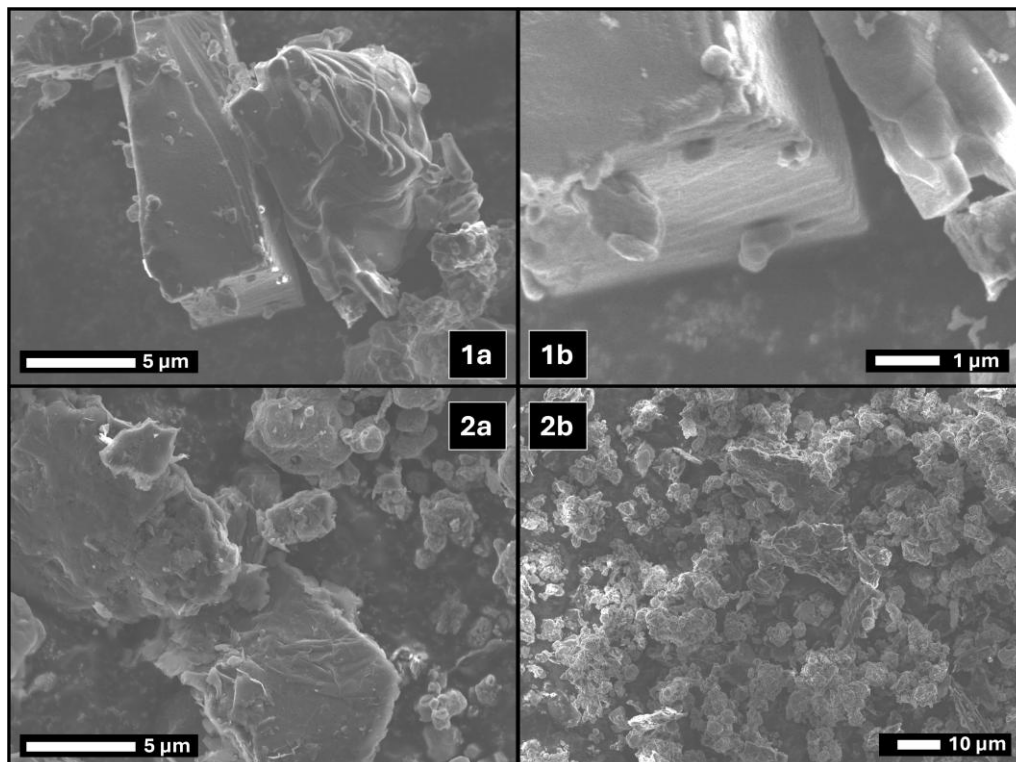


Figure 3.1 – SEM Images of 1) M-MAX at a) $\times 5000$ b) $\times 15,000$ 2) B-MAX at a) $\times 5000$ b) $\times 1000$
At $\times 5000$ magnification, there are noticeable disparities between the two synthesised MAX phases. When considering M-MAX at $\times 5000$ magnification, distinct layering can be seen throughout the sample despite the layers appearing laminated.

A difference in contrast outlining the various layers can be attributed to the A, M, and X elements present in the MAX phase structure, suggesting a successful MAX phase synthesis. At an increased magnification of $\times 15,000$, the layered structure of M-MAX becomes more distinguishable, and layers of higher contrast can be seen distributed evenly throughout the structure. It is worth noting that the M-MAX particle size appears to be around 10-15 μm , which is generally considered a small particle size in relation to MXene synthesis. When considering B-MAX at $\times 5000$, unlike M-MAX, no such layering can be seen. Larger particles present in the sample appear to have uneven facets with rippling and tearing present on the basal planes. In addition, the overall particle size appears to be far less uniform with particle size ranging from $<1 \mu\text{m}$ to 20 μm . The amorphicity of the B-MAX sample suggests an incomplete synthesis of the MAX phase. Due to the variation in the particle size of the B-MAX sample, a lesser magnification of $\times 1000$ was used to gain insight into the homogeneity of the sample. From the resulting images, it was apparent that the particle size distribution was too broad and therefore the B-MAX was deemed unsuitable for use in a MXene synthesis. Further characterisation would be necessary for both MAX phases to identify both the ideal structure and any impurities/precursor materials present in the samples.

Coupled electron dispersive x-ray spectroscopy (EDX) was utilised alongside SEM in order to identify the elemental species present in the MAX phase samples; thus, aiding in the identification of impurities and unreacted elemental powders.

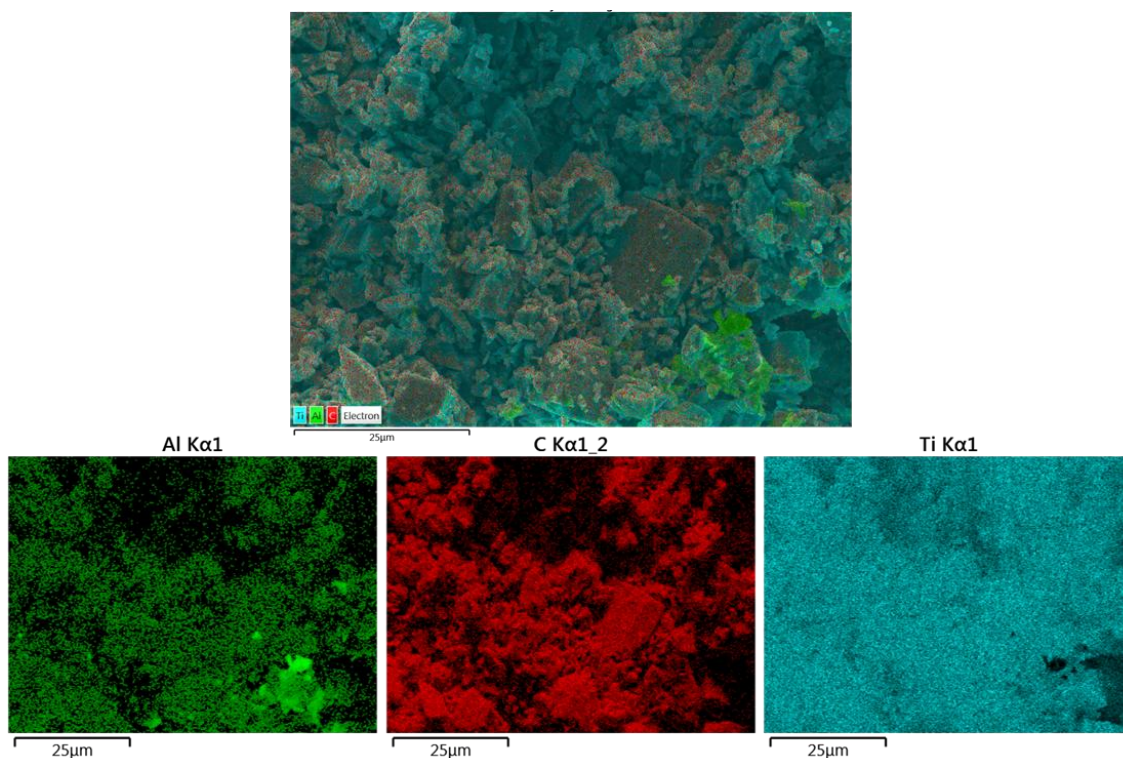


Figure 3.2 - EDX Analysis of Ti_3AlC_2 [M-MAX] a) Al, C, and Ti (Combined), b) aluminium, c) carbon, d) titanium. Scale bars represent 25 μm .

EDX analysis was performed on M-MAX at a low magnification of $\times 250$, shown in Figure 3.2, to gain insight into the homogeneity of the sample and provide elemental analysis representative of the sample. Individual EDX mappings for Al, C, and Ti were taken and then combined to highlight any element-rich regions of the sample. Towards the lower-right quadrant of the observed area, Al (green) can be seen localised in large quantities indicating an Al impurity – likely originating from the unreacted Al elemental powder. Due to the insolubility of aluminium powder, this impurity may be challenging to remove from the sample entirely and may lead to undesirable reactions during MXene synthesis. If following the in-situ generation of HF synthesis method; excess aluminium from an impure MAX phase may scavenge fluoride ions in the solution, thus reducing the concentration of HF. Excluding the aforementioned Al impurities, the M-MAX sample can be considered predominantly homogenous with Al, C, and Ti all present in significant quantities throughout the sample. Notably, the combined mapping appears mainly blue which is attributed to the titanium outer layers of the MAX phase.

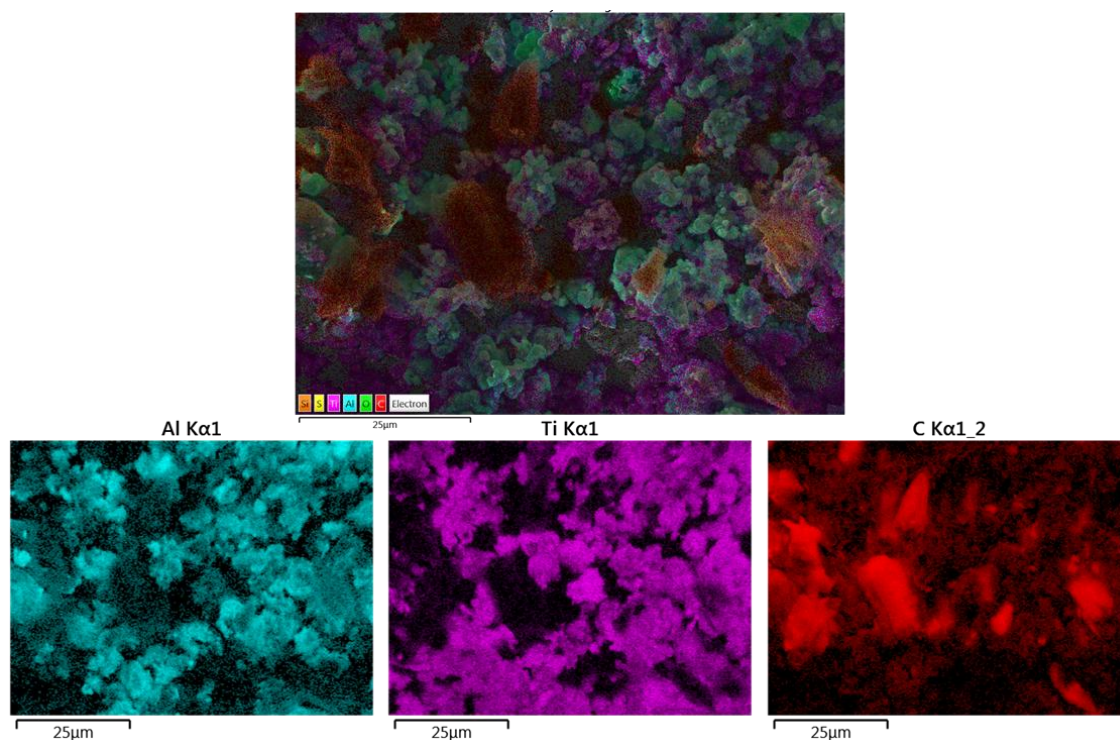


Figure 3.3 - EDX Analysis of Ti₃AlC₂ [B-MAX] a) Al, Ti, and C (Combined), b) aluminium, c) titanium, d) carbon. Scale bars represent 25 μm.

EDX mapping of the B-MAX sample at $\times 250$ magnification, shown in Figure 3.3, supports a previously suggested unsuccessful synthesis. When considering the overall mapping, distinct localisations of all three observed elements, Al, Ti, and C, can be seen indicating separate elemental species. When comparing the individual elemental mapping, there are very few similarities in structure and size across all three species. Although the MAX phase material appears absent in B-MAX, structural characterisation will assist in identifying the nature of impurities/precursor material.

The X-ray diffraction (XRD) patterns of the Ti₃AlC₂ MAX phases known as B-MAX and M-MAX herein are shown in Figure 3.4.

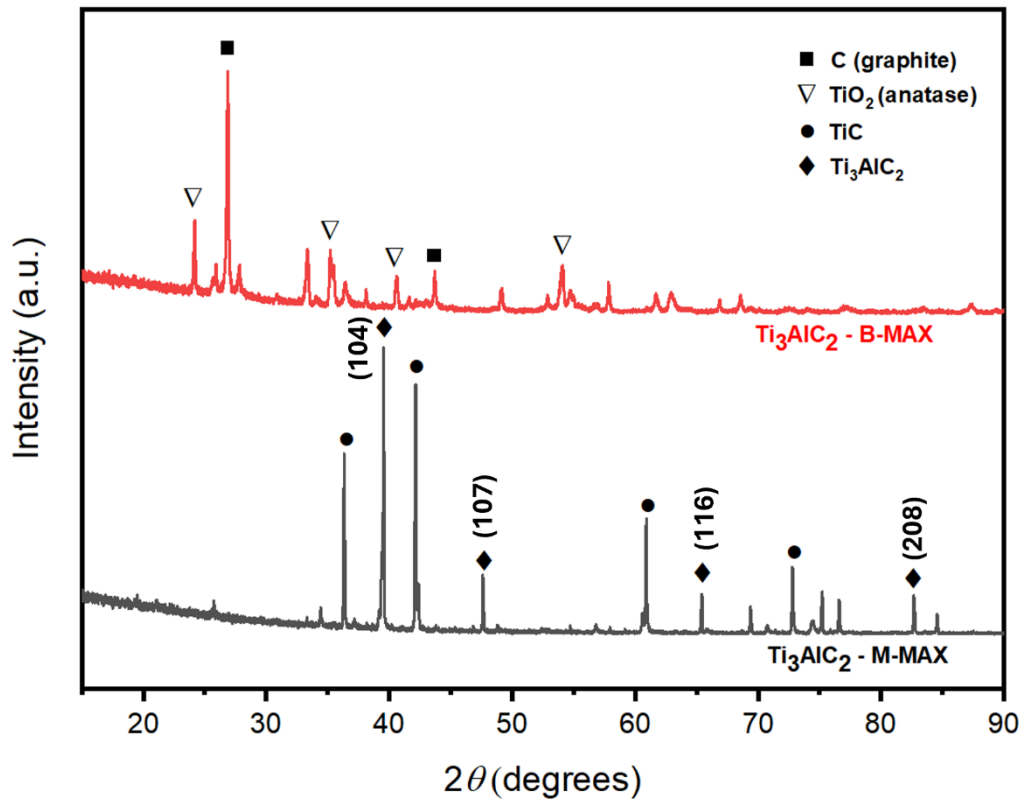


Figure 3.4 - XRD diffraction pattern for a) red - Ti_3AlC_2 [B-MAX], b) black - Ti_3AlC_2 [M-MAX]

From the B-MAX XRD pattern of Figure 3.4 (top), it is evident that the primary characteristic Ti_3AlC_2 peak, typically observed at $2\theta = 39^\circ$, is absent. In addition to this, characteristic peaks observed in literature at 48° , 65° , and 83° are also missing. The peaks that are observed within the XRD pattern at 28° and 44° ; and 24° , 35° and 55° correspond to literature values cited for graphite powder and TiO_2 (anatase) respectively. From the absence of key characteristic MAX phase peaks, alongside the presence of precursor material peaks; it is strongly suggested that the synthesis was unsuccessful at 1200°C . It is noteworthy that the synthetic method employed here substitutes a temperature which is 300°C less than recommended, due to equipment limitations.

The XRD pattern shown in Figure 3.4 (bottom) for M-MAX shows a large characteristic peak at $2\theta = 39^\circ$ with a smaller shoulder peak on its left at 38° . When observing the literature, it is typical in less-pure samples to see two large peaks at near overlapping positions around 39° ; which are assigned to Ti_3AlC_2 and Ti_2AlC on the left and right respectively. As the shoulder peak is present on the left-most side of the main peak at 39° , it can be assumed that the larger peak indicates the presence

of Ti_2AlC , with Ti_3AlC_2 also being detected at a lower peak intensity. Other key peaks observed at 48° , 65° , and 83° , confirm the successful synthesis of Ti_3AlC_2 ; however, due to the relative intensity of said peaks, the purity of the Ti_3AlC_2 sample is assumed to be relatively low. Additional peaks of moderately high intensity can be seen at 36° , 42° , 61° , and 74° . These peaks are attributed to significant amounts of unreacted precursor TiC still present within the sample, indicating only a partially successful synthesis of the MAX phase. As with the synthesis of B-MAX, a lower holding temperature (1200°C) was used than specified in the original method (1350°C) due to equipment limitations, therefore achieving a pure sample of Ti_3AlC_2 was especially challenging.

Although a MAX phase was achieved via the Maughan method, large quantities of TiC and Al were present in the sample as identified with XRD and SEM/EDX respectively. As a high temperature has been identified as a key experimental parameter,¹³³ it is crucial to observe the effects of a high-temperature MAX phase synthesis and evaluate the properties of the resulting material

Following the procurement of a high-temperature furnace, a Ti_3AlC_2 MAX phase synthesis was attempted at 1350°C using the Maughan method. Following calcination, a white material was present on the surface of the newly synthesised MAX phase, assumed to be an oxide layer. EDX analysis (Figure 3.5) was performed on the white material which revealed an elemental composition of 47.3 wt% oxygen and 44.4 wt% aluminium, with carbon and titanium making up the remaining ~ 8 wt%. The elemental composition of the oxide layer suggests significant aluminium oxide (Al_2O_3) formation due to the introduction of oxygen in the calcination process.

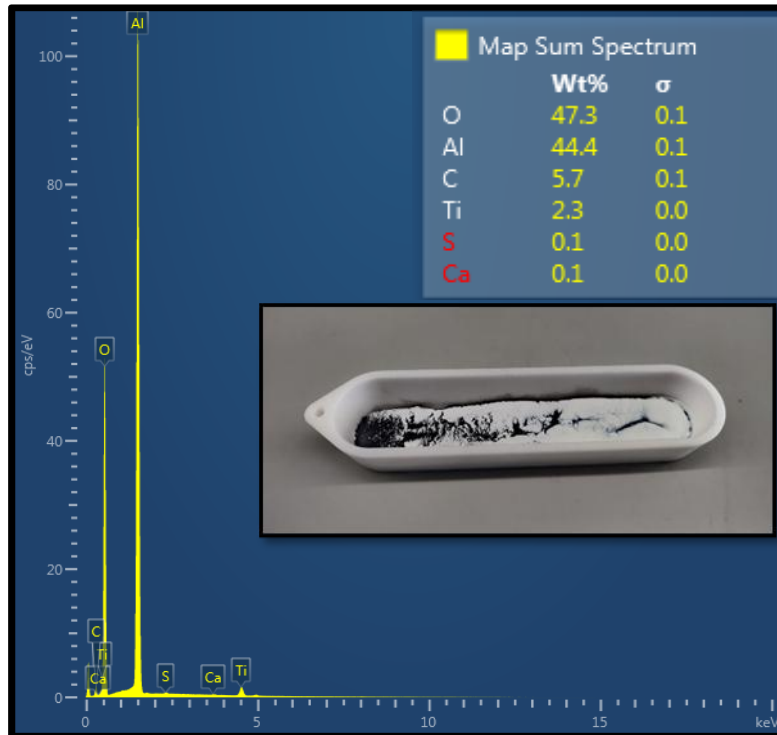


Figure 3.5 – Elemental composition of the surface oxide layer post-synthesis, MAX phase [Maughan method, 1350 °C]. Inset – Image of Maughan method MAX phase following calcination.

Once the oxide layer was removed, the synthesised MAX phase was ground and characterised via XRD and SEM imaging.

For comparison, a commercial Ti_3AlC_2 MAX phase was purchased from Carbon Ukraine. The X-ray diffraction pattern for the newly synthesised MAX phase, shown in Figure 3.6, presented characteristic MAX phase peaks at 9° , 34° , 39° , 42° , and 60° corresponding to the facets (002), (101), (104), (105), (110) respectively. The MAX phase peak positions in $\text{Ti}_3\text{AlC}_2^{1350}$ and their relative intensity are near-identical to those of $\text{Ti}_3\text{AlC}_2^{\text{CU}}$ indicating a successful MAX phase synthesis with a high degree of crystallinity. Supplementary to the MAX phase peaks; impurity peaks can also be seen in the $\text{Ti}_3\text{AlC}_2^{1350}$ diffraction pattern at 36° , 43° , and 61° attributed to a mixture of oxides, TiO_2 and Al_2O_3 , and remaining TiC . Evidently, increasing the calcination

temperature from 1200°C to 1350°C in the Maughan method results in a higher purity MAX phase; with a near complete TiC conversion to Ti₃AlC₂.

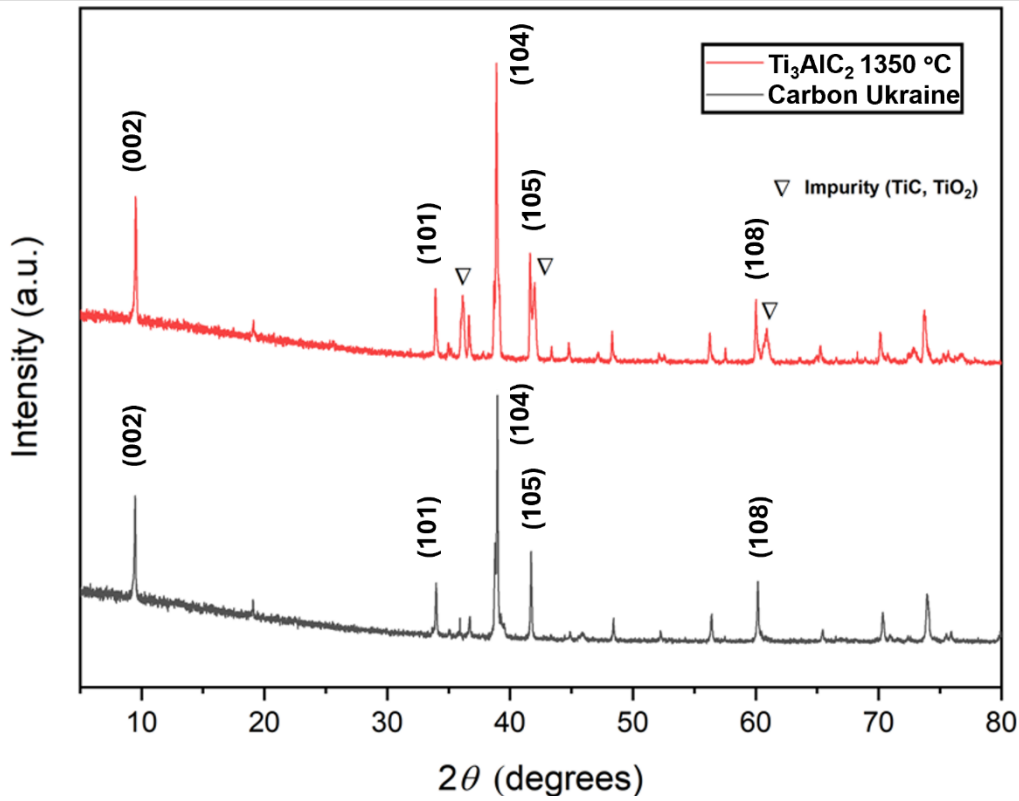


Figure 3.6- XRD diffraction patterns for a) red - Ti₃AlC₂¹³⁵⁰ b) black - Ti₃AlC₂^{CU}

SEM images of Ti₃AlC₂¹³⁵⁰ (Figure 3.7) show a high level of crystalline material with distinct layering present throughout the sample. The particle size distribution appears relatively wide; with particles ranging from >1 μm – 20 μm, possibly due to the varied particle size of the elemental powders. To avoid a large particle size distribution, the ball-milling of precursor powders may be an alternative solution, however, due to the reactivity of fine aluminium powder and equipment limitations, it was decided against.

TGA/DSC curves obtained for both Ti₃AlC₂¹³⁵⁰ and Ti₃AlC₂^{CU} (Figure 3.8) show a steady increase in mass as temperature increases. A total mass gain of 16% is achieved at 1250°C and 1500°C for Ti₃AlC₂^{CU} and Ti₃AlC₂¹³⁵⁰ respectively attributed to the oxidation of the MAX phase, which begins as low as 400°C. A relatively rapid mass gain occurs for Ti₃AlC₂^{CU} at 400°C when compared to Ti₃AlC₂¹³⁵⁰ suggesting the commercial MAX phase has less oxidation resistance. Notably a sharp exothermic peak around 1200°C is present in the DSC curve for Ti₃AlC₂¹³⁵⁰ which can be

attributed to the formation of Ti_3AlC_2 from elemental powders present following the MAX phase synthesis. Although the corresponding DSC peak is also present in $Ti_3AlC_2^{CU}$, the exothermic process releases considerably less energy – meaning far less unreacted elemental powder is present in the commercial sample.

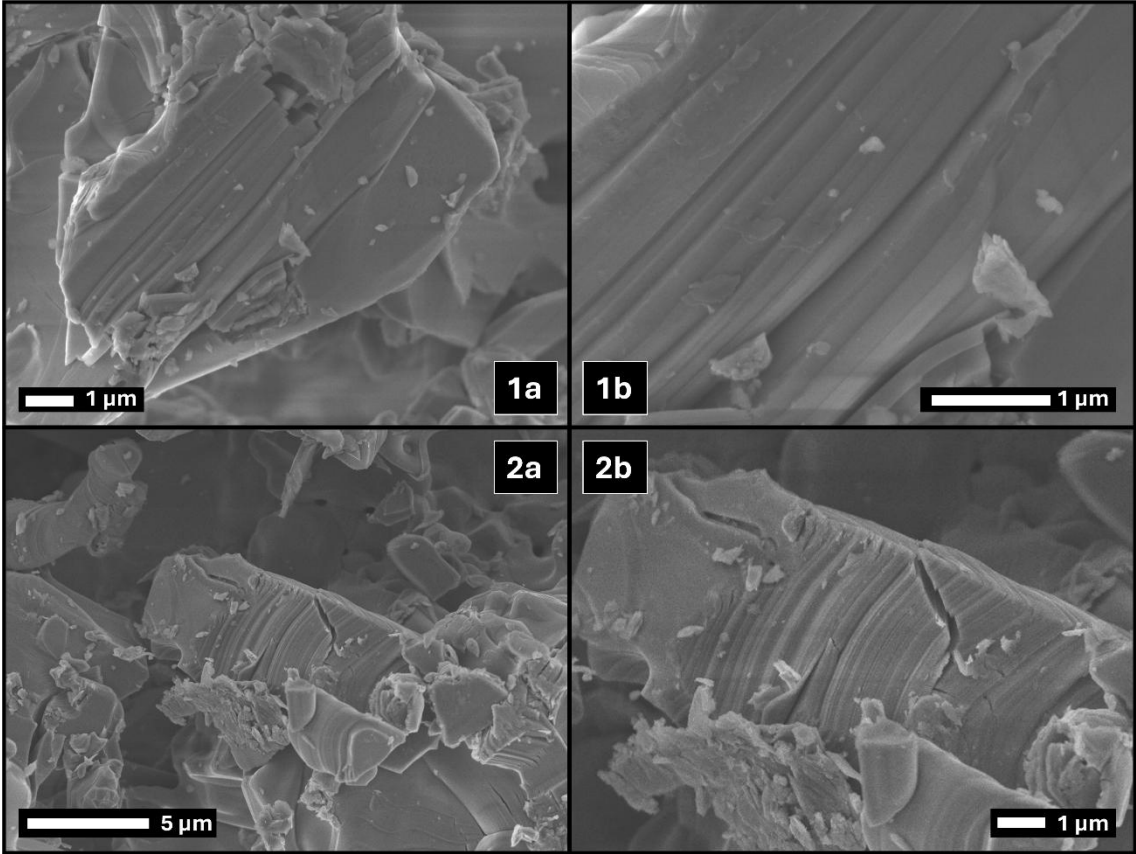


Figure 3.7 – SEM Images of 1) $Ti_3AlC_2^{1350}$ at magnification of a) $\times 10,000$ b) $\times 25,000$, and 2) $Ti_3AlC_2^{CU}$ at magnification of a) $\times 5,000$ b) $\times 10,000$

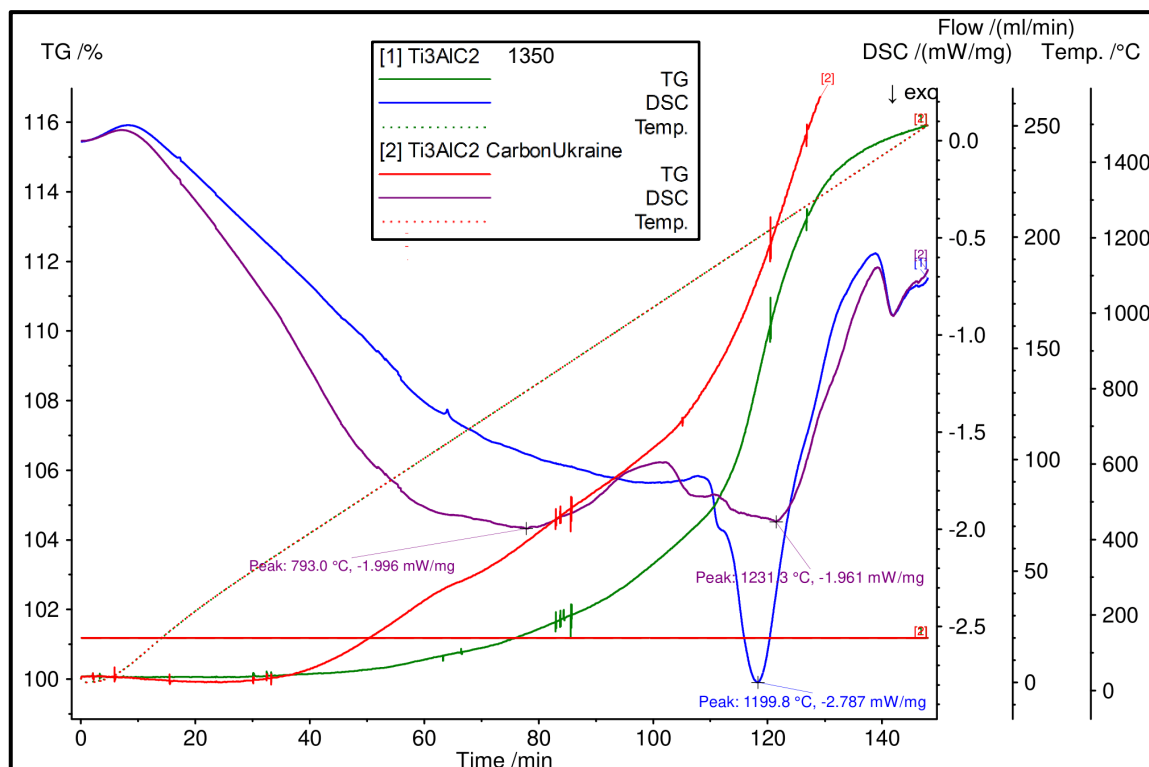


Figure 3.8 - TGA/DSC Curves for 1) $\text{Ti}_3\text{AlC}_2^{1350}$ a) TGA – Green b) DSC – Blue and 2) $\text{Ti}_3\text{AlC}_2^{\text{CU}}$ a) TGA – Red b) DSC – Purple

Although the synthesis of Ti_3AlC_2 at 1350 °C using the Maughan method has proven effective, yielding a highly crystalline MAX phase – the amount of impurity when compared to a commercial sample is considered too high and unsuitable for etching to Ti_3C_2 MXene.

This section details the synthesis of Ti_3AlC_2 MAX phase via differing methods and the challenges associated with MAX phase synthesis. In order for a MAX phase to be successfully etched to a MXene, a high purity is crucial due to the challenging separation of MXene from its parental MAX phase. Using the method described by Maughan et al, we were able to achieve a Ti_3AlC_2 MAX phase – however, due to the presence of unreacted elemental powder following calcination, the sample was deemed unsuitable for MXene synthesis.

3.3.2 Acidic Etching of Ti_3AlC_2 to $\text{Ti}_3\text{C}_2\text{T}_x$ via *in-situ* HF generation

$\text{Ti}_3\text{C}_2\text{T}_x$ was synthesised via the *in-situ* generation of HF from LiF and HCl according to Ghidiu et al.'s method. Due to the presence of both fluoride and chloride ions in the etching solution, the predicted surface termination groups are -O, -OH, -F, and -Cl exclusively.

Following synthesis, the newly etched MXenes were subject to SEM characterisation to assess the morphology of the material, with a particular focus on visible delamination. The resulting SEM images displayed a multitude of particles varying in size and shape with no significant layering present. The larger MAX/MXene particles appear to be covered in a small crystalline deposit in the nanometre range. Despite a select few large particles showing some level of delamination, the overall synthesis can be considered unsuccessful. During the synthesis, a potential equipment malfunction may have prevented the desired temperature from being achieved, therefore, the synthesis was repeated.

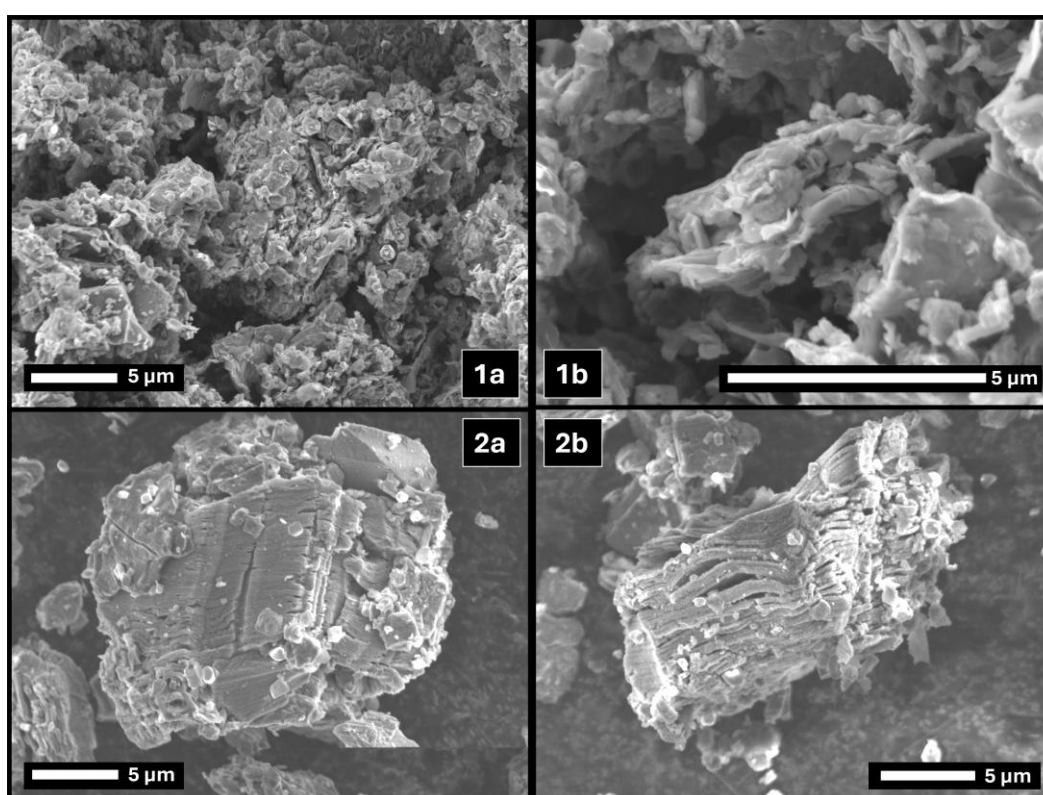


Figure 3.9 – SEM Images of 1) $Ti_3C_2T_x$ 1st synthesis at a) x 3,700 b) x 12,000, and 2) $Ti_3C_2T_x$ 2nd synthesis at a) x 3,700 b) x 4,300

Following a repeat synthesis, the resulting MXene was again subject to SEM characterisation to contrast with the previous unsuccessful MXene synthesis. The resulting images displayed significantly more promise with considerable layering present throughout the entire sample. Partial delamination was also observed within most large MXene particles, likely due to the Li^+ ions present in the etching solution intercalating between MXene sheets. In addition to the ML-MXenes, smaller uniform particles can be seen distributed evenly throughout the sample. These

impurity particles could potentially be metal oxides, carbon-based impurities, or even residual LiF salt particles from inefficient washing steps post-reaction.

XRD analysis was performed for the synthesised $\text{Ti}_3\text{C}_2\text{T}_x$ and is presented in Figure 3.10 in red. Ti_3AlC_2 (black) and $\text{Ti}_3\text{C}_2\text{T}_x^{\text{NB}}$ (blue) are also presented for comparison. Firstly the absence of a sharp characteristic MAX phase peak at 9° indicates the successful etching of Al from the MAX phase to yield $\text{Ti}_3\text{C}_2\text{T}_x$ MXene. Two sharp peaks present in the XRD pattern for the LiF + HCl MXene at 35° and 41° indicate the presence of TiO_2 within the sample, suggesting the formation of defects on the MXene surface during synthesis. At the low-angle region of the spectrum, the characteristic MXene peak present in $\text{Ti}_3\text{C}_2\text{T}_x^{\text{NB}}$ at 6° cannot be seen, perhaps due to it being dwarfed by the increasing signal at lower angles. This characteristic peak is often attributed to the delamination of MXene sheets and represents the interlayer spacing present. The increasing signal at low angles in the newly synthesised MXene may be attributed to the lack of interlayer spacing in the sample.

While the successful synthesis of $\text{Ti}_3\text{C}_2\text{T}_x$ has been demonstrated herein, the presence of TiO_2 impurities suggests that the material is unsuitable for use in electrochemical applications. Due to the oxidative potential of MXenes in aqueous media, any Ti defect sites present on the surface of the synthesised $\text{Ti}_3\text{C}_2\text{T}_x$ will likely assist in the rapid oxidation of the material when used in aqueous applications.

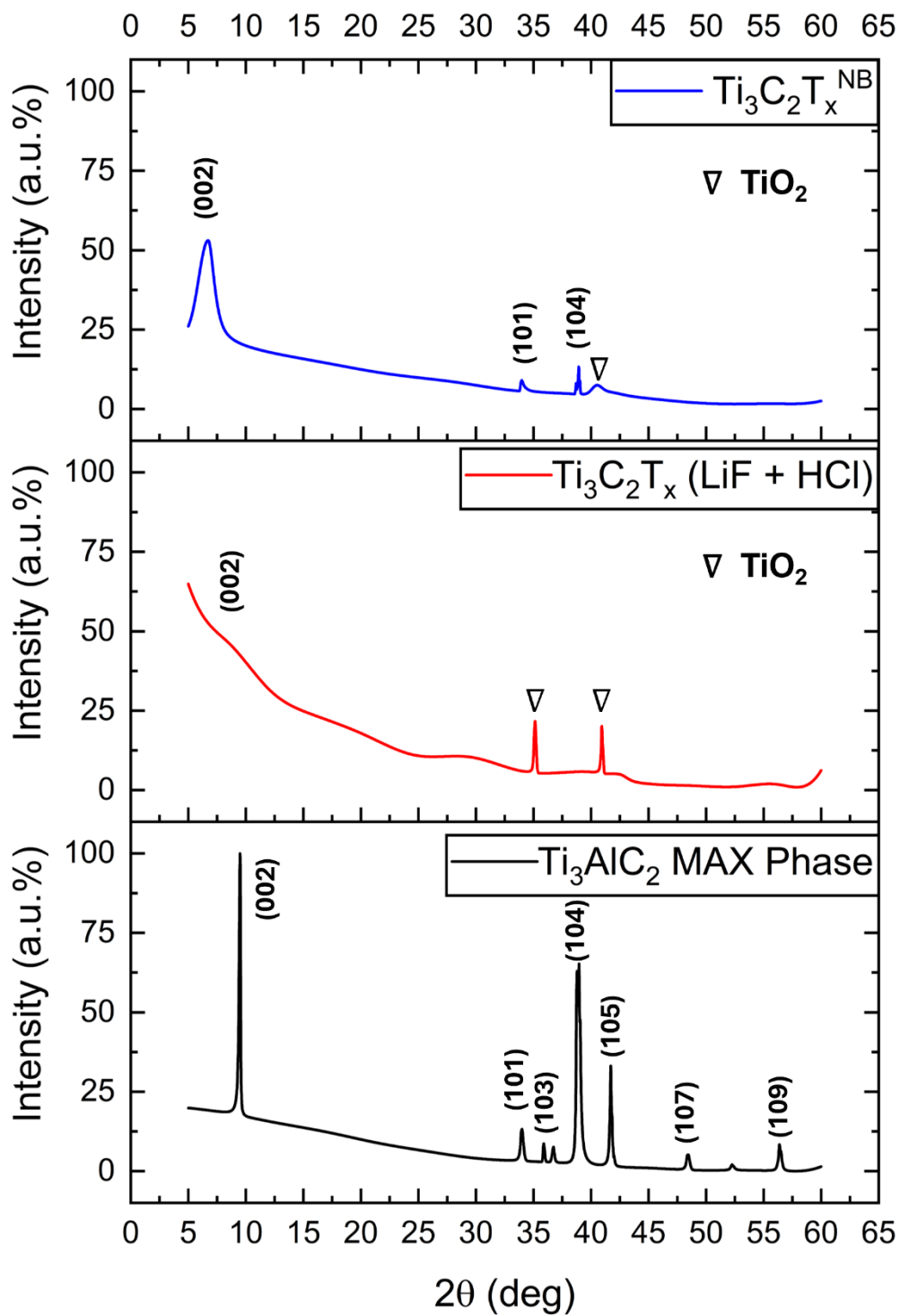


Figure 3.10 - XRD diffraction patterns of a) top - $\text{Ti}_3\text{C}_2\text{T}_x^{\text{NB}}$, b) middle - $\text{Ti}_3\text{C}_2\text{T}_x$ (LiF + HCl), c) bottom - Ti_3AlC_2 MAX Phase

3.3.3 Fluorine-Free Synthesis of $\text{Ti}_3\text{C}_2\text{T}_{0,\text{OH}}$

A commercial Ti_3AlC_2 MAX phase was selectively etched to $\text{Ti}_3\text{C}_2\text{T}_{0,\text{OH}}$ under highly alkaline conditions. The fluorine-free synthesis method, reported by Li et al, was modified with the aim of evaluating the effects of soaking time on the resulting MXene. Due to the species present in the etching solution, MXene terminations are predicted to be exclusively -O and -OH; therefore MXenes will be denoted $\text{Ti}_3\text{C}_2\text{T}_{0,\text{OH}}$. All MXenes synthesised via this method were characterised via XRD to gain insight into the structure of the etched $\text{Ti}_3\text{C}_2\text{T}_{0,\text{OH}}$.

Due to the extreme conditions of the synthesis, it was particularly challenging to find a suitable reaction vessel. The temperature of the reaction exceeds that of the maximum temperature recommendation of PTFE (250 °C), therefore an alternative liner material must be used. Simultaneously, due to the alkalinity of the etching solution, a stainless steel reaction vessel would be susceptible to high levels of corrosion, and therefore an acid/alkaline-resistant liner would be required. A polyphenylene polymer (PPL) liner was procured and used for the NaOH synthesis.

It is worth noting that to achieve high enough concentrations of NaOH (27.5 M), the reaction temperature must be significantly increased, which will significantly increase the internal pressure of the reaction vessel. As the reaction cannot be visually monitored at all times within the oven, it is not possible to ensure the complete pressurisation of the reaction, especially considering that once cooled, the internal pressure will return to 1 atm. All syntheses are assumed to have maintained pressure throughout the course of the reaction.

Firstly, Ti_3AlC_2 was etched under hydrothermal conditions (via 27.5 M NaOH, 270 °C) for 24 hours before being filtered, washed, and dried. The resulting diffraction pattern was evaluated alongside diffraction patterns for Ti_3AlC_2 and $\text{Ti}_3\text{C}_2\text{T}_x^{\text{(MILD)}}$ for comparison. A characteristic peak 7° , typically assigned to the (002) facet of a MXene/MAX phase, can be found at relatively high intensity when compared to other visible peaks. This (002) peak appears significantly broader than its corresponding peak in the MAX phase spectrum. In addition to the broadening of the peak, a 2° shift towards a lower diffraction angle is also seen – from 9° in the MAX phase, to 7° in the MXene. This shift can be accounted for by an increase in interlayer spacing. When

Al is removed from the MAX phase structure, the interlayer spacing between individual sheets is increased, especially in the case of large molecule intercalation.

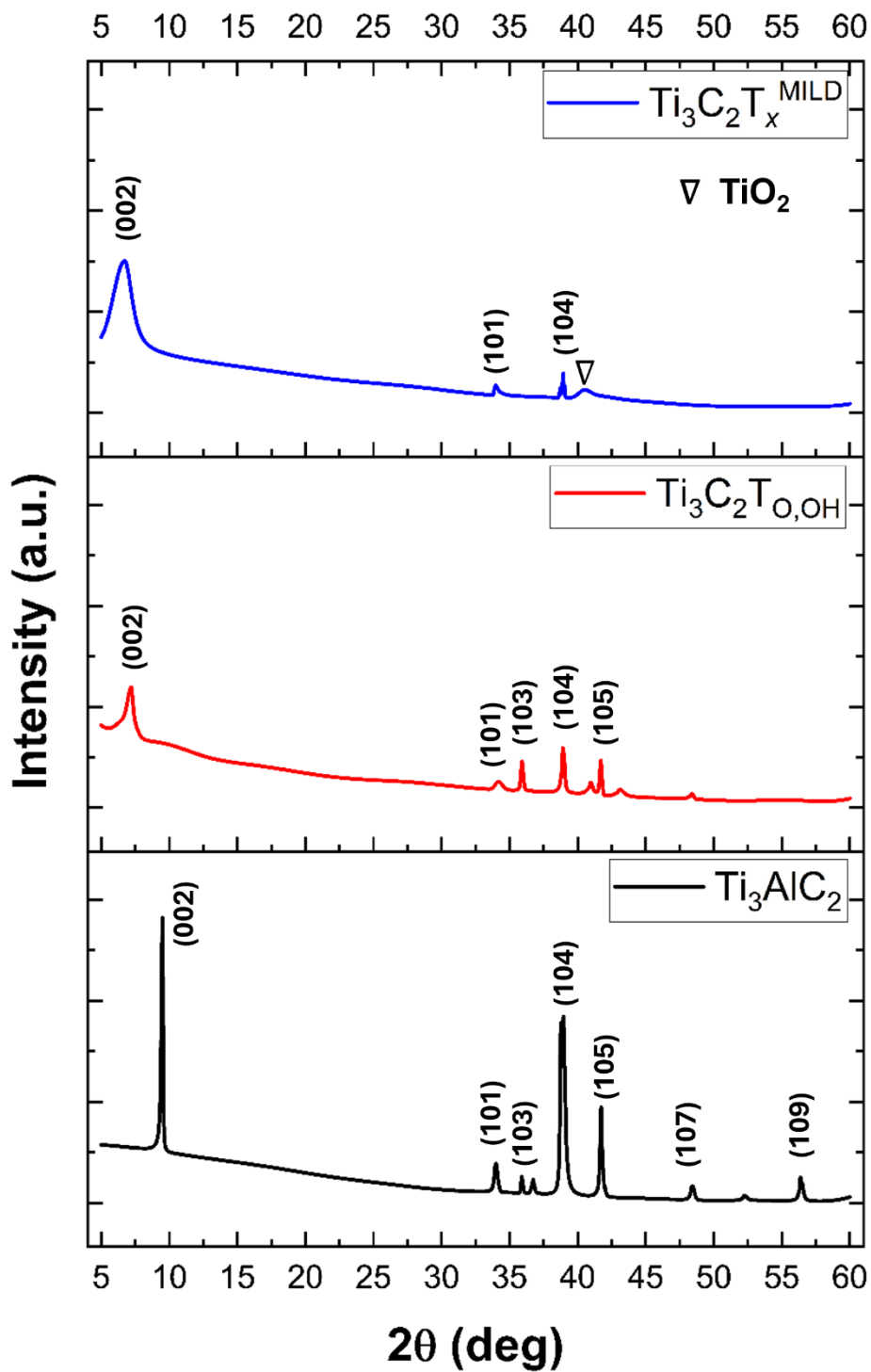


Figure 3.11- XRD diffraction patterns of a) top - $\text{Ti}_3\text{C}_2\text{T}_x^{\text{NB}}$, b) middle - $\text{Ti}_3\text{C}_2\text{T}_{\text{O,OH}}$ c) bottom - Ti_3AlC_2 MAX phase

An increase in interlayer spacing will lead to smaller diffraction angles, causing the peaks to shift to lower angles in the diffraction pattern. The broad (002) peak can be

seen in the MILD-etched MXene and therefore confirms the loss of Al in the MAX structure, indicating a successful MXene synthesis. Additional peaks can be seen in the diffraction pattern for $\text{Ti}_3\text{C}_2\text{T}_{0,0\text{H}}$ at 34° , 36° , 39° , and 42° ; which are also present in the MAX phase, correspond to (101), (103), (104), and (105) respectively. This indicates that there are still significant qualities of the unetched MAX phase in the alkali-etched sample; which is supported by the absence of peak shift – indicating no change in interlayer spacing. A peak of low intensity can be seen also at 9° , which is attributed to the (002) facet of the unetched MAX phase. This alkaline-etching of Ti_3AlC_2 has successfully produced $\text{Ti}_3\text{C}_2\text{T}_{0,0\text{H}}$ MXene in reasonable quantities; however, there are significant amounts of impurities that need to be eliminated should this sample be representative of a MXene. Owing to the difficulty of separating multi-layered MXene and MAX phase; the alkali-etched synthesis must be reattempted in order to reduce the amount of MAX phase impurity.

A second attempt at the alkaline synthesis was made with a modification to the post-etch drying procedure. Instead of being air-dried in a chemical oven; the sample in this case was placed in a vacuum oven overnight to avoid the presence of oxygen. As previously mentioned, MXenes have a high oxidation potential in the presence of moisture and heat – of which both are required for this synthesis. Alongside using de-oxygenated water in the etching solution, a vacuum oven was employed to eliminate oxygen in the drying environment but also decrease the drying time; thus minimising the opportunity for oxide formation. Although TiO_2 peaks were not present in the diffraction pattern of $\text{Ti}_3\text{C}_2\text{T}_{0,0\text{H}}$; defect sites may be present due to the harsh etching conditions, which will promote rapid MXene degradation.

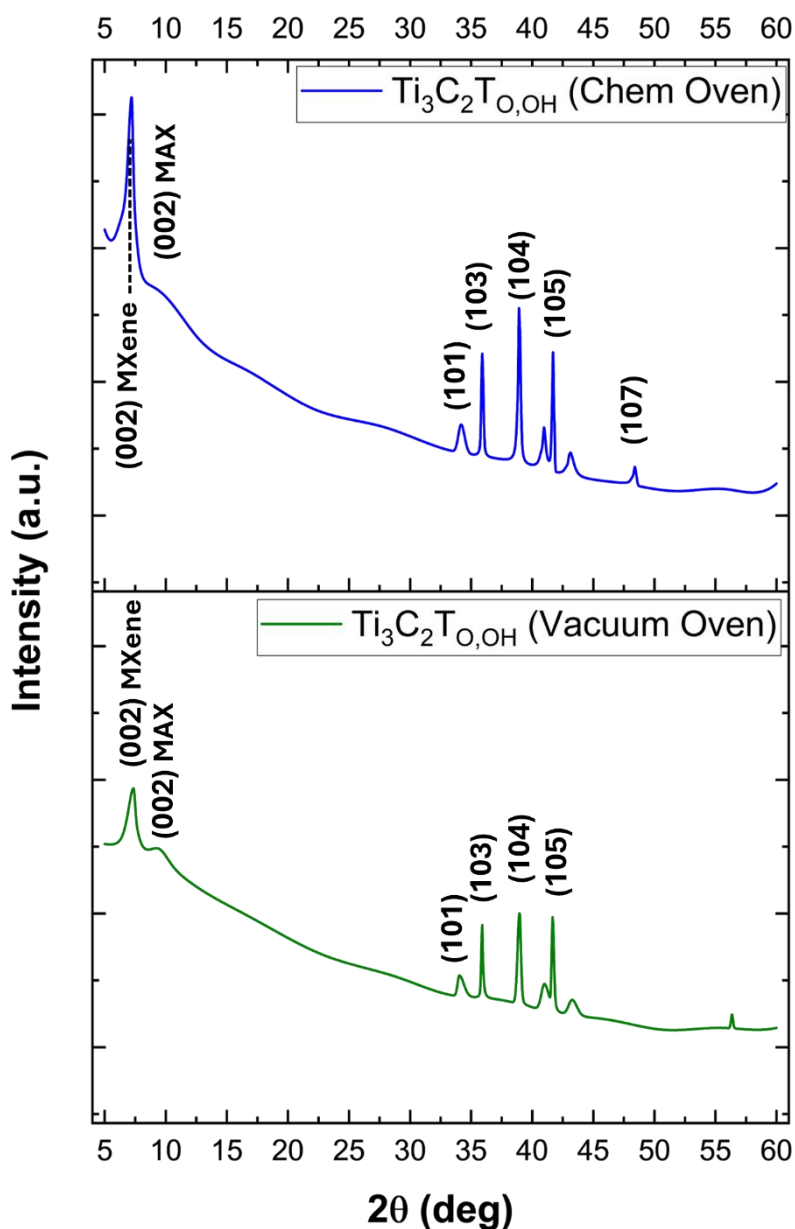


Figure 3.12 - XRD diffraction patterns of $\text{Ti}_3\text{C}_2\text{T}_{0,0\text{H}}$ dried in a) top - static air oven, b) bottom - vacuum oven

Following a reattempted synthesis; the diffraction pattern for the vacuum-dried $\text{Ti}_3\text{C}_2\text{T}_{0,0\text{H}}$ (Figure 3.12) shows a characteristic (002) MXene peak at 7° ; however, the intensity of the peak appears significantly less than previously observed. Additionally, the (002) facet peak, typically observed in a MAX phase, at 9° is much greater in intensity than the previous synthesis. MAX phase peaks at 34° , 36° , 39° , and 42° are again visible, corresponding to (101), (103), (104), and (105) respectively. Although the overall intensity of all peaks is considerably lower – their relative intensity when compared to the (002) MXene peak is much greater indicating substantially greater MAX phase impurities. As the etching conditions do

not vary between both the vacuum oven-dried and the chem oven dried samples, there must be unidentified factors influencing the quality of the MXene produced.

When Li et al reported the alkaline-etching of Ti_3AlC_2 to $Ti_3C_2T_{0,OH}$; both the concentration of NaOH in the etching solution and reaction temperature were evaluated, however, the reaction time was simply stated as 12 hours without sound reasoning. To this end, the effects of reaction time on the resulting MXene were studied for soaking times of 4, 8, 12, and 24 hours.

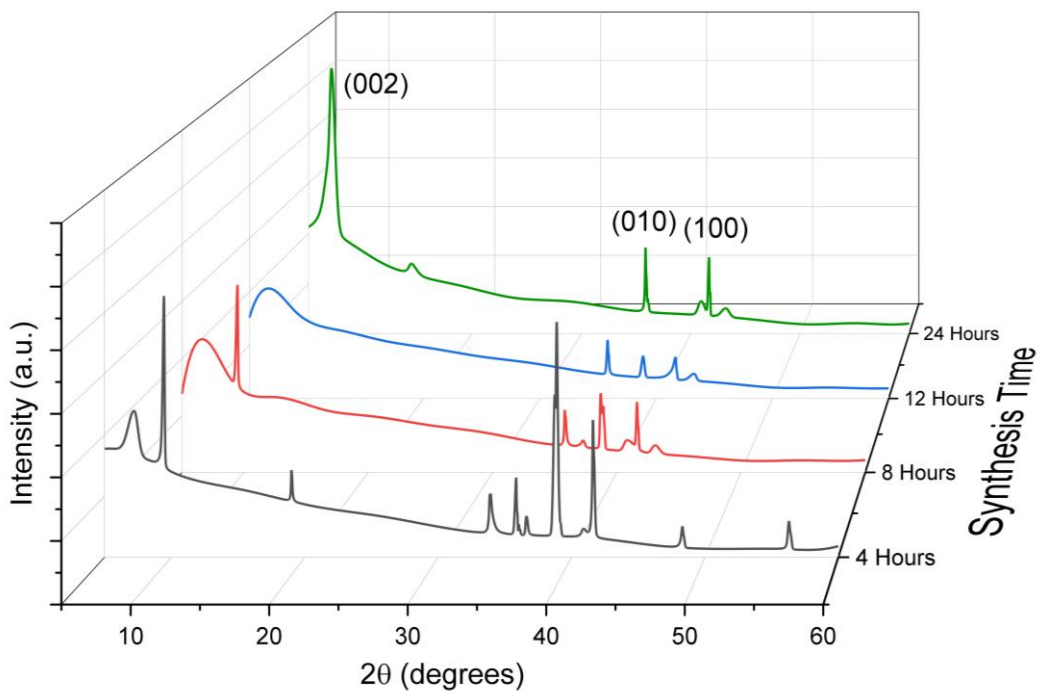


Figure 3.13 - XRD Diffraction patterns of $Ti_3C_2T_{0,OH}$ synthesised with a soaking time of a) black - 4 hours, b) red - 8 hours, c) blue - 12 hours, d) 24 hours

A 4-hour soaking time has shown, via XRD, to have little influence on the etching of Ti_3AlC_2 . All characteristic MAX phase peaks are present at high intensity; including those previously mentioned in the 30°-50° region and the (002) MAX phase peak at 9°. Interestingly, a small-broad peak at 7° is present after only 4 hours, indicating that the etching process begins prior to this time. As we increase the soaking time to 8 hours; the overall intensity of peaks in the 30°-50° region decreases alongside the MAX (002) peak at 7°. Peaks observed at 19°, 49° and 56°, corresponding to (104), (107), and (109) respectively, are no longer present after 8 hours. Interestingly, as the MAX phase (002) peak decreases in intensity, the broadness of the MXene (002) peak increases drastically, indicating a degree of disorder amongst the MXene

sheets. Typically, variations in the stacking arrangement of MXene sheets can lead to disorder in the crystal lattice; this will give a wide distribution of interlayer spacings and therefore result in a broader diffraction peak. It is thus far unconfirmed as to why we observe a broader MXene peak – however the delamination and subsequent re-stacking of MXene sheets during drying is a likely possibility.

When soaking time is increased to 12 hours; we observe a loss of the (002) MAX phase peak and a further decrease in intensity of the 30°-50° region. Although MAX phase peaks are still present in the diffraction pattern; their relative intensity compared to the broad (002) MXene peak suggests that the majority of the sample has been etched successfully to $Ti_3C_2T_{0,OH}$ with small amounts of MAX phase remaining. In an attempt to successfully etch the remaining MAX phase; the soaking time was increased to 24 hours.

The diffraction pattern for a 24 hour soaking time shows MAX phase peaks still present - specifically (010) and (100) facets giving sharp intense peaks when compared to the 12-hour synthesis. Contrastingly, the MXene (002) peak increased significantly in both intensity and sharpness – suggesting that not only is there significantly more MXene material present in the sample; but also there is a much less disorder in the crystal lattice.

Despite no evidence to suggest the depressurisation of the vessel, this must be considered when reporting these findings. Due to the bespoke nature of the synthetic set-up, namely the necessity of PPL, it would be significantly challenging to incorporate an internal pressure gauge within the set-up.

3.3.4 MXene Surface Functionalisation

3.3.4.1 Acid and Alkali Treatment of $Ti_3C_2T_x$

MXene - $Ti_3C_2T_x^{PM}$

Following the acidic and alkaline treatment of $Ti_3C_2T_x$ a deep orange supernatant was observed upon the MXene settling, shown in Figure 3.14. Despite several washes with deionised water and subsequent vacuum drying via a vacuum desiccator, the treated MXene displayed severe signs of oxidation, namely turning grey/white, within the following 48 hours. The orange supernatant observed is likely attributed

to the formation of a Ti(IV) compound, such as titanium(IV) oxide or titanium(IV) chloride, as they often yield yellow/orange solutions. The rapid oxidation of the material is likely due to the creation of defect sites on the surface of the MXene, attributed to the harsh chemical treatments. Acid and alkaline treatments can not only remove surface terminations but can also etch the subsequent active metal sites thus creating surface defects. The severity of these defects will be subject to certain factors such as pKa, concentration, and length of exposure. Typically, strong acids and bases, such as those used herein, are considered more likely to introduce defect sites on the surface of the MXene. An increased swelling time will also increase the risk of defect sites and thus greater oxidation potential.

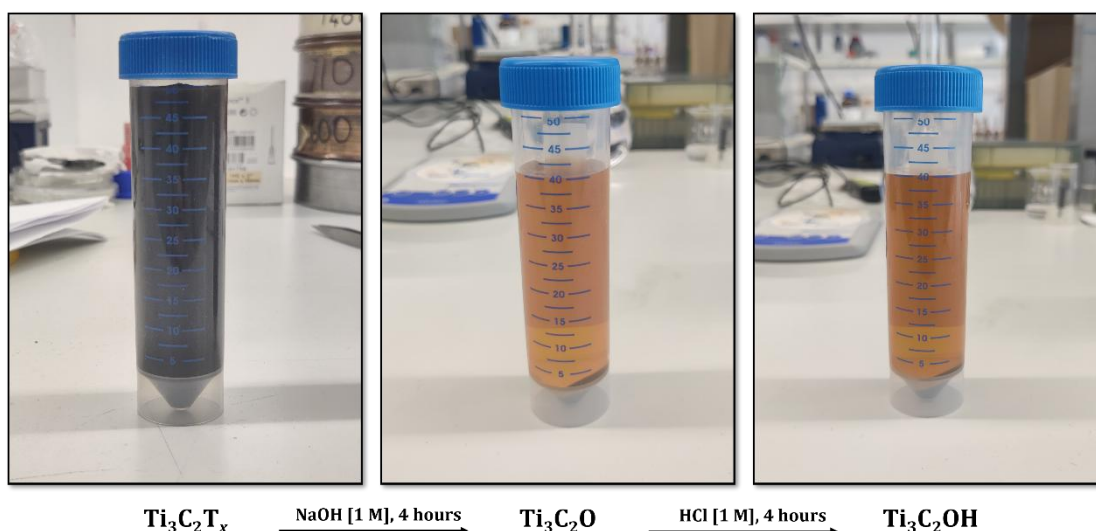


Figure 3.14 - Photographs depicting the alkaline and subsequent acidic treatment of $\text{Ti}_3\text{C}_2\text{T}_x$ to yield -O and -OH terminations respectively

To mitigate the generation of defect sites and resulting oxidation of the MXene, a lower concentration of strong acid/alkaline can be used. While in theory, this should reduce the defect sites present, it may also directly lower the removal of surface terminations. Alternatively, a lower soaking time may reduce the number of defect sites but may also prove ineffective for removing termination groups.

Due to the amount of material lost during each washing and drying step and the cost of MXene material at the time of this study – the thorough evaluation of surface functionalisation via acid and alkaline treatment was deemed too costly.

Since the time of this initial study, the cost of $Ti_3C_2T_x$ MXene has reduced significantly, and therefore the evaluation of alternative alkali/acid treatment for MXene functionalisation is worth further exploration.

3.3.4.2 – Ozone Treatments for -O and -OH Functionalisation

MXene – Commercial $Ti_3C_2T_x$

When considering the high oxidising power of ozone combined with the oxidation potential of MXenes in aqueous media, the opportunity to ozone-treat MXenes in a dry application is highly desired. For these reasons, a UV ozone cleaner was used to ozone-modify a drop-cast MXene film with the aim of achieving -O and -OH terminations exclusively.

While the dry ozone treatment of a MXene is one possible method for -O and -OH functionalisation, this process can be time-consuming and requires the individual treatment of each drop-cast film as they are prepared. The ability to ozone-treat MXenes in bulk would allow researchers to achieve a more consistent, cost-effective, and efficient process. To this end, the wet ozone treatment of MXenes may be an attractive alternative.

Alternative ozone treatment methods are evaluated herein for the -O and -OH functionalisation of $Ti_3C_2T_x$ MXene.

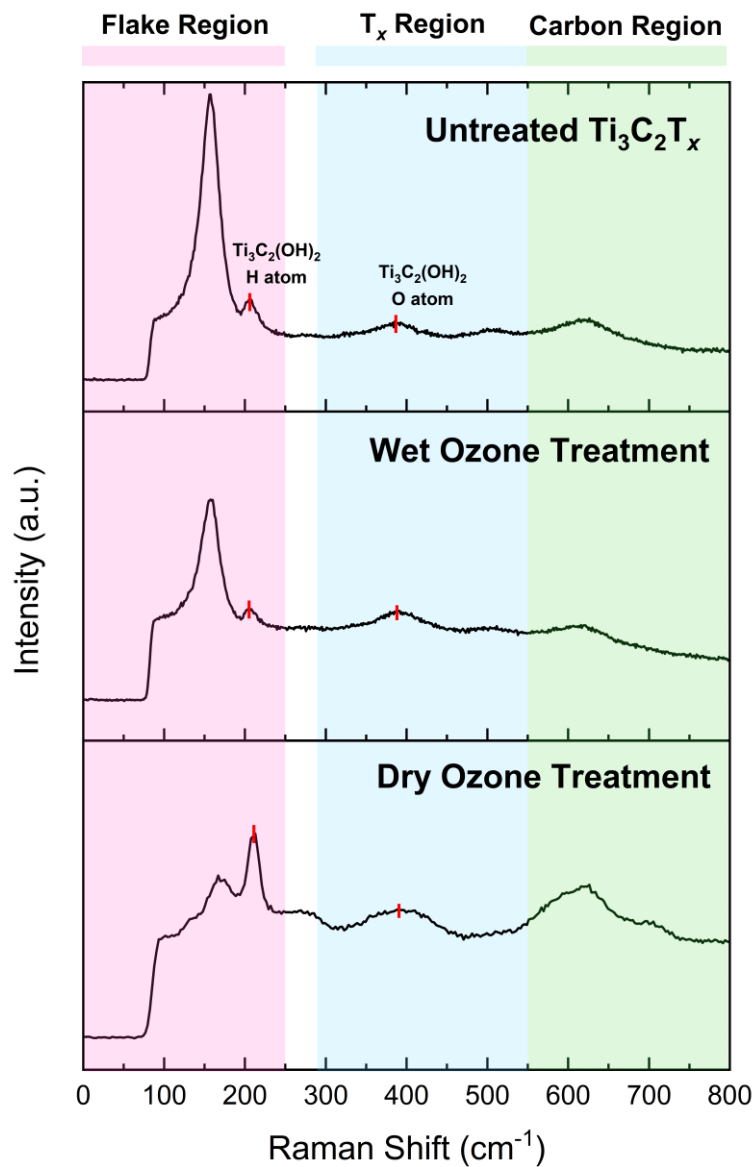


Figure 3.15- Raman Spectroscopy patterns for a) Untreated $Ti_3C_2T_x$ b) wet ozone treated Ti_3C_2 c) dry ozone treated Ti_3C_2

The ozone treated MXene materials were subject to SEM/EDX-coupled Raman spectroscopy for surface morphology and compositional evaluation. The obtained Raman patterns for untreated, wet ozone functionalised, and dry ozone functionalised Ti_3C_2 are overlaid in Figure 3.15. Each known region of the Raman spectra has been identified as the flake region (0-250 cm^{-1} , pink), termination group region [T_x] (290-550 cm^{-1} , blue), and carbon region (550-800 cm^{-1} , green). The Raman spectra obtained for the untreated MXene sample align well with those reported in the literature, with characteristic peaks matching in the flake, T_x , and carbon regions. Notably, peaks at 210 cm^{-1} and 390 cm^{-1} have been reportedly

attributed to the -H and -O atoms of the -OH termination groups respectively and have been identified in red in the presented spectra.

When evaluating the effects of a wet ozone treatment, both the untreated and treated spectra appear near-identical, with the peak-to-peak intensities remaining unchanged across the entire spectra. The characteristic flake region peak observed at 150 cm^{-1} is used as a reference to monitor changes in the characteristic -OH peaks. No significant changes in the intensity of the -OH peaks at 210 cm^{-1} and 390 cm^{-1} are observed, suggesting the wet ozonation method to be ineffective in functionalising the MXene surface with -OH terminations.

When comparing the untreated MXene to the dry ozone-treated MXene, significant differences can be seen in both peak intensities and position. Interestingly, the characteristic flake-region peak at 150 cm^{-1} appears significantly less intense following ozone treatment. This variation in peak intensity has yet to be rationalised, with further structural analysis necessary to fully understand the observed phenomenon. While a small peak can still be observed at 150 cm^{-1} , the neighbouring peak at 210 cm^{-1} , attributed to the -H atom in the -OH termination, appears drastically more intense relative to its neighbouring peak. The next peak in the spectra at 390 cm^{-1} , attributed to the -O atom in the -OH termination, appears much broader than previously seen in the untreated material. Despite appearing to have a higher absolute intensity, when compared to the carbon-region peak at 620 cm^{-1} it is unclear as to whether it is a true increase in relative intensity or simply a more sensitive sample location. Notably, the absence of characteristic rutile and anatase peaks typically observed at 450 cm^{-1} and 510 cm^{-1} respectively indicate the suppression of TiO_2 formation during the ozonation procedure. While the oxidation of MXenes at defect sites is commonplace following aqueous applications, strict measures, such as the degassing of delamination solutions and the meticulous drying of the drop-cast film, have proved effective in avoiding TiO_2 formation. While the Raman spectra presented herein show indications for the effective dry ozone treatment of $\text{Ti}_3\text{C}_2\text{T}_x$, inscrutable phenomena observed in the spectra suggest the need for further comprehensive surface chemistry analysis.

X-ray photoelectron spectroscopy surface analysis was employed (Figure 3.16) to probe the surface populations of $\text{Ti}_3\text{C}_2\text{T}_x$ and dry ozone-treated Ti_3C_2 to identify any

changes in the composition of surface species. When evaluating the high-resolution F 1s spectra, a significant decrease in C-Ti-F (684-685 eV) peak intensity can be observed following ozone treatment, indicating the partial removal of -F terminations from the MXene surface. An additional peak, attributed to Al-F, also sees a decrease in intensity following ozone treatment. The Al-F present in the sample prior to treatment is likely attributed to residual aluminium fluoride from the etching process. As the dry ozone treatment involves the drop-casting of MXenes onto a substrate prior to ozonation, the aluminium fluoride in the sample is likely removed/reduced during the aqueous delamination process.

The Cl 2p spectra display two primary peaks, attributed to an electron's two possible spin states in the 2p shell within the Ti-Cl bond, $2p_{3/2}$ and $2p_{1/2}$. These peak intensities can be considered as a single feature as the ratio of their intensities is generally constant for a given chemical environment. Following ozonation, the Ti-Cl peaks see a drastic reduction in intensity, larger than that observed for the C-Ti-F bonding in the F 1s spectra. This reduction in peak intensity indicates the partial removal of -Cl terminations from the surface of the MXene. As the peak intensity for XPS typically correlates with surface populations, this reduction loosely translates to a 10-15% reduction in -Cl termination following ozone treatment. A third peak highlighted in orange is also present in the -Cl spectra at around 202 eV, which may potentially be attributed to chlorine compounds of a different oxidation state. The source of this additional chlorine compound is unknown, however, even air has the potential to react with the bound chlorine, forming higher oxidation state chlorine species following exposure. Despite the unknown nature of this chlorine compound, a reduction in peak intensity of similar magnitude is observed for it resulting in a very weak signal. Further spectroscopic analysis of the MXene surface may provide crucial information regarding the identity of the orange peak.

Finally, O 1s spectra provide information regarding firstly, the population of oxygen species, via the Ti-O bond peak at 530 eV, and secondly the population of -OH surface termination groups via the Ti-OH bond peak at 523 eV. Following ozonation, the Ti-O bond peak sees a dramatic increase in intensity of over 20%,

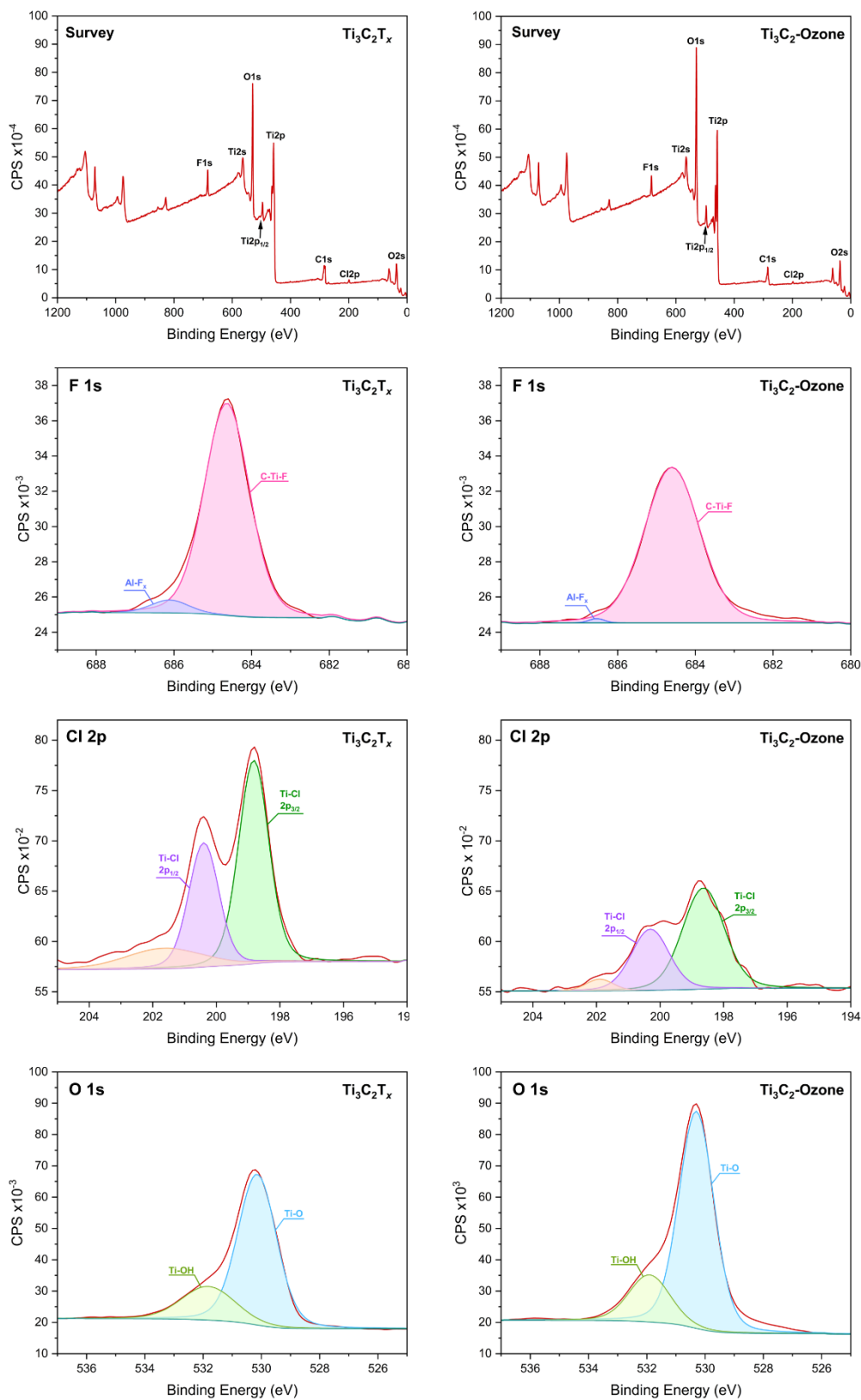


Figure 3.16 - High resolution (a) survey, (b) F 1s, (c) Cl 2p, (d) O 1s XPS spectra of (1) $Ti_3C_2T_x$, (2) dry ozone-treated Ti_3C_2

loosely translating to an oxygen population increase of the same percentage. As previously confirmed by Raman spectroscopic analysis, the formation of TiO_2 is suppressed during ozonolysis, and therefore the Ti-O bonding observed in XPS analysis directly correlates to the population of oxygen termination groups. Additionally, the Ti-OH bond peak sees an increase in intensity by over 10% following the ozone treatment of the sample, a value which equates to the same percentage change in the population of -OH terminations.

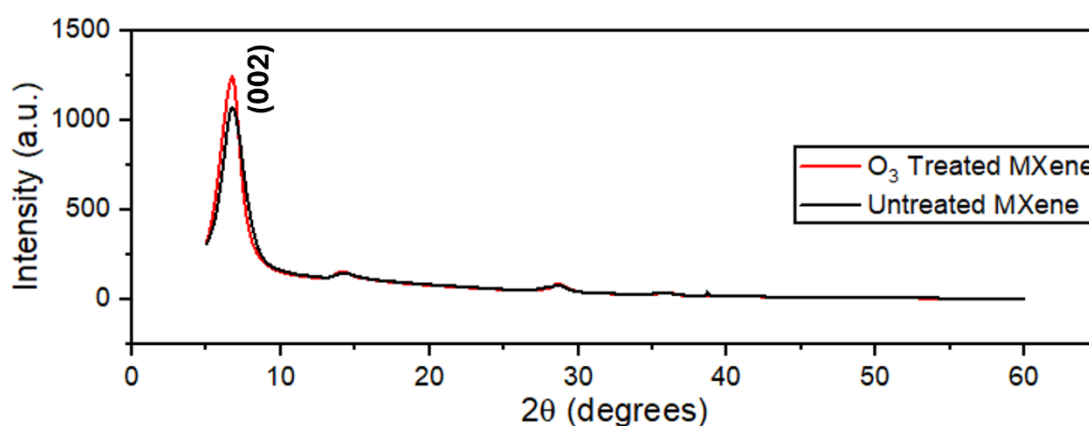


Figure 3.17 - X-ray diffraction patterns for a) black - $\text{Ti}_3\text{C}_2\text{T}_x$ MXene b) red - Ti_3C_2 -Ozone

Finally, x-ray diffraction patterns were obtained for the ozone-modified Ti_3C_2 -Ozone and the $\text{Ti}_3\text{C}_2\text{T}_x$ MXene to evaluate the levels of oxidation present as a result of ozone modification. The resulting XRD diffraction patterns are near identical, with no additional peaks attributed to the formation of TiO_2 following ozone treatment.

The dry ozone modification proved highly effective in modifying the surface chemistry of $\text{Ti}_3\text{C}_2\text{T}_x$, successfully replacing -F and -Cl terminations with desired -O and -OH termination groups, without any significant evidence of TiO_2 formation. Further optimisation of ozonolysis parameters could see greater levels of desired -O and -OH functional groups terminating MXene sheets.

3.4 Conclusions

Firstly, the direct comparison of MAX phase synthetic methods was conducted between the Barsoum and Maughan methods, each utilising different precursor powder mixtures. Firstly, we note the observation of partial MAX phase formation

following the Maughan method at 1200 °C, with no evidence of MAX phase formation using the Barsoum method at the same temperature. We next emphasise the effects of calcination temperature on the resulting MAX phase, with a temperature of 1350 °C necessary to achieve significant Ti_3AlC_2 formation via the Maughan method, which aligns with current literature. This is 150 °C lower than that reportedly necessary for the Barsoum method. Finally, despite low amounts of impurity observed in the resulting Ti_3AlC_2 MAX phase, the sample was deemed unsuitable for MXene synthesis. Further optimisation of experimental parameters and post-synthetic handling may yield a MAX Phase of sufficient purity for MXene synthesis.

The etching of Ti_3AlC_2 to $\text{Ti}_3\text{C}_2\text{T}_x$ was attempted via the *in-situ* generation of HF. Following repeated attempts, the successful synthesis of $\text{Ti}_3\text{C}_2\text{T}_x$ was achieved, with the resulting SEM and XRD analysis confirming the removal of the A layer from the MAX phase structure. Despite the successful synthesis, impurities were observed in both characterisation methods, likely attributed to the formation of TiO_2 during etching. These impurities are considered too significant and may interfere with the resulting electrochemistry. In efforts to avoid the harsh etching conditions of HF, alternative etching solutions were explored.

With the aim of both removing the HF etchant and simultaneously terminating synthesised MXenes with -O and -OH functional groups, the alkaline etching of Ti_3AlC_2 to $\text{Ti}_3\text{C}_2\text{T}_{\text{O,OH}}$ was attempted. Initial syntheses proved ineffective, with significant amounts of Al remaining in the sample. We next evaluated the effects of soaking time on the resulting MXenes, concluding that a 24-hour soaking time produced higher purity MXenes with less disorder than an MXene utilising a 12-hour soaking time. MAX phase peaks were still present in the sample, potentially due to the depressurisation of the reaction vessel. To ensure a complete etching, a specialised set-up is necessary to accommodate both the high pressure and extreme alkalinity of the NaOH synthesis. As mentioned previously, the recent drastic decrease in MXene cost suggests that the functionalisation of commercial samples is more cost- and time-effective for the -OH and -O functionalisation of high-purity MXenes.

Finally, the -O and -OH functionalisation of a commercial $\text{Ti}_3\text{C}_2\text{T}_x$ was attempted via various chemical treatments. Firstly, the submersion of $\text{Ti}_3\text{C}_2\text{T}_x$ in alkaline and acidic

baths proved ineffective at functionalizing the MXene, and instead appeared to oxidise the material yielding an orange supernatant. An alternative chemical treatment, namely ozone functionalisation, was attempted via two methods. The wet ozonation method proved ineffective in replacing -F and -Cl terminations with -O and -OH, however, the resulting MXene remained structurally unchanged. The dry ozonation method was then successfully employed, resulting in the reduction of -F and -Cl terminations which were replaced by -O and -OH as confirmed by Raman spectroscopy and XPS analysis. It was also confirmed that the increase in oxygen content was not attributed to the formation of TiO_2 , thus suggesting a successful, defect-free, -O and -OH modified T_3C_2 MXene.

4 MXene Delamination and Electrode Modification

4.1 Introduction

Catalyst inks are crucial components in the fabrication of catalyst layers and films for electrochemical applications. They involve the dispersion of catalyst particles in an appropriate solvent, typically in the presence of a binding agent to assist in the adhesion of the resulting film to a substrate. The choice of solvent will have a significant influence on the resulting ink, in particular the dispersion and potential agglomeration of catalyst particles, and the resulting homogeneity of the dried catalyst film. Several reports have emphasised the importance of appropriate solvent choice in the context of fuel cell catalyst layers, which rely heavily on the homogeneity of the fabricated layers.¹³⁴⁻¹³⁷

Owing to the hydrophilicity of MXene sheets, the dispersion of these materials as catalyst inks is widely utilised in the preparation of catalytic films and modified electrodes.¹³⁷⁻¹³⁹ Several studies have explored the dispersive capabilities of MXenes, with a particular focus on ink composition, processing methods, and oxidation stability.¹⁴⁰⁻¹⁴³ In order to achieve a stable MXene dispersion in a liquid media, they must be fully delaminated, a process in which the Van der Waals forces holding together MXene sheets are overcome to yield single or few-layered MXene sheets. This delamination process is typically achieved directly following synthesis, however, the delamination of ML-MXenes from a dry powder is of significant importance to low-cost, low-hazard MXene utilisation.¹⁴⁴

4.1.1 Delamination and Intercalation

Mechanical delamination is the most widely used technique to effectively delaminate and disperse MXenes in liquid media. Several reports have detailed the effectiveness of repeated manual shaking and centrifugation to yield large defect-free MXene flakes.^{145,146} Sonication, however, provides several key advantages over manual shaking. Firstly, reports have suggested sonication significantly improves dispersion stability, with Seyedin et al. claiming that sonication is necessary to redisperse a dry MXene powder back into a stable dispersion.¹⁴⁷ Secondly, sonication can provide precise control over a MXene flake size, with Maleski et al. reporting the production of smaller, more uniform MXene flakes via sonication, ultimately enhancing the electrochemical properties of MXenes.¹⁴⁸ Despite the effectiveness of this methodology, it must be utilised with care, as the incorrect handling and processing of MXene dispersions may lead to degradation of the resulting flakes. Due to the high-power output of sonication, the high-frequency sound waves can generate significant amounts of heat, which will ultimately lead to the formation of TiO₂ at surface defect sites and edge planes on the MXene, thus degrading the material. Additionally, a prolonged targeted sonication has the potential to fragment MXene flakes, again revealing exposed edge planes with an opportunity to oxidise. This over-delamination can result in a loss in conductivity of the flakes, reduce mechanical strength, and significantly reduce the number of catalytic active sites.¹⁴⁹

An alternative method of delamination is via the intercalation of ions or molecules between MXene sheets. Once diffused between the MXene layers, repulsive forces overcome the inter-sheet VDW forces, thus forcing them to separate. The presence of intercalants and increased inter-layer spacing also prevents the re-stacking of FL- and single-flake MXenes, thus providing a stable dispersion.¹⁵⁰ One of the most widely reported intercalants for delamination is Li⁺ ions, which are typically found in the etching solution of MXenes.¹⁵¹⁻¹⁵³ This is particularly beneficial at the point of synthesis as dispersions can be produced during synthesis without any further processing. The redispersion of dry MXene powders, however, is notoriously challenging and requires further investigation. In addition to etching solution species, the delamination of MXenes has been reported using a host of alternative

intercalants with DMSO being the most commonly used. Early MXene work, published by Naguib et.al., detailed the combination of sonication with DMSO intercalation to produce stable MXene colloidal solutions, a method which has become common practice in recent years.¹⁵⁴

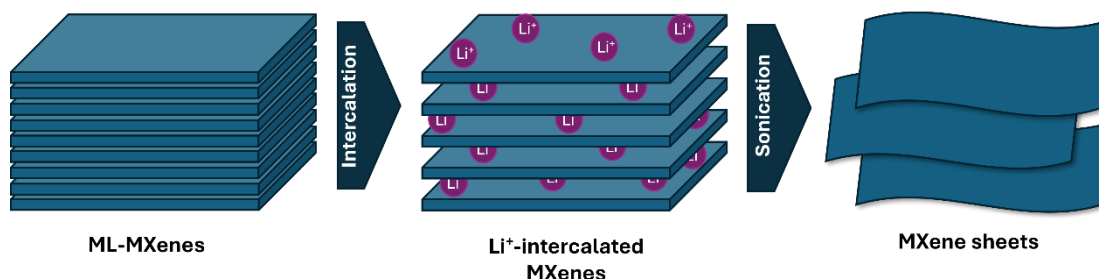


Figure 4.1- Schematic showing Li⁺ ion intercalation between ML-MXenes

Despite the effectiveness of coupling DMSO intercalation with sonication, challenges arise following the preparation of MXene films from the colloidal dispersion. Specifically, due to the high boiling point of DMSO, significant amounts of heat are required to evaporate the DMSO yielding a dry film, which has the potential to oxidise the MXene. This combined method holds significant advantages, but the use of which will ultimately depend on the intended application.

4.1.2 Electrode Fabrication

For electrochemical applications, following delamination, MXenes must be deposited onto an electrode substrate or formed into a free-standing film. Traditional deposition methods have been widely reported for catalyst-modified electrodes including drop casting, spin coating, and dip-coating. To determine the optimal electrode modification method for MXenes, one must consider their inherent properties and the intrinsic costs associated.

Dip-coating is the process of immersing a substrate in a liquid before being withdrawn to form a coating. It typically requires high-viscosity liquids as they tend to adhere more strongly to substrates while also minimising the excess runoff.¹⁵⁵ With water being a common solvent choice for MXene ink, this method is not appropriate and would present significant challenges in controlling the resulting catalyst film.

For enhanced film thickness control and uniformity, spin-coating is commonly used in thin film fabrication for a variety of electrochemical applications. This technique utilises centrifugal force to distribute material uniformly across a surface, however, a significant majority of MXene ink is typically wasted during the spin-coating process and is therefore unsuitable for the low-cost fabrication of MXene films.¹⁵⁶

Finally, drop casting is by far the most widely used method for electrode modification due to its simplicity and accessibility. (Brook et al., 2014; Kaliyaraj Selva Kumar & Compton, 2022; Z. Wang et al., 2010) To begin, a controlled droplet of catalyst suspension is deposited onto a substrate, typically an electrode such as glassy carbon, before the solvent is evaporated leaving behind a dried catalyst film. The choice of drop casting solvent is particularly important as it has been reported to directly influence the homogeneity of the resulting catalyst film. A recent review paper was published by Kumar et al. of the Compton group, evaluating the reliability of drop casting with a particular focus on the coffee ring effect.¹⁶⁰ Following the evaporation of typical drop casting solvents under standard conditions, a ring-like pattern is often visible towards the outer diameter of the electrode film. In short, this ring effect is attributed to the capillary flow of the solvent from the centre towards the edge, as evaporation occurs at a higher rate towards the edge due to greater ventilation. With this capillary flow, catalyst material suspended in the solvent follows the flow, thus migrating towards the edge and depositing once dry.

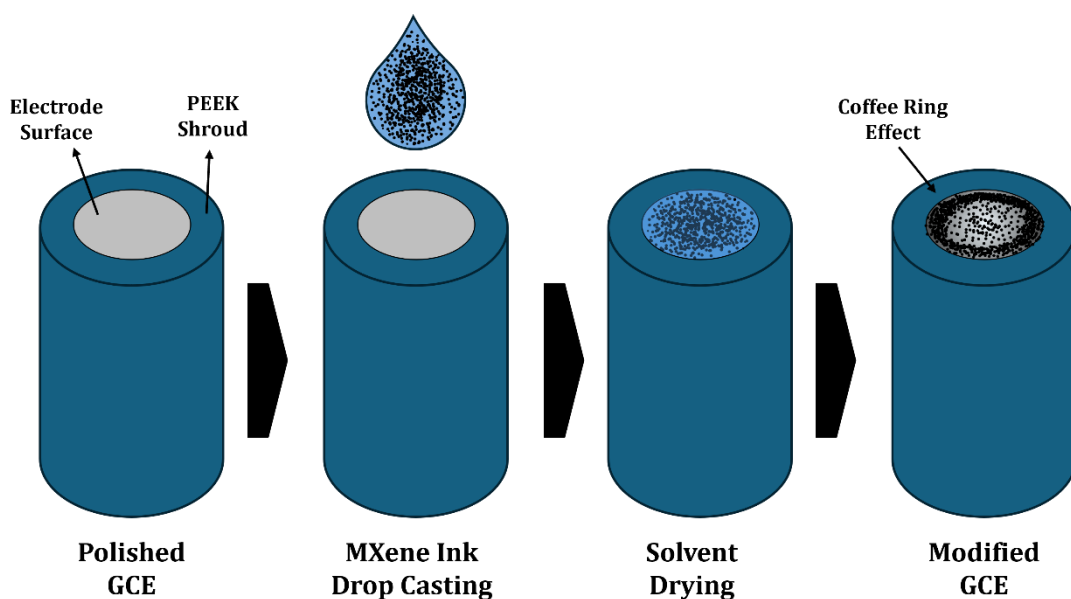


Figure 4.2 – Schematic showing the drop casting of catalyst particles on an electrode culminating in the coffee ring effect

While there are certain influencing factors that can be optimised, such as drop casting solvent, evaporation method, and temperature, careful considerations must be made to preserve the catalyst material ensuring it remains chemically unchanged. In the case of MXenes, these parameters must be optimised to ensure a successful and stable delamination with a preserved MXene structure following deposition.

Owing to the bespoke properties of MXene sheets, there have been several reports of free-standing MXene films (FSMF) which utilise inter-sheet VDW forces to bind MXene sheets together.¹⁶¹⁻¹⁶³ Free-standing films are typically synthesised via the delamination of MXenes followed by the subsequent drying via vacuum-assisted filtration. Upon filtering and drying, the single/FI-MXene sheets are restacked with the inter-sheet VDW forces reportedly strong enough to produce a free-standing, binderless film. Free-standing films are exclusively manufactured directly following the synthesis of a MXene, with no current literature reporting the fabrication of a free-standing MXene-only film from a commercial sample.¹⁶¹ While typically FSMFs are reported for dry applications, such as solid-state battery anodes and cathodes, their inclusion in aqueous electrochemistry has been reported recently, highlighting their stability in a variety of aqueous electrolytes.¹⁶⁴ The synthesis of a free-standing MXene film with high stability in aqueous conditions from commercial MXene samples is highly attractive towards accessible MXene CO₂RR catalysis.

4.1.3 Electropolymerisation of EDOT

Electrochemical polymerisation, also known as electropolymerisation (EPOL), is a well-established technique that refers to the process of depositing layers of polymer onto an electrode surface using electrical potential. This highly tuneable technique allows precise control over the thickness, morphology, and chemical composition of the polymerised films in an array of aqueous and non-aqueous electrolytes.¹⁶⁵

There is a vast library of conductive monomers that can be used for the purposes of electropolymerisation, often categorised into anodic or cathodic monomers. During electropolymerisation, anodic monomers undergo oxidation at the anode leading to the formation of a radical cationic species. These species then react with one another on the surface of the anode via polymerisation, thus forming a thin film of conductive

polymer on the electrode surface. Popular anodic monomers include pyrrole, thiophene, aniline, and 3,4-ethylenedioxythiophene (EDOT), which have been reported in various applications including conductive coatings, sensors, supercapacitors, flexible electronics, and energy storage devices.¹⁶⁶⁻¹⁶⁹

3,4-ethylenedioxythiophene (EDOT) is one of the most frequently used monomers for electropolymerisation since it is stable in most aqueous and non-aqueous electrolytes and readily polymerises under electrochemical conditions.¹⁷⁰ The resulting polymer, poly(3,4-ethylenedioxythiophene) (PEDOT), exhibits high electrical conductivity in addition to being oxidation, chemical, and moisture resistant.

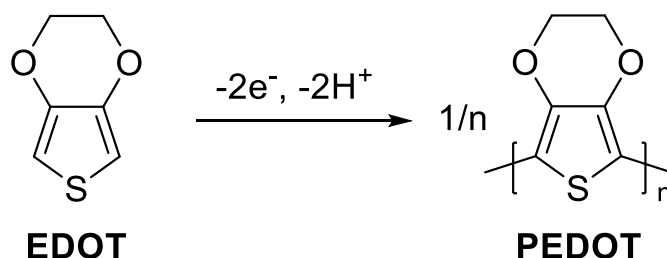


Figure 4.3 – Reaction scheme of the electropolymerisation of EDOT to PEDOT

In addition to the choice of monomer, the selection of electropolymerisation solvent is crucial as this will have a direct impact on the resulting film's properties. A recent study by Seki et al detailed the effects of different electrolytes and film thicknesses on the intrinsic properties of EPOL PEDOT films.¹⁷¹

Electropolymerisation offers the ability to immobilise a heterogeneous catalyst within a polymer matrix while having a great degree of control and precision over the properties of the resulting film.¹⁷² This approach is well documented in the literature.

Although drop-casting is typically used for the modification of an electrode surface with a catalyst in the presence of a binder, electropolymerisation offers a higher degree of control over the resulting catalytic film. There are 2 primary methodologies for catalyst immobilisation using electropolymerisation.

The first method, referred to herein as single-step EPOL (SSE), involves dispersing the catalyst in the polymer-containing electrolyte. When an electric potential is

applied to the electrode, the monomers are electrostatically attracted to the electrode's surface. As the monomers move towards the charged surface, they encapsulate catalytic material, effectively ferrying it towards the growing polymer matrix. This encapsulation process integrates the catalyst seamlessly into the newly formed polymer network. For SSE to be effective, a large amount of catalyst must be dispersed throughout the electrolyte, which notably won't all be incorporated into the film. Assuming all monomers present in the electrolyte are successfully polymerised on the electrode surface, gravimetric analysis can provide insight into the amount of catalyst successfully incorporated. This amount may vary in practice, which will significantly diminish reproducibility. The resulting polymeric film will contain homogeneously distributed catalyst, which can have significant benefits and applications.

The second method, referred to herein as dual-step EPOL (DSE), combines the technique of electropolymerisation with drop-casting. Firstly, a binder-free catalyst film is drop-cast on the surface of an electrode before undergoing electropolymerisation. During EPOL, monomers are electrostatically attracted to the electrode surface and consequently polymerise forming a thin film entirely covering the catalyst layer. This method presents distinct advantages. Firstly, it ensures the complete utilisation of catalyst material in the electrode modification, affording no unused catalyst – especially desirable for high-cost materials. Additionally, it allows for a precise quantification of catalyst on the modified electrode. Although the catalyst material is used to modify the surface of the electrode, it doesn't directly integrate into the film. This necessitates the selection of a polymer that is permeable to the chosen electrolyte and all possible reactants and products. Moreover, the second method will inherit all the disadvantages previously mentioned regarding the drop-casting of a catalyst ink.

While both methodologies present their own strengths and weaknesses, the decision will ultimately depend on the intended application of the resulting catalyst film.

As MXenes have excellent dispersion throughout aqueous media, the first method described herein would be suitable in practice; however, due to the inherent cost of MXenes, this methodology bears a significantly higher cost than the drop-cast

incorporated method. Table 4.1 shows the cost of each method with regards to MXene material only.

	<i>SSE</i>	<i>DSE</i>
Total Reaction Volume	5 mL	
MXene Cost (GBP)	£400 /g	
MXene Used	25 mg	0.125 mg
MXene Deposited	Variable	0.125 mg
MXene Cost per experiment	£ 10.00	£ 0.05

Table 4.1- A table comparing the associated cost of SSE and DSE electropolymerisation experiments

While the incorporation of MXenes in electropolymerised PEDOT films has gained traction in fields such as bioelectronics and supercapacitors in recent years, its application for electrocatalytic electrode preparation is yet to be investigated.

4.2 Materials and Methods

For delamination experiments, firstly 40 mg of $Ti_3C_2T_x$ was added to nitrogen-sparged deionised water (4 mL) in a 5 mL container. For manual shaking experiments - the MXene ink was shaken by hand for 60 seconds prior to monitoring. For manual agitation experiments – the MXene ink was agitated for a specified amount of time via magnetic stirring at 500 rpm. For bath sonication experiments – the MXene ink was placed inside a custom-designed holder within a 35 kHz sonication bath to prevent the spillage of ink. The bath was powered on for a specified amount of time. For probe sonication experiments - Firstly 40 mg of $Ti_3C_2T_x$ was added to nitrogen-sparged deionised water (4 mL) in a 5 mL container. Next, a sonic probe tip was immersed in the dispersion before being subject to probe sonication. Probe sonication was carried out for a specified amount of time, pulsing on and off for 6 and 10 seconds respectively at a 20% frequency (4 kHz), situated in an ice bath.

For drop casting experiments, a MXene dispersion was made according to the parameters outlined in Chapter 4.3.2. A known volume of the MXene dispersion was then drop cast onto a polished glassy carbon electrode (\varnothing 3 mm) and left to dry under ambient conditions.

For the fabrication of a free-standing MXene film, firstly 80 mg of $\text{Ti}_3\text{C}_2\text{T}_x$ was added to nitrogen-sparged deionised water (40 mL). The MXene dispersion was then subject to probe sonication in an ice bath for 30 minutes, pulsing on/off for 6/10 seconds, 20% frequency (4 kHz). Following sonication, the opaque black suspension was vacuum filtered through Nylon filter paper (0.22 μm pore size) via a filter holder funnel. The resulting solid was then dried on the filter paper at 50 °C overnight.

For electropolymerisation experiments, firstly 40 mg of $\text{Ti}_3\text{C}_2\text{T}_x$ was added to nitrogen-sparged deionised water (4 mL) in a 5 mL container. The MXene dispersion was then subject to probe sonication in an ice bath for 30 minutes, pulsing on/off for 6/10 seconds, 20% frequency (4 kHz). 20 μL of the MXene dispersion was then drop cast onto a polished glassy carbon electrode and left to dry under ambient conditions. Following modification, the electrode was placed in a custom electrochemical, presented in Chapter 4.3.4. Next, an electropolymerisation solution was made by the addition of EDOT (0.01 M, 7 mg) and LiCF_3SO_3 (0.1 M, 75 mg) to 4 mL of N_2 -sparged acetonitrile. The electropolymerisation solution was then added to the cell via syringe before an Ag/Ag^+ reference electrode and Pt counter electrode were added to the system. Electropolymerisation was then performed on bare and modified glassy carbon electrodes at 1.52 V (vs Ag/Ag^+) for 480 seconds before being left to dry under ambient conditions. Once dry the modified electrode was washed with deionised water.

$\text{Ti}_3\text{C}_2\text{T}_x$ MXene was procured according to Chapter 2.4.

Dimethyl sulfoxide, acetonitrile, and EDOT were purchased from Sigma Aldrich (UK). Lithium triflate (LiCF_3SO_3), EtOH and PEDOT:PSS were procured from Fisher Scientific.

Glassy carbon electrodes (\varnothing 3 mm), Ag/Ag^+ reference electrodes and Pt wire electrodes were purchased from IJ Camrbia Scientific LTD.

Fisherbrand Nylon filter paper (0.22 μm pore size, \varnothing 47 mm) was purchased from Fisher Scientific.

All electrochemical measurements were made using an IviumStat (Ivium) potentiostat controlling IviumSoft software.

A Fisherbrand 505 Sonicator (500 W, 20 kHz) with Microtip Probe 6.3 mm (5-50 mL volume) was utilised for probe sonication. An Elmasonic P30SE bath Sonicator was utilised for bath sonication

4.3 Results and Discussion

4.3.1 Delamination of $Ti_3C_2T_x$ and Intercalation

MXene - $Ti_3C_2T_x^{NB}$

The manufacture of various $Ti_3C_2T_x$ MXene inks was first carried out with the aim of achieving a stable MXene colloidal suspension for use in electrode fabrication. To provide a point of reference to the opacity testing, a picture of the Lancaster University crest was used to assess whether the MXene ink had settled. A physical copy of the crest was placed behind the MXene ink container; once the entire crest was visible, the ink was considered settled.

[1a] Firstly, $Ti_3C_2T_x$ was added to DI water and manually shaken for 60 seconds to delaminate the material. The subsequent black suspension was then monitored over the course of the following 60 minutes. Surprisingly, the suspension appeared to predominantly settle during the first 10 minutes, with the solvent turning completely transparent after 15 minutes.

[1b] The manual agitation time was increased to 5, 10, 30, and 60 minutes following subsequent repeat experiments. Due to the unreproducible nature of person-induced shaking, the manual agitation was achieved via a stirrer bar at 500 rpm. The subsequent black suspensions all appeared to settle at a similar rate, taking between 15 – 20 minutes to settle completely. This suggests that although the MXenes appear to readily disperse initially, the manual agitation time has little influence on the level of delamination from 5 to 60 minutes.

[1c] Manual agitation time was then replaced by a bath ultrasound sonication. This type of sonicator utilises high-frequency sound waves to agitate liquids, thus creating cavitation bubbles that will collapse and provide a concentrated surge of kinetic energy. This kinetic energy can be used to overcome the inter-sheet VDW forces between ML-sheets. Initial testing using a bath sonicator involved the sonication of a $Ti_3C_2T_x/H_2O$ dispersion for 30 minutes. Upon completion, the

dispersion was notably warm to the touch. The dispersion was monitored for the following 1 hour, which settled at around 40 minutes. Interestingly, the black dispersion appeared to discolour over time, with a dark grey tint appearing over the 40 minutes. The sample was returned to after 24 hours, with a light-grey powder present at the bottom of the sample tube. Considering the excess heat generated by the bath sonicator in addition to the observed colour change, it can be assumed that the MXene began to oxidise during the sonication.¹⁷³ For all subsequent dispersions, the solvent was first sparged with N₂ to remove any dissolved oxygen which would aid oxide formation. Additionally, an ice bath was employed for all consequential sonicating procedures to ensure the MXene sample remained below room temperature for the duration of the experiment.

[2] In efforts to avoid the coffee-ring effect previously discussed, a 1:1 solvent mixture of EtOH:H₂O was evaluated for its influence on the dispersibility of Ti₃C₂T_x. The addition of EtOH to water lowers the surface tension and increases the vapour pressure of the solvent mixture, allowing for a more rapid evaporating of the solvent, thus minimising the observed coffee-ring effect. Initial testing of the EtOH/MXene solvent mixture revealed a propensity for the MXene to aggregate and fall to the bottom of the sample tube following manual shaking. The solvent mixture was then bath-sonicated for 30 minutes to disaggregate and redisperse the MXene sheets. Following sonication, the Ti₃C₂T_x began to precipitate almost immediately, with it completely settling after just 10 minutes. This is potentially due to ethanol having a lower dielectric constant compared to water, which may lead to a reduced electrostatic repulsion between MXene flakes, thus promoting aggregation and subsequent precipitation.¹⁷⁴ A secondary consideration was the potential oxidation of the MXene. Owing to the significantly increased solubility of oxygen in EtOH,¹⁷⁵ the introduction of dissolved oxygen into the dispersion may promote the rapid oxidation of Ti₃C₂T_x at defect sites. This, however, was considered unlikely due to the lack of discolouration of the MXene material, with it remaining black following sonication. As the addition of EtOH to the MXene dispersion significantly reduced the dispersibility, EtOH was disregarded as a co-solvent.

[3a] According to recent reports, MXene dispersions can remain stable for over 7 days with effective delamination.¹⁵⁴ To this end, DMSO was selected as a promising

intercalant for not only delaminating MXene sheets but also for preventing their restacking in solution. Firstly, DMSO (500 μL) was added to the aqueous MXene dispersion and was manually shaken for 60 seconds. The resulting dispersion was monitored for 1-hour post-delamination. The MXene sheets displayed no evidence of agglomeration and remained dispersed for up to 45 minutes following delamination. By direct comparison, we can confirm that the utilisation of DMSO as an intercalant yields higher levels of delamination than manual shaking alone. This study was extended to assess the manual agitation of $\text{Ti}_3\text{C}_2\text{T}_x$ with increased time in the presence of DMSO. The results are presented in Figure 4.4.

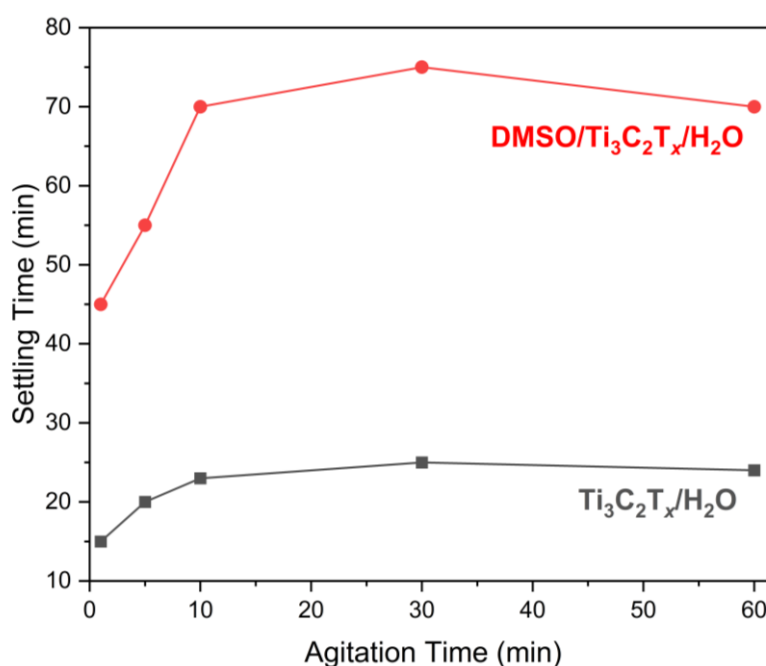


Figure 4.4 – Settling times of a) black - $\text{Ti}_3\text{C}_2\text{T}_x$ b) red- DMSO-intercalated $\text{Ti}_3\text{C}_2\text{T}_x$ inks as a function of agitation time

Following the introduction of DMSO into the MXene ink, a near 3-fold increase is observed in settling time which is consistent across all agitation times. The settling rate appears to remain near-constant from 30 minutes, suggesting this to be the optimal agitation time for manual shaking.

[3b] The combination of DMSO as an intercalant and the intense energy input of bath sonication was next evaluated. Following the sparging of the solvent mixture with N_2 and the implementation of an ice bath, the MXene dispersion was subject to bath sonication for 30 minutes. Upon completion, the MXene ink was left to settle at room temperature. As predicted, the MXene suspension remained stable for over 2

hours, with a determined settling time of 140 minutes. This is significantly longer than previous observations, suggesting that both mechanical and chemical methods are necessary to achieve high levels of delamination for $\text{Ti}_3\text{C}_2\text{T}_x$ MXene sheets. While DMSO has been shown to significantly benefit MXene delamination, complications may arise when attempting to form dry-stable catalytic films. As previously mentioned, due to the high boiling point of DMSO, the evaporation of the MXene solvent mixture may prove significantly challenging when attempting to form stable, dry films for catalysis. Alternative delamination methods must be considered for the applications of MXene thin-film fabrication.

[4a] Within a bath sonicator, the source of sound waves, in most cases, is a transducer beneath the bath. This means that for baths of varying volumes, the reproducibility of the sonication conditions can be challenging. Moreover, a considerable amount of energy can be lost as the sound waves travel further away from the source towards the top of the bath. Probe sonication provides a more targeted and powerful sonication method which is inherently more reproducible than bath sonication. A sonic probe is first immersed in a solution, with the tip positioned as central as possible. The probe tip then emits high-frequency sound waves which propagate through the liquid media transferring kinetic energy to the liquid at a much higher rate and intensity than bath sonication. To examine the targeted effects of probe sonication on MXene delamination, a $\text{Ti}_3\text{C}_2\text{T}_x$ dispersion was subjected to probe sonication for 5 minutes, pulsing on/off for 6/10 seconds to avoid rapid heat generation. The resulting ink was then monitored for the agglomeration and settling of MXene sheets. In the subsequent 3 hours following delamination, the deep black dispersion remained unchanged with no visible agglomeration or settling of MXene powder. The suspension was left overnight to settle. Approximately 28 hours after delamination the suspension had partially settled, with MXene powder visible at the bottom of the sample vial. Interestingly, the supernatant remained a tainted black/brown hue indicating the presence of few-layered/single-flake $\text{Ti}_3\text{C}_2\text{T}_x$ suspended in the solution.

[4b] For comparative purposes, the probe sonication was repeated for 30 minutes. The suspension remained stable for 30 hours, with small amounts of MXene powder precipitating to the bottom of the sample vial. After 48 hours, significant amounts of

MXene powder had precipitated, however, the supernatant was a similar black/brown hue to that previously observed following probe sonication. The

[4c] Finally, DMSO was added to the MXene ink prior to probe sonication. The resulting suspension remained stable for over 48 hours, with the black/brown supernatant indicating the presence of few-layer/single-flake MXenes for 72 hours after delamination. While the newly formulated MXene/DMSO ink cannot be used for the intended purposes mentioned herein, it conclusively demonstrates that to achieve the optimal delamination of $Ti_3C_2T_x$, both mechanical and chemical delamination methods must be used in tandem.

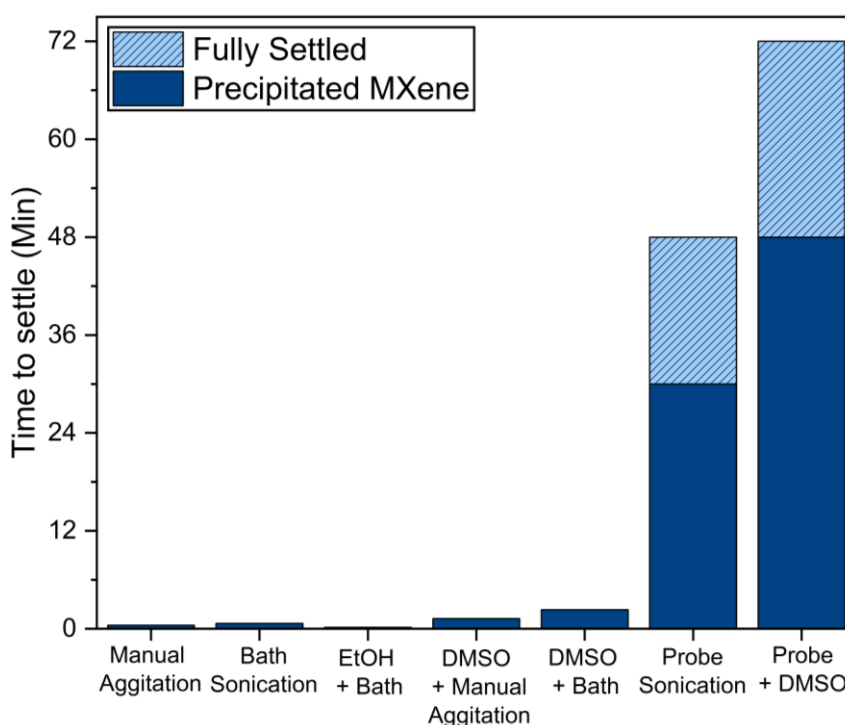


Figure 4.5 - Settling times of various $Ti_3C_2T_x$ inks as a function of the delamination method

Following the comprehensive testing of methods for the delamination of $Ti_3C_2T_x$, the probe sonication of a MXene/ H_2O dispersion was deemed optimal for the intended purposes and was taken forward for all subsequent ink studies.

4.3.2 Drop Casting

MXene - $Ti_3C_2T_x^{NB}$

The drop casting of MXenes was comprehensively studied to find the optimal conditions in which to form stable, homogenous MXene film electrodes. Due to its

popularity in the literature, Nafion was selected as a binder in the drop-casting procedure to ensure the resulting film had adequate adhesion to itself and to the electrode surface. A screening process was conducted for ink compositions whereby a modified electrode was submerged in KHCO_3 [0.1M] electrolyte within an electrochemical cell for 30 seconds. During this time, the film was observed for any deterioration or detachment from the electrode surface. Where stable, the electrochemical evaluation of each modified electrode was conducted to assess the stability and electrochemical behaviour of the film. Although it was not feasible to assess every possible combination of variables reported herein, the most promising options in each instance were selected and justified where necessary.

4.3.3 Binder Concentration

Firstly, the amounts of Nafion binder were varied to find the optimal loading for a 10 mg/mL MXene dispersion. Prior to delamination, calculated amounts of Nafion were added to the MXene/water mixture to ensure the complete mixing of the binder with the catalytic material. Once prepared, 20 μL of ink was drop cast onto a polished glassy carbon electrode and left for approximately 45 minutes for the solvent to evaporate. Due to the hydrophobicity of both glassy carbon and the polyether ether ketone (PEEK) plastic electrode shroud, drop cast inks would often deposit on both the electrode surface and PEEK surround. The amounts of Nafion were varied from 20 μL - 200 μL , the resulting modified electrodes are detailed in Table 4.2. Initial assessment of each film resulted in one of three conclusions – ‘Unstable’ indicates that once submerged, the catalytic film detached from the electrode surface entirely. ‘Stable’ indicates a stable film is retained on the electrode surface, with no evidence of detachment or degradation. ‘Partial’ indicates a known partial detachment of the film in which the film remains in contact with the electrode surface in part.

It was observed that significant amounts of binder were necessary to successfully adhere the MXene/Nafion film to the GCE surface. At the lowest Nafion concentration of 20 $\mu\text{L}/\text{mL}$, MXene was seen to disperse into the electrolyte upon submersion. The film then appeared to detach from the electrode surface and fall to the bottom of the cell in small pieces, dispersing more as it fell. As the concentration of Nafion was increased to 100 $\mu\text{L}/\text{mL}$, once submerged the catalyst film did not disperse, but instead began to ‘flake’ and break apart into large, flat pieces, rapidly

sinking with gravity. These observations have been attributed to the binding of MXene flakes to one another without achieving an adhesion to the electrode surface. At low concentrations, the MXenes are in contact with less binder and therefore disperse readily into solution, however, at higher Nafion concentrations, the material is bound together thus preventing its dispersion. At 250 $\mu\text{L}/\text{mL}$, the Nafion concentration appeared to be high enough to successfully bind the MXene material together, with partial adhesion of the film to the electrode. Upon inspection, the Nafion appeared to bind the film together and attach the film to the PEEK surrounding, rather than the GCE surface itself. At 500 $\mu\text{L}/\text{mL}$, the Nafion concentration was high enough to form a stable film on the surface of the electrode. This ratio of Nafion to catalyst is significantly higher than typically seen for immobilising catalysts, a ratio of near 100 times larger than commonly reported.

MXene (mg/mL)	Binder	Amount of Binder per mL	Drop cast volume	Film Stability
10	Nafion	20 μL	20 μL	No
10	Nafion	50 μL	20 μL	No
10	Nafion	100 μL	20 μL	No
10	Nafion	250 μL	20 μL	Partial
10	Nafion	500 μL	20 μL	Yes

Table 4.2 - Nafion binder amount evaluation

A similar evaluation of the drop-cast volume was conducted using increased Nafion concentrations of 250 μL and 500 μL . The drop-cast volume was increased from 10 μL to 30 μL in 10 μL increments to assess the stability of the resulting catalyst film.

MXene (mg/mL)	Binder	Amount of Binder per mL	Drop cast volume	Film Stability
10	Nafion	250 μL	10 μL	No
10	Nafion	250 μL	20 μL	Partial
10	Nafion	250 μL	30 μL	No
10	Nafion	500 μL	10 μL	No
10	Nafion	500 μL	20 μL	Yes
10	Nafion	500 μL	30 μL	No

Table 4.3 - Drop cast volume evaluation using Nafion binder

At the low drop cast volume of 10 μL , the resulting film failed to adhere to the GCE surface. Interestingly, at 10 μL , the outer diameter of the droplet was within the entire GCE area, where, for volumes exceeding 10 μL , the droplet would spread beyond the active surface area due to wetting. For the high drop cast volume of 30 μL , the resulting film appeared to peel at the edges prior to submersion in the electrolyte. This is likely due to the increased drying rate at the edge of the electrode as previously discussed. Additionally, due to the larger volume of solvent, the drying time of the modified electrode will be significantly increased, thus exaggerating the coffee ring effect resulting in an inhomogeneous film. For these reasons, 20 μL was deemed the optimal drop cast volume and was used in further investigations.



Figure 4.6 - Aqueous $\text{Ti}_3\text{C}_2\text{T}_x$ dispersion following EtOH addition

To investigate the effects of drying time on the drop cast catalyst film, ethanol (EtOH) was added to the MXene ink to increase the evaporation rate of the solvent, thus minimising the coffee ring effect. As previously discussed, EtOH appears to have a detrimental effect on the delamination of MXene sheets. For this reason, the MXene was delaminated via probe sonication prior to EtOH addition. In initial testing, a $\text{Ti}_3\text{C}_2\text{T}_x$ ink was made with a 1:1 ratio of DI:EtOH before Nafion was added and

homogenised via shaking. Prior to the drop casting, the MXene ink began to separate with agglomerations of MXene particles precipitating from the ink and falling to the bottom of the vial. Figure 4.6 shows the agglomerated $Ti_3C_2T_x$ particles precipitated from the EtOH ink solution. This phenomenon was also observed in the delamination study previously reported in Chapter 4.3.1.

An alternative approach to manufacturing a stable MXene/Nafion modified electrode is the layering of components. The principal idea was to initially dropcast a binder-free MXene film onto the GCE surface, and once dried, subsequently dropcast a Nafion binder layer on top of the MXene film, effectively pinning the underlying film to the electrode surface.

[a] Firstly, a binder-free MXene ink was drop cast on the GCE electrode before being left to dry. Next, 5 μ L of Nafion was drop cast directly over the MXene film and left to dry. Once dry, the modified electrode showed signs of cracking and peeling on the surface, as shown in Figure 4.7. The MXene layer beneath appears unchanged, however, the Nafion outer layer appears to peel and crack exposing the MXene underneath. This is likely due to the rapid drying of the Nafion binder, causing the film to dehydrate and crack, a finding which has been previously reported by Lei et al. for Nafion binder in fuel cell applications.

[b] To negate the effects of the rapid drying of Nafion binder, a Nafion solution was prepared with a 1:1 ratio of binder to DI water which was subsequently drop-cast over a pre-prepared MXene electrode. Upon contact of the Nafion solution with the MXene film, the catalyst layer began to shift, ultimately cracking at multiple sites and shifting across the electrode, exposing in areas the GCE surface beneath. Figure 4.7 shows the newly prepared MXene-modified GCE following the drop cast of Nafion solution. The water component of the Nafion solution has disturbed the dry MXene film causing it to degrade and detach from the surface of the GCE.

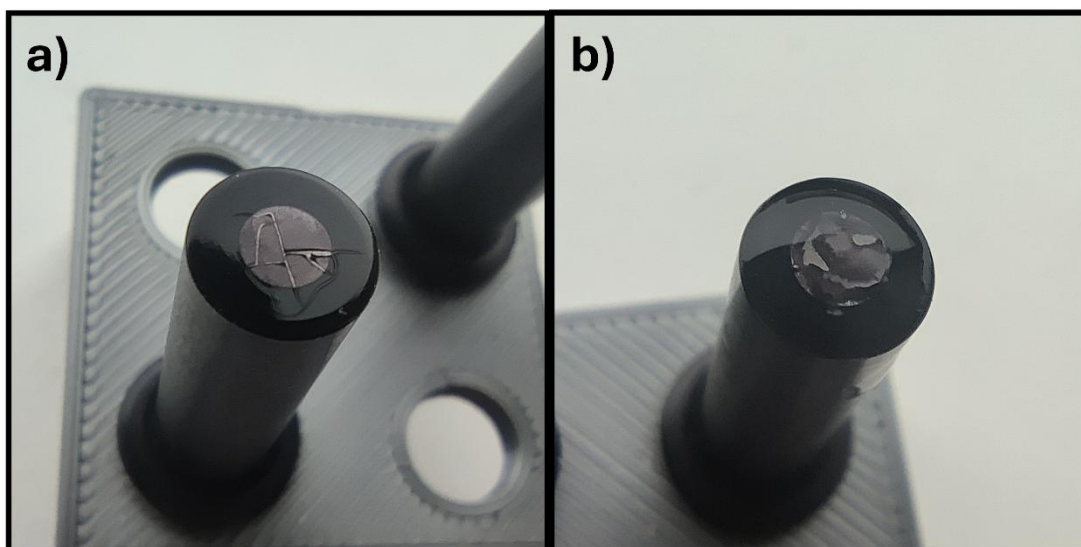


Figure 4.7 – Nafion/Ti₃C₂T_x modified GCE electrodes with a) 5 μ L of Nafion drop cast layer b) 50% Nafion solution

Due to the inherent challenges of using Nafion for catalyst immobilisation, an alternative binder was assessed for the manufacture of MXene modified electrodes. PEDOT:PSS is a polymeric binding agent, typically used in electrochemical devices due to its high conductivity and mechanical flexibility. Initial testing involved the optimisation of binder amounts, as previously done with Nafion binder. The results of the resulting films are detailed in Table 4.4.

MXene (mg/mL)	Binder	Amount of Binder per mL	Drop cast volume	Film Stability
10	PEDOT:PSS	20 μL	20 μ L	No
10	PEDOT:PSS	50 μL	20 μ L	Partial
10	PEDOT:PSS	100 μL	20 μ L	Yes
10	PEDOT:PSS	250 μL	20 μ L	Yes
10	PEDOT:PSS	500 μL	20 μ L	Yes

Table 4.4 – PEDOT:PSS binder evaluation

Interestingly, significantly lower amounts of PEDOT:PSS binder were required to form a stable MXene film when compared to Nafion. With only 50 μ L of PEDOT:PSS, a homogenous film was produced, which detached from one side of the GCE following submersion in the electrolyte. Interestingly, once detached, the film remained intact, despite mechanical agitation of the electrode. When the amount of PEDOT:PSS binder was increased to 100 μ L, the resulting MXene film remained

stable on the electrode following a 5-minute submersion in KHCO_3 [0.1M] electrolyte. Once the film had been removed from the electrolyte, it was allowed to dry before being resubmerged to assess whether the modified electrodes were reusable. Following a re-submerging of the electrode, the MXene/PEDOT:PSS film detached from the electrode and sank to the bottom of the cell while remaining intact. This interaction suggests that the instability of the film is due to the lack of adhesion to the electrode surface, as previously seen with Nafion binder. While PEDOT:PSS satisfied the criteria for an ideal binding agent, the adhesion of the film to the electrode surface was not sufficient. Alternative methods of film formation were considered, with electropolymerisation identified as a key candidate for further study.

To assess the surface morphology of both the Nafion/MXene and PEDOT:PSS/MXene modified electrodes at 500 $\mu\text{L}/\text{mL}$ and 100 $\mu\text{L}/\text{mL}$ binder concentrations respectively, SEM images of the electrode surface were obtained and presented in Figure 4.8.

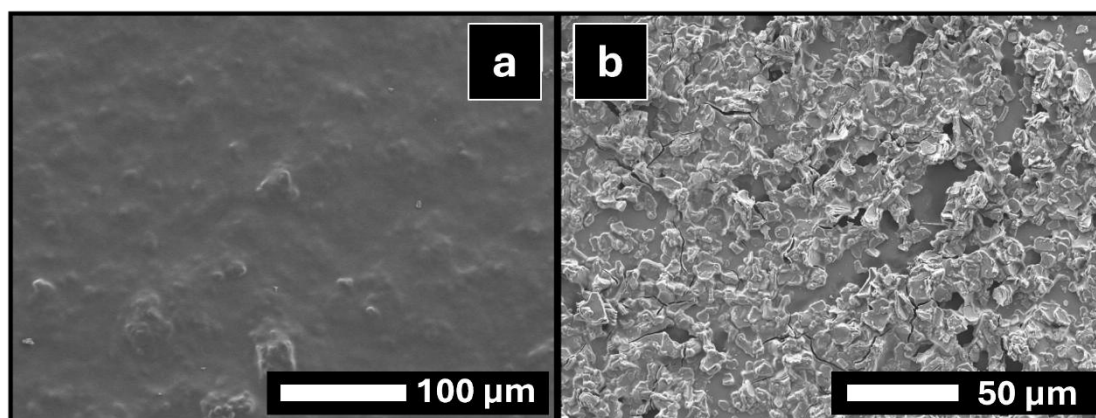


Figure 4.8 - SEM images of a) Nafion(500 $\mu\text{L}/\text{mL}$)/MXene-modified electrode, x 270 b) PEDOT:PSS(100 $\mu\text{L}/\text{mL}$)/MXene-modified electrode, x 500)

From observing the SEM images obtained for the Nafion-containing electrode, the surface appears significantly smoother than expected. At a magnification of x 270, it is apparent that the Nafion is forming a film, entirely covering the MXene layer beneath, with no obvious MXene material visible. Large particles can be seen at points across the surface, but no layering is observed. With such a significant Nafion coverage, access to the MXene is blocked entirely, therefore the electrode is unsuitable for assessing the activity of $\text{Ti}_3\text{C}_2\text{T}_x$ for CO_2RR . For PEDOT:PSS, with a

significantly lower amount of binder used for the film formation, the MXene morphology can be seen clearly in the presented SEM image. Individual particles can be recognised with distinct layering observed throughout the material. In the negative spaces between MXene particles the PEDOT:PSS binder can be seen forming a layer on the electrode surface while also forming a thin layer over the MXene particles thus successfully binding the material with the electrode surface. Interestingly, cracks in the PEDOT:PSS film can be seen throughout the sample, which potentially accounts for the deterioration of the film observed under prolonged electrolyte exposure. These cracks likely promote the degradation and subsequent loss of the film on the electrode surface. Additionally, cracks have the potential to afford electrolyte direct access to the GCE surface, resulting in significantly faster film degradation rates should gas products evolve on the GCE and push the film from the electrode. While the formation of a stable binder/MXene film was achieved, both PEDOT:PSS and Nafion binders present individual challenges for the manufacture of efficient MXene-modified electrodes.

4.3.3 Free-standing MXene Film

MXene - $\text{Ti}_3\text{C}_2\text{T}_x^{\text{NB}}$

For the fabrication of a free-standing $\text{Ti}_3\text{C}_2\text{T}_x$ film from a commercial powder, vacuum filtration was utilised to filter and dry the MXene flakes following delamination. Initial attempts involved the probe sonication-assisted delamination of Ti_3C_2 in DI water. Following sonication the MXene was filtered via high-vacuum filtration using Nylon filter paper. The resulting MXene film when then left to dry on the filter paper under vacuum at room temperature for 4 hours. One fabricated, attempts were made to peel the film from the electrode as reported in the literature. Upon peeling, there was no structural integrity to the film and instead appeared to be a dry powder. The film was then washed to assess its structural integrity under aqueous conditions. Figure 4.9 shows video stills of the washing procedure with DI water, upon immediate contact with the water, MXene material is washed from the filter paper and disperses into an ink. Following washing, small amounts of MXene remained on the filter paper, however upon agitation, the MXene fully dispersed into the water.

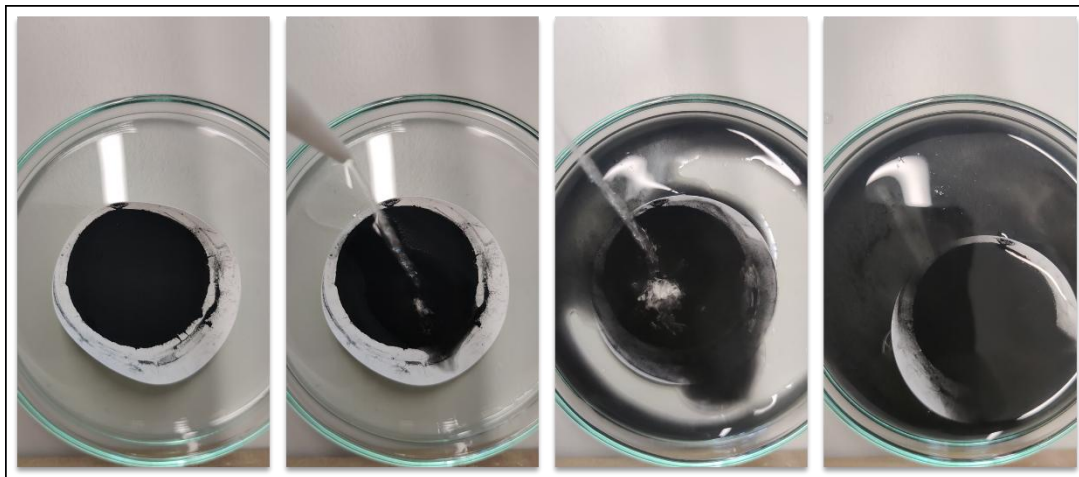


Figure 4.9 - Images of the washing of a vacuum-filtered $\text{Ti}_3\text{C}_2\text{T}_x$ MXene film

It was concluded that although the level of delamination following sonication was insufficient to yield flakes suitable for a free-standing film, a more aggressive or prolonged sonication would likely lead to a deterioration of the MXene flakes thus deactivating it as a catalyst. In order to form free-standing binder-free MXene films, it is suggested that the fabrication is carried out directly following MXene synthesis using large defect-free MXene flakes.

4.3.4 Electropolymerisation of EDOT

MXene - $\text{Ti}_3\text{C}_2\text{T}_x^{\text{NB}}$

The electropolymerisation of 3,4-ethylenedioxythiophene (EDOT) was utilised for the fabrication of MXene-modified electrodes. Firstly, electropolymerisation parameters were evaluated for EDOT in a bespoke electrochemical cell to optimise the electropolymerised film. The bespoke electrochemical cell is shown in Figure 4.10. In this cell, the counter electrode is located at the top of the cell, directly opposite the working electrode. The reference electrode is oriented sideways and located between the working and counter electrodes. Finally, the working electrode is situated at the bottom of the cell and is inverted in an attempt to mitigate the effects of gravity on the drop-cast MXene film.

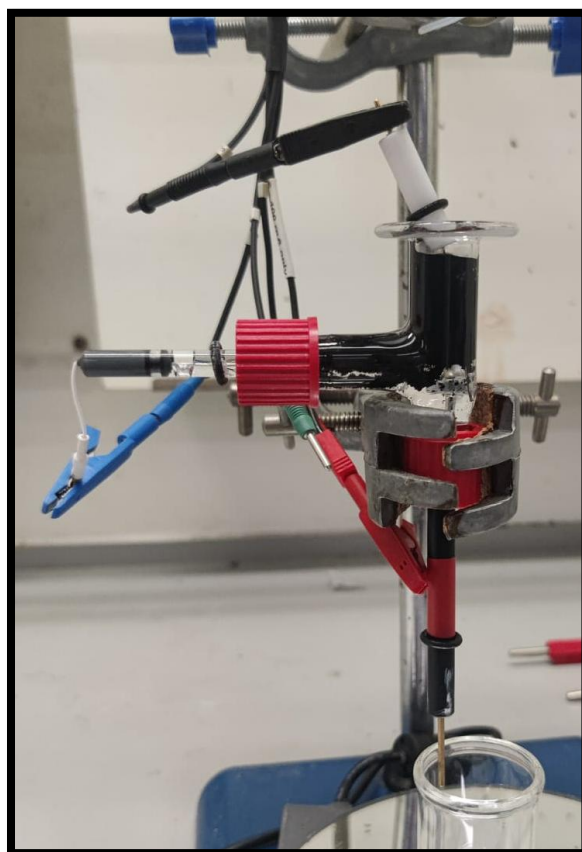


Figure 4.10 – Bespoke electropolymerisation cell with a glassy carbon electrode (red), Ag/Ag⁺ reference (blue), and Pt counter electrode (black)

Since no binder is present in the drop-cast MXene film before electropolymerisation, great care is taken when filling the cell with electrolyte via syringe as there is a need to avoid mechanical disturbances of the fragile film. Acetonitrile (MeCN) was chosen as a solvent for the electropolymerisation of EDOT due to its high ionic conductivity,

low viscosity, and tendency to suppress the hydrogen evolution reaction. This is significant as hydrogen evolution has the potential to compete with the electropolymerisation process and reduce the overall efficiency of film formation.

Following the electrochemical parameters reported by Seki et al.,¹⁷¹ electropolymerisation was performed on a bare and MXene-modified glassy carbon electrode at 1.52 V (vs Ag/Ag⁺) for 480 seconds in nitrogen-sparged MeCN. Following electropolymerisation, a uniform dark blue/black film was deposited on the surface of the glassy carbon electrode. Next, the electropolymerisation was repeated using a Ti₃C₂T_x-modified glassy carbon electrode.

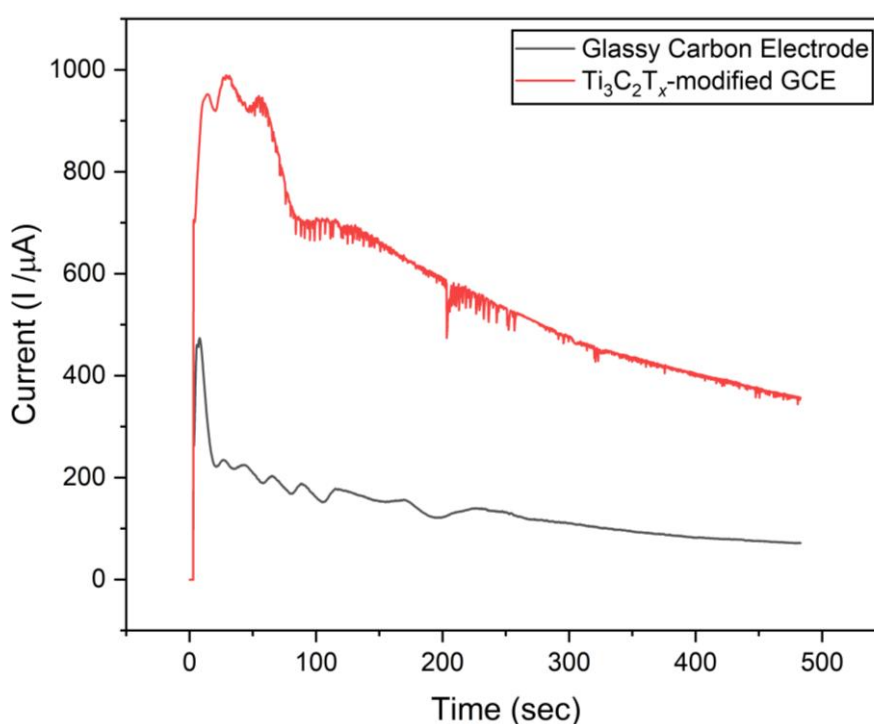
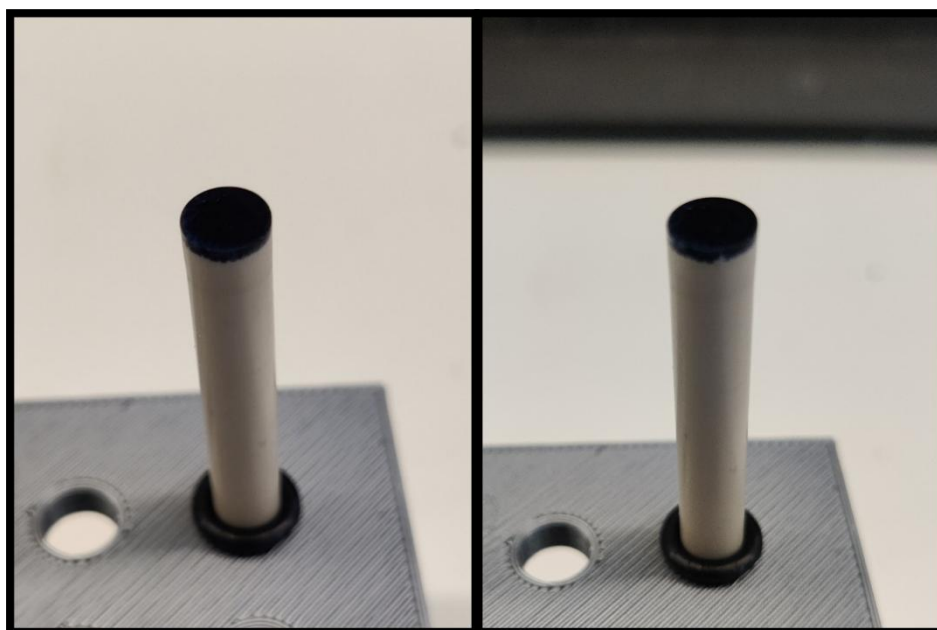


Figure 4.11 - Chronoamperogram of electropolymerised PEDOT for 480s in MeCN on a) black - Glassy carbon electrode, b) red - Ti₃C₂T_x-modified GCE

The chronoamperometry for the electropolymerisation of EDOT on modified and unmodified glassy carbon electrodes is presented in Figure 4.11. Initially, both electrodes show a rapid current spike, indicating a rapid polymerisation and growth phase of the EDOT monomers to PEDOT. Throughout the course of the reaction, the current decays gradually, this indicates that the polymer growth becomes slower as the resulting film becomes thicker. With the MXene-modified GCE exhibiting a higher initial current with a slower decay rate compared to the untreated GCE, it may

suggest that the MXene surface enhances the deposition process, providing a more favourable surface for EDOT polymerisation.

The resulting PEDOT/MXene modified GCE is shown in Figure 4.12 before and after washing with deionised water. No visible changes to the electrode surface are observed following washing, indicating a stable MXene-incorporated electrode. Scanning electron microscopy was employed to survey the morphology of the PEDOT/MXene-modified electrode.



**Figure 4.12- Images of the electropolymerised PEDOT/MXene-modified GCE
a) before washing with water b) after washing with water**

SEM images of the film were taken at varying magnifications to assess the coverage, quality, and effectiveness of the film formation. Figure 4.13 shows an SEM image taken at x150 magnification. The image shows an overall uniform coverage of the polymer, with polymeric agglomerations distributed evenly over the surface of the electrode. No cracks or tears in the film are visible at this magnification, suggesting a successful electropolymerisation of a PEDOT film.

The polymer agglomerations were then assessed at a higher magnification of x1000. When magnified, the polymer regions appear 'fluffy' and 'cauliflower-like', protruding outwards from the surface of the electrode. A uniform coverage of the polymer can be seen, with local regions of large and small agglomerations distributed across the surface. MXene material is also present in regions closer to

the electrode surface which appear accessible beneath the polymer coating. PEDOT is also believed to partially grow on the surface of the MXene sheets due to the excellent conductivity.

An interesting MXene/PEDOT interaction was observed at x4300 magnification. The polymer appears to anchor the lower layer of a ML-MXene flake while leaving the upper layers exposed to the electrolyte. This appears to be an ideal interaction, with the polymer securing the MXene to the electrode surface, while still ensuring a large, catalytic basal-plane surface area is accessible to the electrolyte.

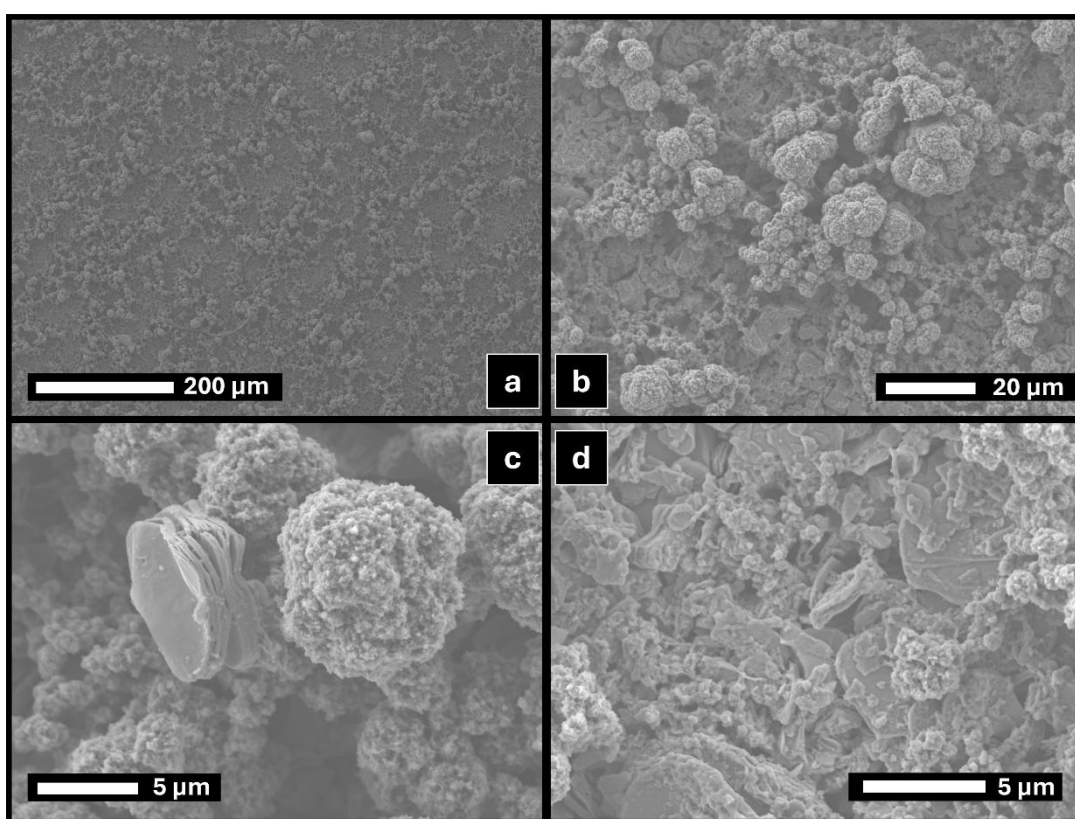


Figure 4.13 – SEM images of an electropolymerised PEDOT/MXene-modified glassy carbon electrode at a) $\times 150$ b) $\times 1,000$ c) $\times 4,300$ d) $\times 3,300$

A novel PEDOT/ $\text{Ti}_3\text{C}_2\text{Tx}$ -modified glassy carbon electrode was successfully fabricated. The electropolymerisation of PEDOT over a drop-cast MXene film resulted in a stable composite electrode. The PEDOT film serves as a binding matrix, anchoring the MXene material to the electrode surface and facilitating electrolyte access to the MXene basal planes for electrocatalytic applications.

4.5 Conclusions

Firstly, we report the extensive evaluation of delamination methods for commercial samples of $\text{Ti}_3\text{C}_2\text{T}_x$. The optimal MXene delamination was achieved using a combination of probe sonication with the chemical intercalation of DMSO not only to effectively delaminate MXene sheets but to prevent their restacking also. Despite DMSO being one of the most widely reported intercalants, the evaluation of alternative intercalants, specifically those with lower boiling points, would prove attractive for drop-casting applications.

In addition, the $\text{Ti}_3\text{C}_2\text{T}_x$ -modification of a glassy carbon electrode was explored via drop-casting. The comprehensive screening process accounted for a wealth of variables, including ink compositions and concentrations, drop-casting solvents, sonication methods, drying methods, and alternative binding agents among others. While stable MXene-modified electrodes were achieved via significantly larger amounts of binder than typically reported in the literature, the volumes necessary would be severely detrimental to any subsequent electrochemistry and would not be representative of $\text{Ti}_3\text{C}_2\text{T}_x$.

Next, the fabrication of a free-standing $\text{Ti}_3\text{C}_2\text{T}_x$ film was attempted via delamination followed by vacuum filtration, as reported in the literature. Typically, free-standing films are fabricated directly following MXene synthesis. Considering the results presented herein, the fabrication of free-standing MXene films from commercial samples proves significantly more challenging. This aligns with reports in the literature suggesting commercial MXenes are significantly more challenging to delaminate than their freshly synthesised counterparts.

Finally, the electropolymerisation of EDOT was attempted for the fabrication of PEDOT/MXene-composite electrodes for CO_2RR applications. A stable PEDOT/ $\text{Ti}_3\text{C}_2\text{T}_x$ was successfully fabricated and characterised via SEM imaging. The resulting images show a uniform coverage of the polymer with MXene material distributed evenly over the surface of the electrode, specifically with accessible MXene basal planes while simultaneously being anchored in place by the polymer matrix. Due to the inherent conductivity of both $\text{Ti}_3\text{C}_2\text{T}_x$ and PEDOT, this study

provides promise in the advancement of efficient MXene-based electrodes for CO₂RR.

5 CO₂RR Electrochemical Cell Design

5.1 Introduction

Three-electrode cell (3EC) voltammetry is by far the most common and widely used electrochemical technique for the study of redox processes, electrode characterisation, and analyte detection.^{115,116} The fundamental configuration of a 3EC consists of a working electrode, a reference electrode, and a counter electrode with the working electrode facing downward in common practice.

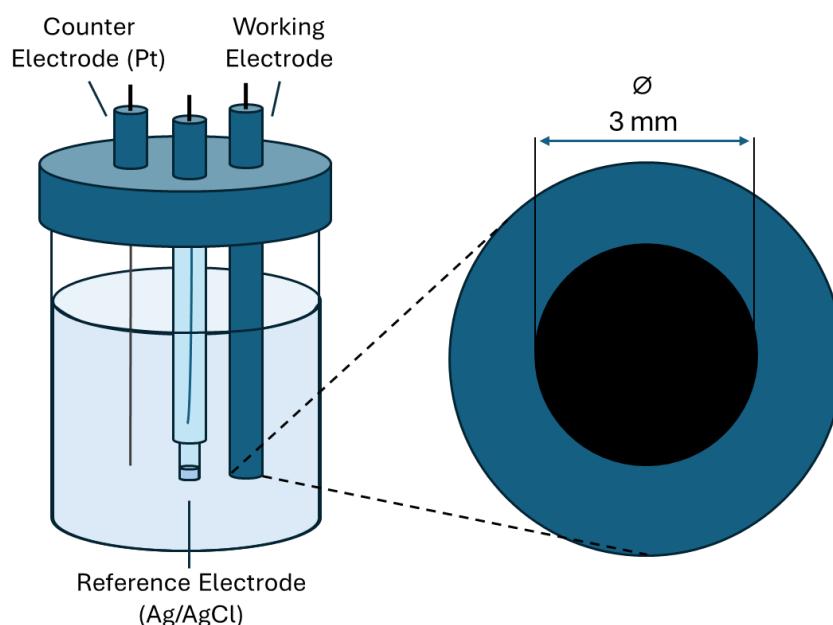


Figure 5.1 - [Left] Traditional three-electrode cell with a Pt counter electrode, Ag/AgCl reference electrode, and glassy carbon working electrode [Right] Glassy carbon electrode (GCE) surface

The most widely used electrochemical technique to assess CO₂RR catalytic activity and selectivity is chronoamperometry, in which a fixed potential is applied for a determined amount of time while the current is measured.¹¹⁶ Chronoamperometric experiments are typically run as a batch process, meaning that the system is isolated with a finite amount of reactant CO₂ in the system. Over the course of the reaction, CO₂ is consumed, producing in most cases, gas and liquid products which remain in the reaction vessel. These products can then be sampled and a faradaic efficiency for each product can be calculated using the total charge passed.

The most common reactor type used for CO₂RR bulk electrolysis research is the H-type cell (H-Cell) which consists of two compartments, an anodic and a cathodic.¹⁷⁶ The working electrode (cathode) is housed with the reference electrode in the cathodic compartment, while the counter electrode (anode) is housed in the anodic compartment. The compartments are separated by a membrane, most often either proton exchange membranes (PEMs) or anion exchange membranes (AEMs).¹⁷⁷ PEMs, such as Nafion, are used to facilitate proton transport while ensuring the isolation of reaction products from the cathodic and anodic processes. Should this membrane be absent, reaction products from either compartment can migrate to the counter compartment may undergo subsequent reactions and drastically reduce the overall efficiency of the system. Hydrogen's tendency to diffuse through components, due to its small molecular size, means that all H-cell set-ups must achieve a complete gas-tightness and be checked periodically for leaks to ensure accurate product quantification.

For the sampling of products from an H-cell following CO₂RR, typically both the gas and liquid phase products are sampled via syringe insertion.¹⁷⁸ For liquid sampling, a known volume of electrolyte is taken via syringe and subsequently analysed using liquid-sampling methods such as NMR, HPLC, and IC. For gas samples, a gas-tight syringe is used to withdraw a known amount of gas from the headspace of the reactor. This sample is then directly injected into a GC for gas-phase product analysis where the number of moles of gas are subsequently calculated. This methodology, however, does not consider any overpressure within the reactor cell from evolved gases and therefore does not provide an accurate quantification of gas-phase products. For accurate product analysis, the internal pressure of the cell must be

known. By using the ideal gas law and the known ratios of the gas mixture from GC-BID measurements, the number of moles of each gas component can be accurately calculated, thus providing accurate selectivity and activity data for any catalyst.¹⁷⁹

A recent publication by Diercks et al. details a novel gas chromatography setup which allows the real-time monitoring and quantification of eCO₂RR products.¹⁸⁰ The automated sampling and analysis set-up continuously flushes the GC sample loop with the product gas stream until 'injection mode' is initiated, at which point the sample loop is then flushed to the column for analysis. Although the electrochemical cell is directly attached to the GC, the system is not a true real-time analysis due to the length of time necessary for sample separation. To achieve adequate peak separation for the multitude of CO₂RR reaction products, a GC method of at least 10 minutes is necessary. Despite the elegance of the system, it would be possible to achieve similar results by the continuous sampling of a batch electrolysis experiment. While the replenishment of CO₂ may not be possible in a batch process, the ability to monitor product formation over time may be achieved if the chosen method allows for short run times >10 min. To achieve an absolute real-time analysis of CO₂RR product formation, an alternative analytical technique is required.

Differential electrochemical mass spectrometry (DEMS) has been reported for the real-time monitoring of CO₂RR reaction products and allows for the identification and quantification of products almost immediately.^{181,182} This technique can also be used to identify how product distribution changes with varying applied potentials, providing a key insight into the reaction mechanisms of CO₂RR and the individual behaviour of electrocatalysts. In order to accommodate various electrode geometries, bespoke electrochemical cells have been reportedly integrated into a DEMS set-up. In this case, there can be a slight lag in bespoke cells between the generation of products in the electrochemical cell and the analysis of those products at the inlet due to the slow transport of electrolyte through the system. This lag, however, can be compensated in post via a series of calibrations. One significant concern regarding DEMS systems is the generation of bubbles. While the mass-spec inlet of a DEMS system is capable of sampling dissolved gases, problems arise when large gas bubbles pass over the inlet, often causing a spike in the real-time data.

These formed bubbles are problematic as the evolved gas is not accurately quantified, and so efforts to reduce bubble formation during electrolysis are paramount in ensuring accurate product quantification.

To date, the golden standard of CO₂RR product analysis has not yet been identified. While several flow and batch electrolysis methods have been reported, each technique and subsequent analysis has its advantages and disadvantages. This thesis chapter will detail the rational design, manufacture, and implementation of bespoke electrochemical cells for CO₂RR catalyst evaluation. First, the classic 3-electrode cell has been redesigned to accommodate a wealth of electrode geometries while mitigating the effects of gravity on a catalyst film. For CO₂RR electrolysis, considerations have been made for the current reactor design challenges mentioned herein, with the primary focus on the design of a batch electrolysis cell, capable of collecting all CO₂RR products while allowing facile sample submission.

5.2 Materials and Methods

5.2.1 Reagents and Equipment

Potassium hydrogen carbonate and ruthenium hexamine were purchased from Fisher Scientific. All solutions were prepared using Milli-Q[®] ultrapure water (resistivity 18.2 MΩ/cm).

All electrochemical measurements were performed using an IviumStat potentiostat (Ivium) using Iviumsoft software. The glassy carbon plate working electrode, Ag/AgCl reference electrode, and Pt wire counter electrodes were all purchased from IJCambria Scientific LTD.

Carbon dioxide (>99.99%) and calibration gas (1000 ppm of hydrogen, methane, ethylene, carbon monoxide, helium balanced) cylinders were provided by BOC UK.

Standard photopolymer resin was purchased from AnyCubic. PLA filament (1.75mm) was purchased from RS Components.

Swagelok components were purchased from Swagelok.

Polypropylene and sheet acrylic was provided by Lancaster University Physics Department

5.3 Results and Discussion

5.3.1 3-Electrode Cell for Catalyst Evaluation

5.3.1.1 Design and Rationale

The standard 3-electrode electrochemical cell has been redesigned, primarily to allow for a multitude of electrode morphologies. This new design facilitates the electrochemical characterisation of a large-area plate electrode, such as a glassy carbon plate, which has been modified with MXene material. These modified electrodes can then be translated directly into an electrolysis cell for eCO₂RR. During the catalyst preparation, typically a catalyst ink is drop-cast onto a substrate and the solvent is evaporated.

The working and reference electrodes have been configured symmetrically with the aim of improving the stability of the cell, such that there will be no uneven current distribution and the potential difference will be less susceptible to fluctuations.

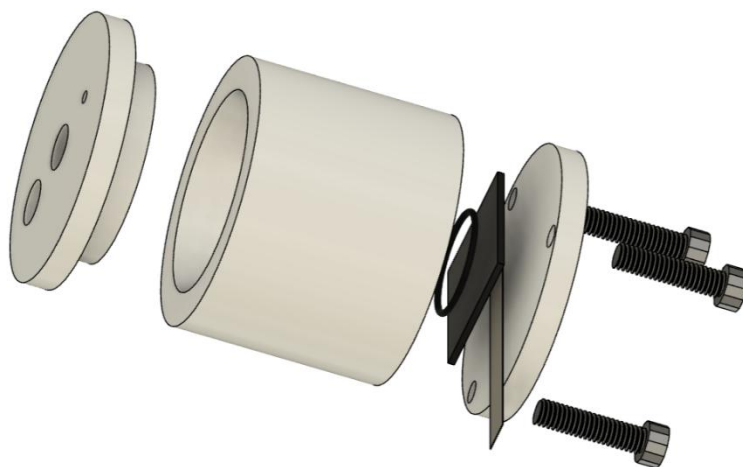


Figure 5.2 - 3D render of a bespoke 3-electrode electrochemical cell modelled in Fusion360

As mentioned previously, it is suspected that gravity may be influencing the deterioration and detachment of the drop-cast MXene film. The inverted geometry of the re-designed cell ensures that gravity will no longer have an effect on the drop-cast film. Additionally, the ‘peeling’ of the catalyst film, which was previously observed at the edges, has been mitigated in this new design using an O-ring. In addition to ensuring a water-tight seal, the O-ring effectively ‘pins’ down the catalyst film with no edges present inside the ring.

Finally, due to the high chemical resistance of polypropylene, this cell is suitable for both aqueous and non-aqueous electrochemistry.

5.3.1.2 Prototyping

The bespoke 3-electrode cell was designed in Fusion360™. The generated .STL files were then imported into PrusaSlicer, where the individual models were arranged on the build plate and printing parameters were confirmed. Using the exported .gcode, the model was printed via FDM additive manufacturing (Prusa i3 MK3S+) using PLA filament (1.75 mm, grey). Following printing, the parts were smoothed with sandpaper.

During initial testing, the cell operated as expected providing a liquid tight seal during operation. Following testing, modifications were made to the circular opening adjacent to the electrode surface. This was optimised for efficient mass transport of the electrolyte and dissolved species to the electrode surface. PLA was considered unsuitable for the final design due to its propensity to swell when in contact with moisture and its lack of tensile strength.

Final designs were then milled from acrylic, due to optical clarity, for aqueous applications, and from polypropylene for non-aqueous applications.

5.3.1.3 Assembly and Operation

Firstly, the main cell body is inverted, and an O-ring is placed over the small-diameter opening. An electrode is then placed centrally on the O-ring before a short strip of nickel-plated steel ribbon is added to the top leaving >1 cm overhanging from the cell. Finally, the base plate is added ensuring the threads are aligned with those of the main body and secured using 3 x M6 screws which are tightened carefully to ensure an even pressure distribution. The cell is then inverted, and an electrolyte is added to the cell. The lid is finally added, and the reference electrode is placed in the centre, with the counter electrode and gas line added to the large- and small-diameter holes respectively.

5.3.1.4 Preliminary Results

MXene - $\text{Ti}_3\text{C}_2\text{T}_x^{\text{NB}}$

Cyclic voltammetry was performed on a glassy carbon plate in the redesigned 3-electrode cell using a $[\text{Ru}(\text{NH}_3)]^{3+/2+}$ redox couple in potassium hydrogen carbonate with a scan rate of 100 mV/s. The resulting voltammogram presented a clearly defined redox peak, achieving a peak-to-peak separation of 75 mV (vs Ag/AgCl), which is within the expected range, suggesting a well-behaved system with reasonably fast electron transfer kinetics. The nature of the redox couple borders on that of a quasi-reversible process, however, when considering the relatively fast scan rate and large electrode size, the system can be considered reversible.

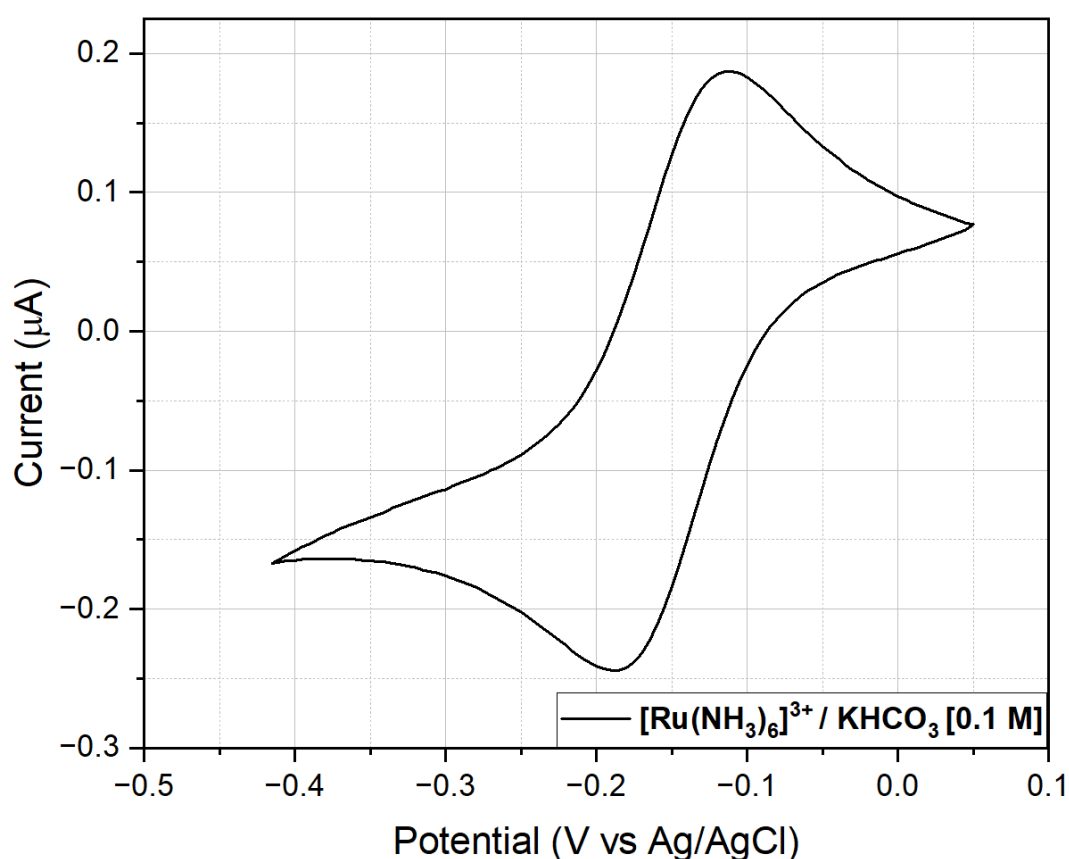


Figure 5.3 - Cyclic voltammogram of $[\text{Ru}(\text{NH}_3)_6]^{3+/2+}$ in 0.1 M KHCO_3 , scan rate of 100 mV/s

Cycling voltammetry was utilised to assess the CO_2RR activity of a MXene/Nafion-modified glassy carbon plate in the newly-designed bespoke 3-electrode electrochemical cell.

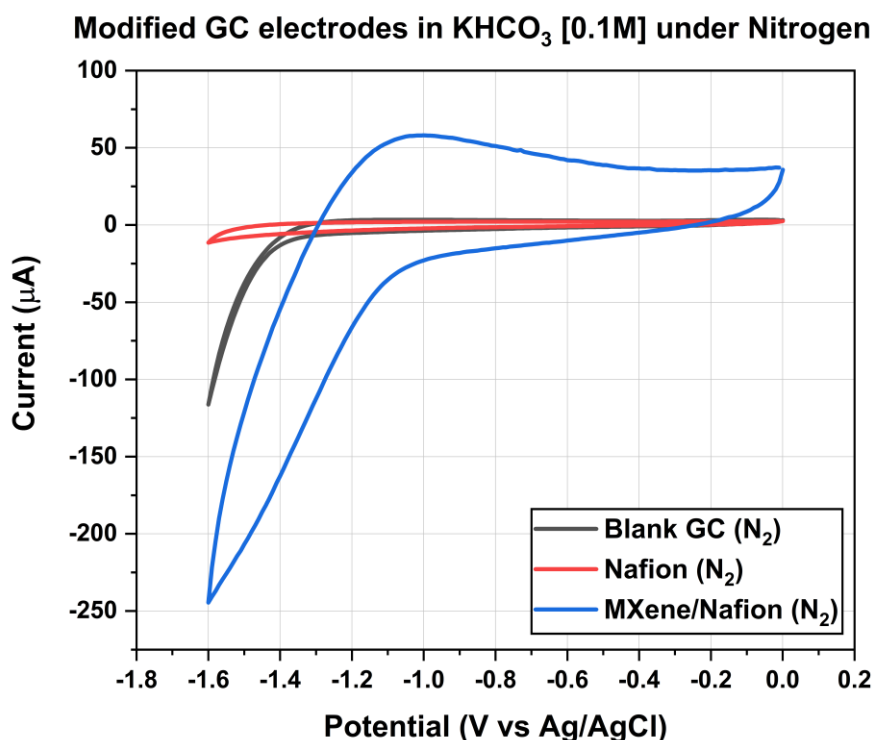


Figure 5.4 – Cyclic voltammogram of a) black – bare glassy carbon electrode b) red – Nafion-modified GCE c) blue – $\text{Ti}_3\text{C}_2\text{T}_x$ /Nafion-modified GCE

Firstly, a bare glassy carbon electrode was subject to cyclic voltammetry to ensure any current response observed for the MXene/Nafion modified electrodes was attributed to the MXene material rather than the glassy carbon surface. Initially, the blank glassy carbon electrode exhibited an increase in current response when approaching 1.3 V (vs Ag/AgCl) which can be attributed to the hydrogen evolution reaction due to the absence of dissolved CO_2 . Next, a Nafion-modified glassy carbon was evaluated, displaying a delayed current response more negative than that of the blank glassy carbon indicating a suppression of the hydrogen evolution reaction. One possible reason for this may be due to the perfluorosulfonic acid groups present in the Nafion binder which can create a hydrophobic environment near the surface of the electrode. This may prevent the adsorption of water molecules onto the modified electrode, thus inhibiting HER. Further investigation is required to determine the factors influencing the observed current response. Finally, a MXene/Nafion modified electrode was evaluated to determine the overpotential necessary to drive HER reaction. The initial steady increase in current response, combined with the large area of the obtained CV suggests the double-layer charging

of the MXene. At -1.0 V (vs Ag/AgCl) an exponential increase in current response is observed indicating the beginning of HER.

To assess the CO₂RR activity of the MXene/Nafion modified electrode, a polished blank glassy carbon plate was subject to cyclic voltammetry in the presence and absence of dissolved CO₂. No significant differences are observed between the two bare GCE voltammograms, however, the current response for the CO₂-saturated electrolyte appears to increase at a slightly less negative potential than the N₂-saturated electrolyte. This is potentially due to the decrease in pH following CO₂ saturation. When CO₂ is dissolved in water, carbonic acid is formed according to the following reaction. This weak acid then can dissociate into hydrogen ions and bicarbonate ions which will lower the pH and make the solution more acidic. Due to the low solubility of CO₂ in aqueous electrolytes, this acidification is unlikely to have a significant influence on the electrochemistry but may account for the slight differences in overpotential observed in the blanks. Next, the MXene/Nafion modified GCE was subject to cyclic voltammetry in the presence of dissolved CO₂. Once again, an initial steady current response was observed attributed to double-layer charging followed by an exponential increase in current response. This sudden current increase began at -0.8 V (vs Ag/AgCl), which is a reduction in overpotential of 200 mV. Owing to the differences between comparable voltammograms and the

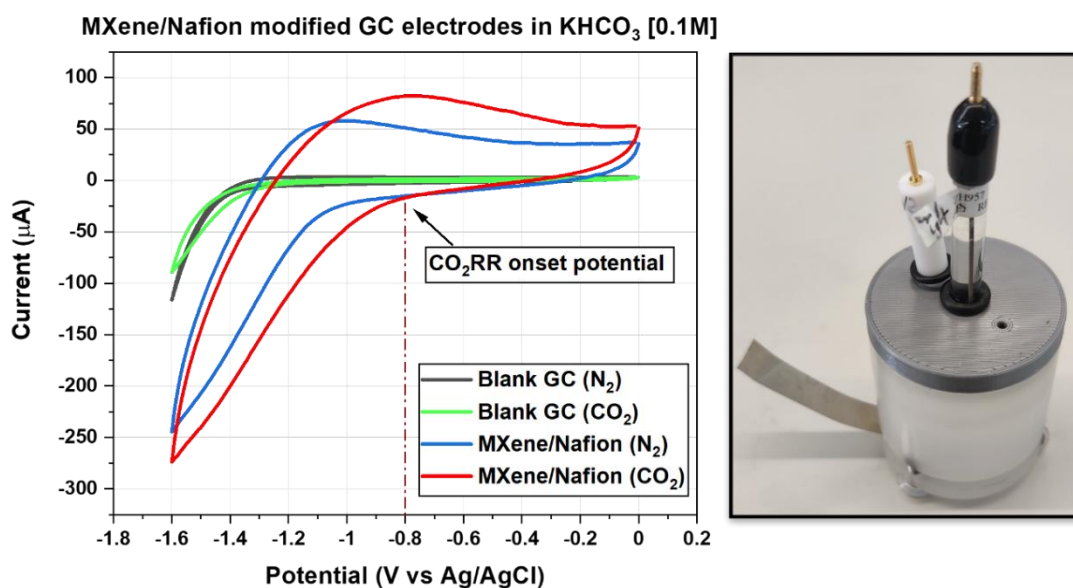


Figure 5.5 - [Left] Cyclic voltammogram of [Ru(NH₃)₆]^{3+/2+} in 0.1 M KHCO₃, scan rate of 100 mV/s. [Right] Image of fully assembled redesigned 3-electrode cell

presence of dissolved CO₂, the current response observed is attributed to the onset of CO₂RR. The 3-electrode cell utilised in this experiment allows the direct translation of the modified MXene/Nafion electrode into a batch electrolysis cell for CO₂RR product analysis.

5.3.2 Batch Electrolysis Cell for CO₂RR

5.3.2.1 Design and Rationale

Due to the multitude of products seen from copper-catalysed CO₂RR, it is crucial to design a reactor that can separate liquid-phase and gas-phase products for analysis.

As previously mentioned, the ability to monitor the internal pressure of a batch electrolysis cell is crucial for the accurate quantification of gas-phase products. To this end, a pressure gauge must be included in the final design of the bespoke electrolysis cell.

In order to quantify all products for accurate catalytic activity, the reactor must be able to effectively retain evolved hydrogen. Due to its small size, hydrogen molecules have a tendency to escape most porous materials and fittings. Swagelok™ components will be incorporated into the acrylic cell to mitigate any hydrogen gas losses.

A suitable reaction vessel should also be capable of sonication due to the likelihood of dissolved gases in the spent electrolyte. Should there be a high concentration of dissolved gases, sonicating the reactor will degas the electrolyte while also removing gas bubbles trapped within the reactor vessel or attached to the electrode, ensuring accurate product quantification.

5.3.2.2 Design Iteration 1. – Downstream Collection Vessel (DCV)

Early designs for the gas/liquid sample vessel featured a two-chamber design for downstream sample collection. One prototype, referred to herein as ‘downstream collection vessel (DCV)’, featured two compartments stacked vertically connected by a Swagelok™ tap, allowing isolation of the individual compartments. In the lower compartment [liquid], an inlet and an outlet are positioned diametrically with Luer lock taps connected to both externally which allow a) an isolation of the vessel entirely should both be closed b) a collection of the gas/liquid mixture should the

outlet tap be closed. Luer lock fittings are used in the lower compartment as this allows rapid detachment post-electrolysis when transporting the vessel to other pieces of sampling equipment. In the upper compartment (gas), a pressure gauge is situated in the top plate to give necessary internal pressure readings. A Swagelok™ tap, 'gas outlet tap' (GOT), is also present in the top compartment to outlet gaseous products for analysis.

5.3.2.2.1 Prototyping

The downstream collection vessel was designed using Fusion360™. The generated .STL files were then imported into CHITUBOX slicer, where the individual models were arranged on the build plate, supports were added to the model, and printing parameters were confirmed. The exported .photon file was finally imported into PhotonFileValidator to validate the file and highlight any discrepancies in the model, supports, and islands. The model was then printed via SLA additive manufacturing (AnyCubic Photon SLA 3D Printer) using a clear photopolymer resin. Following printing, the parts were washed with IPA and left to dry before being cured under UV light for 1 hour. Once cured, all supports were removed and the model was smoothed with sandpaper.

During initial testing, the resin-based prototype was effective in collecting liquid products, however, it did not achieve gas-tightness when approaching 1 bar of internal pressure. Due to the inherent challenges when resin-printing large objects, it is likely that there was a warping of the components due to gravity during printing. This warping did not allow for a tight seal of components in the gas collection chamber, thus leading to a gas leak. In addition, when a warping of components is observed, it is significantly challenging to achieve an even pressure across the components, making the issue of gas tightness even more challenging.

Parts were milled from acrylic due to its rigidity and durability.

5.3.2.2.2 Assembly and Operation

Firstly, both compartments are sealed via 4 x M6 screws with a rubber gasket sandwiched between each compartment and lid to achieve a gas-tight seal. PTFE tape is then used around each seal to prevent any potential gas leak. The central tap (CT) is then attached to both compartments with PTFE tape used around the taper

to achieve a gas-tight fit. Once assembled, the liquid outlet tap is closed, and the bottom compartment is filled with electrolyte to verify its liquid tightness. [CT – Open, GOT – Closed] Nitrogen gas is then bubbled through the electrolyte via the liquid inlet, which will consequently pressurise the gas compartment. Once the pressure reaches 1 bar, the nitrogen purging is ceased and the vessel is sealed for 10 minutes which the pressure gauge is closely monitored for a pressure drop. If a pressure drop is observed, the entire collection vessel can be submerged in water to identify the location of the leak followed by a subsequent tightening of the components local to the leak. The pressure test is then repeated until there is no pressure loss observed and the electrolyte is drained via the liquid outlet read.

For electrochemical CO₂ reduction using an aqueous electrolyte – Firstly, the gas compartment is sparged with CO₂ via the liquid inlet for 5 minutes [CT – Open, GOT – Open] before GOT and LIT are both closed, leaving the vessel at atmospheric pressure. The DVC is then connected to a flow-cell reactor via Luer lock compatible tubing which is fed through a peristaltic pump (peri pump) between the DVC and reaction vessel.

Once the liquid outlet tap is closed, the electrolysis can begin, and the peristaltic pump will begin to push the electrolyte into the DCV. As the DCV has a CO₂ atmosphere at 1 atm, as electrolyte enters, the internal pressure will increase until the liquid compartment is full resulting in a pressure of at least 2 atm. Once the liquid compartment is filled with electrolyte, the electrolysis and peri pump are halted, and the vessel is disconnected and transported to a sonicator. Following sonication, the reaction vessel is connected to the GC-BID where the overpressure of the vessel will be released into the GC sample loop. The spent electrolyte in the liquid compartment can then be sampled – if the electrolysis is to resume, a syringe must be inserted into the liquid outlet tap for sampling, thus creating a slight negative pressure which will be resolved when resuming the peri pump. This process is repeated until the desired electrolysis time or volume is complete. Once the reaction has completed, the gas outlet tap is opened and the electrolyte is drained from the vessel for sampling.

Currently, the internal volume of both gas and liquid compartments is comparable, however, due to the modular design of the compartments – the total volume can be modified to suit the conditions of the reaction.

Although nearly all products can be collected using the DCV, there are still a number of inherent challenges with this method of sampling:

- 1) Any gas bubbles trapped in the flow reactor will not be submitted for analysis. The flow reactor can be engineered to mitigate trapped bubbles, but accounting for all gas products is challenging with such a large system.
- 2) Due to the ex-situ nature of downstream product collection, there is a time delay between generating products and collecting them.
- 3) If a large volume of electrolyte or lengthy electrolysis is necessary, the collection vessel must be regenerated many times to collect all products. Not only is it a complicated process, but also provides the opportunity to introduce human error into the to collect all products. Not only is it a complicated process that is to be repeated, but this also increases the likelihood of human error, with the potential to release gas-phase products or introduce air into the system.

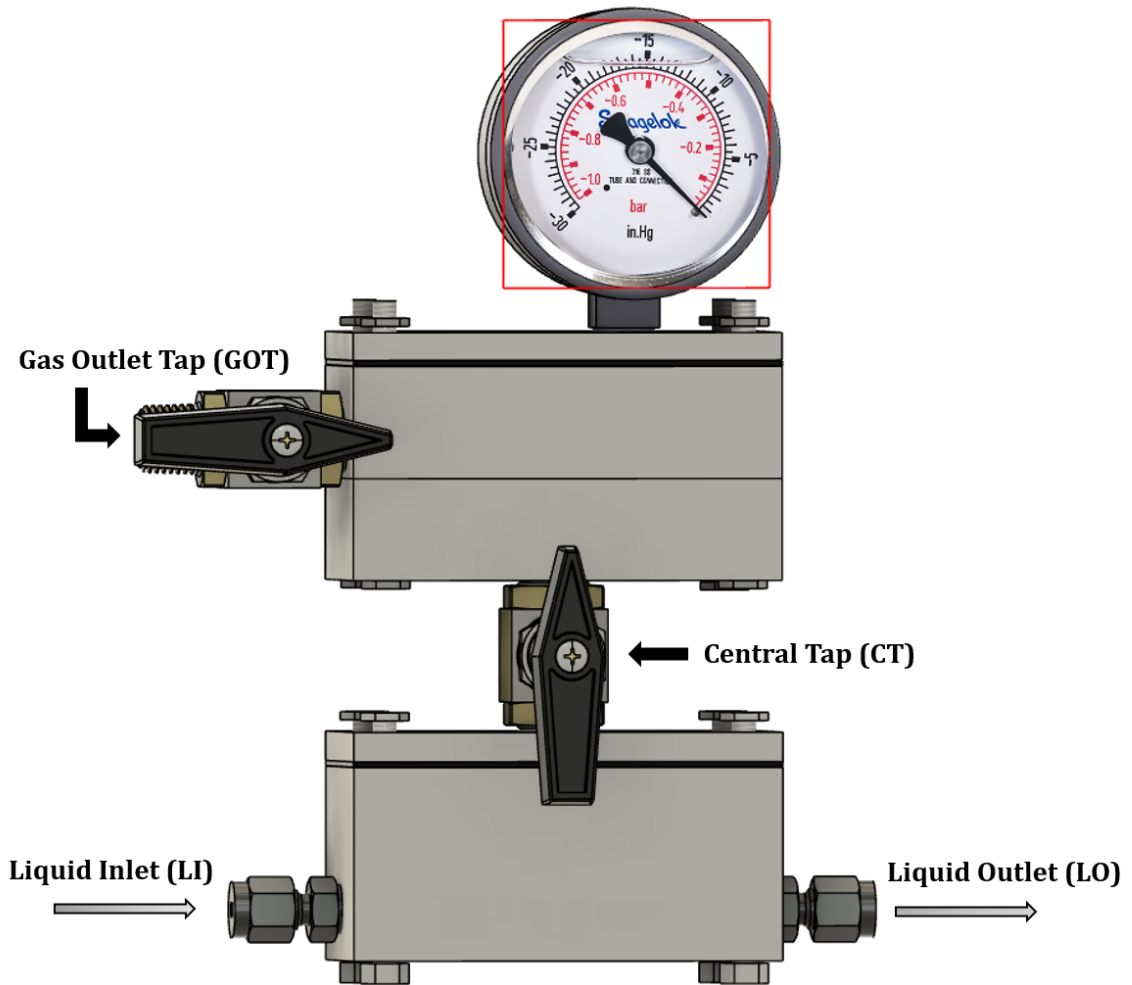


Figure 5.6 – 3D render of the downstream collection vessel (DVC) modelled in Fusion360

5.3.2.2.3 Design Improvements

The inherent challenges presented by the DCV were considered and optimisations were made to both the intrinsic design and operation. A two-chamber design was used for the subsequent iterative prototype so-called “zero-headspace electrolysis cell V1”.

In an effort to address the 3 primary concerns of the DCV previously mentioned, it was decided that the flow cell would be replaced with a batch electrolysis cell which would retain 100 % of the electrolyte in-situ while transporting the gas to a separate vessel.

5.3.2.3 Design Iteration 2. – Zero-Headspace Electrolysis Cell 1 (ZHEC1)

To address the current engineering challenges faced when performing classic H-cell CO₂ electrolysis, a novel zero-headspace H-cell was conceptualised, designed, and prototyped. The newly designed cell, so-called, 'zero-headspace electrolysis cell V1 (ZHEC1)', incorporates a three-compartment design, featuring a working electrode compartment (WEC), counter electrode compartment (CEC), and gas collection compartment (GCC). The WEC and CEC are separated by a proton exchange membrane to allow ion exchange facilitating efficient CO₂ reduction while also preventing the mixing of liquid products between the two compartments. The gas collection compartment is made exclusively from Swakelok components, including various taps, a pressure gauge, and a large-volume stainless steel flask. The taps integrated into the pressure vessel were trivalent in design to allow 1) a complete isolation of the gas phase products 2) a direct outlet to a GC-BID, and 3) a separate gas flask to increase the volume of the pressure vessel if necessary. The gas collection compartment is connected to the electrolysis cell via short tubing (>10 cm) to minimise the overall free volume available for gas products. Integrated into the working electrode compartment, there are two horizontal plugs in either side for the insertion of a reference electrode and working electrode. The reference electrode plug is custom-made to accommodate a Ag/AgCl reference electrode ($I\varnothing = 6$ mm) with an outer cap used to achieve a liquid-tight seal via O-ring compression. In early electrolysis experiments using this electrolysis cell, copper wire was coiled behind a plate electrode and attached via double-sided copper tape – this was then adhered to the cell in position A (red) and the copper wire was fed through a rubber gasket sealing the working electrode plug. The positioning of the working electrode was then moved to position B (green) to achieve a more even current distribution throughout the system. It is important to note that the copper wire connecting the working electrode to the potentiostat is plastic-coated, except for the bare ends at the connection points, ensuring isolation from the electrolyte. The counter compartment solely housed the counter electrode port, integrated into the upper face. The electrode fits loosely within the port to avoid any internal pressure increase from the evolution of oxygen in the counter compartment. Finally, a Nafion membrane was placed between both the working and counter compartments with a rubber gasket on either side to create an airtight seal once the components were assembled.

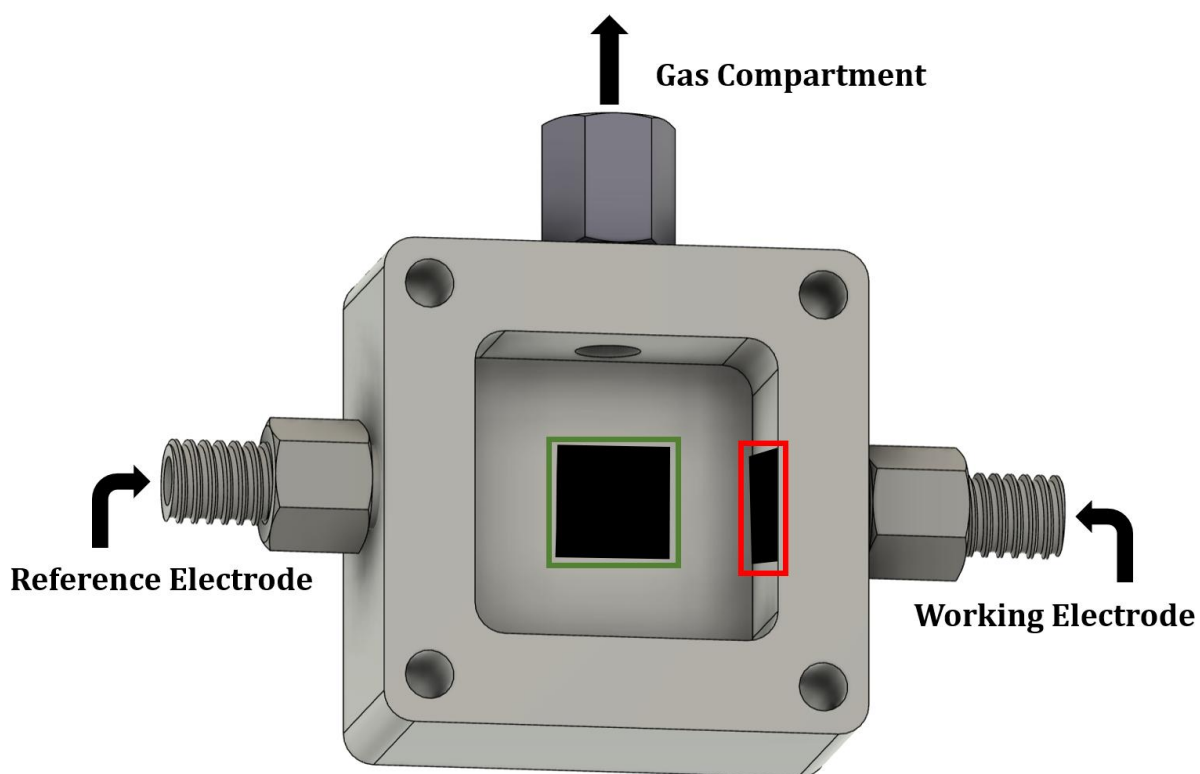


Figure 5.7 - 3D render of working compartment open view with electrode positions a) side-mounted [red] b) back-mounted [green] modelled in Fusion360

5.3.2.3.1 Support Bracket

Following comprehensive testing of the ZHEC1, a bowing of the Nafion membrane was observed due to the increased pressure of the working electrode compartment following electrolysis. It is important to prevent the bowing of the separating membrane first because this will put unnecessary strain on the membrane and ultimately lead to tearing or puncturing. Secondly, due to the outward bowing of the Nafion membrane, the working compartment will undergo an undetermined increase in volume, invalidating gas molarity calculations and thus giving inaccurate catalyst evaluation. A support bracket was designed and prototyped to prevent outward bowing of the Nafion membrane, which was housed in the counter-electrode compartment. The support bracket was designed to evenly distribute support across the membrane to avoid a localisation of pressure, potentially leading to a tear or puncturing. It was also important to design a support bracket which wouldn't significantly affect the internal volume of the counter compartment or impede the transport of ions through the membrane. Taking these factors into account, a minimally invasive support bracket, shown in Figure 5.8, was additively

manufactured via SLA printing using a photopolymer resin. The photocuring resin was selected for its rigidity, chemical resistance, and optical clarity.

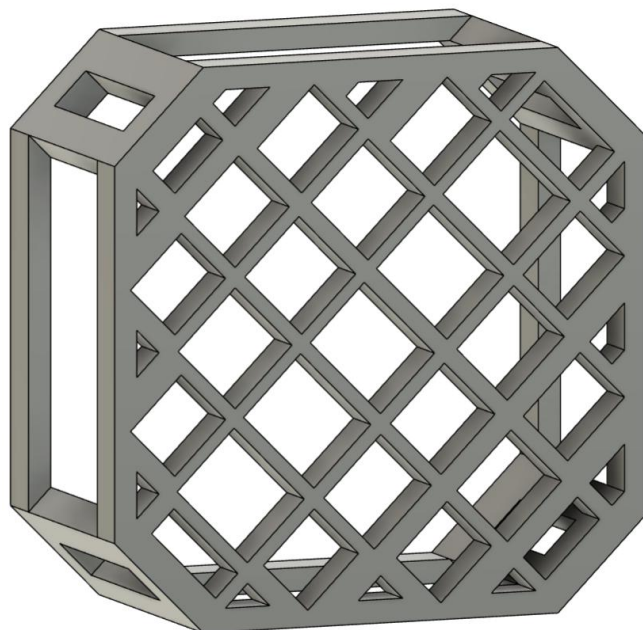


Figure 5.8 - 3D render of a photopolymer resin printed support bracket modelled in Fusion360

5.3.2.4 Design Iteration 3. - Zero-Headspace Collection Vessel 2 (ZHEC2)

The most recent and final iteration of the Zero Headspace Electrochemical Cell (ZHEC2) incorporates key design features from both the DCV and ZHEC1. This design has been engineered to directly attach the gas compartment to the liquid compartment vertically, taking inspiration from the DCV. When sampling, this will reduce the dead volume in the cell by removing the plastic gas tubing, providing fewer opportunities for any gas products to leak from the cell.

During sampling, the sampling interface between the GC and ZHEC1 contained small amounts of air, which would often be retained in the sampling loop should an inadequate volume of gas sample be pushed through the loop. The improved ZHEC2 design features a combination of Swagelok taps on the outlet to allow a CO₂ cylinder to be fitted, which can then sparge the outlet with CO₂ prior to sample submission. Due to the sparging CO₂ exiting via the GC sample loop, this ensures that the GC sample loop is also purged of any air and residual sample potentially retained in the loop. Finally, the additional outlet taps also allow a known volume of CO₂ to be

pushed into the sample vessel to achieve a desired overpressure should the generated gas inside the vessel be of an inadequate volume to fill the sample loop.

The addition of a negative pressure gauge allows us to achieve a complete vacuum within the vessel, specifically to achieve full product quantification.

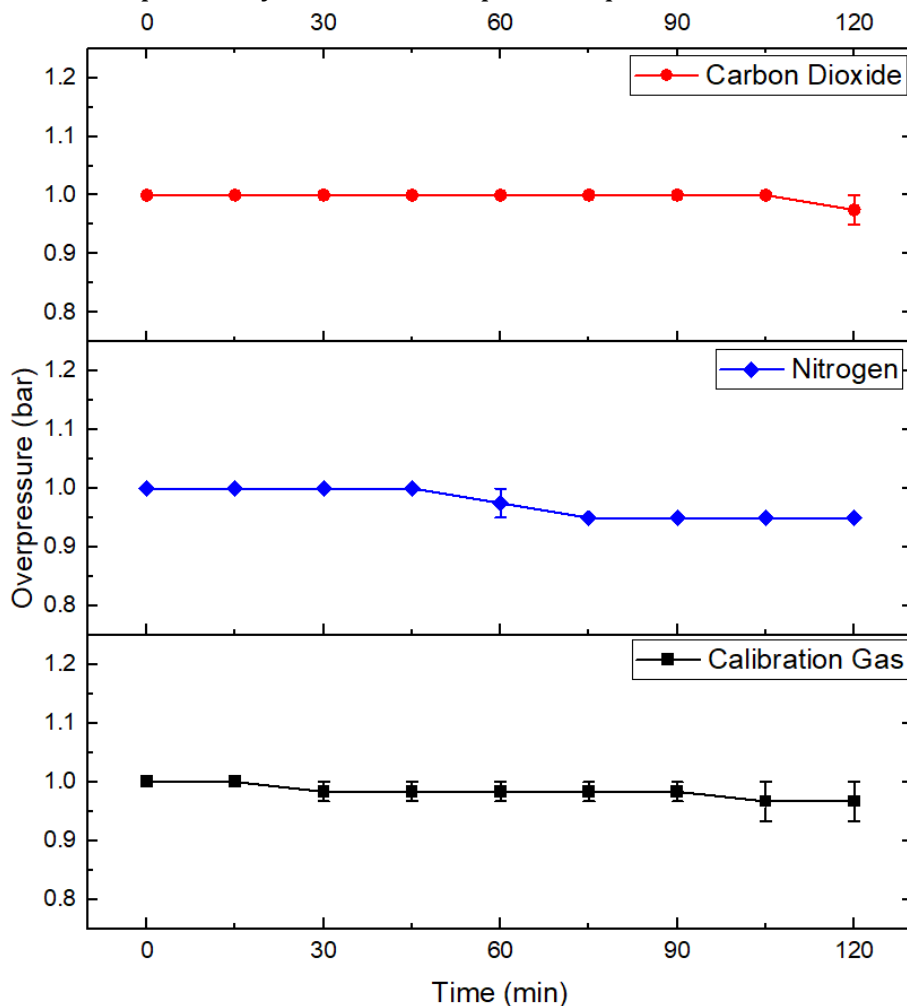


Figure 5.9 – Gas-tightness calibration of ZHEC2 over 120 minutes using i) carbon dioxide ii) nitrogen ii) calibration gas

To ensure the complete gas-tightness of the vessel, multiple gases were used to pressurise the vessel to 1 bar above atmospheric pressure and the internal pressure was monitored over the course of 2 hours, with readings taken every 15 minutes. The figure below details the total internal overpressure recorded over the 2-hour duration.

5.3.2.4.1 ZHEC 2 Operation

1. Firstly, attach the working electrode to position A of the working compartment and feed the connecting wire through a rubber gasket exiting

from the working electrode inlet and tighten to thumb-tightness. Insert the reference electrode in the opposite facing reference electrode inlet and tighten to thumb-tightness.

2. Insert the 4 x main bolts through the back of the working compartment and lay down the vessel facing upwards (pressure gauge facing up). Place the Nafion membrane between two rubber gaskets with central cutouts and slide these onto the upwards facing bolts. Insert the support bracket into the counter compartment and finally slide these onto the bolts. Affix the washers and nuts to the screws and tighten all 4, working in an 'X' pattern – this tightening process is repeated to ensure all 4 corners of the vessel are of equal tightness.
3. The working compartment is filled with CO₂ saturated electrolyte via needle insertion into the working electrode rubber gasket. CO₂ is then bubbled through the electrolyte via needle insertion, ensuring the flow is not too high that the electrolyte is forced into the Swagelok pressure fitting. The purging CO₂ is outlet through all Swagelok components before all taps are closed and the CO₂ inlet is removed, ensuring the Swagelok fittings contain only CO₂ at ambient pressure.
4. The counter compartment is then filled with CO₂ saturated electrolyte and the counter electrode is placed loosely in the counter electrode inlet to ensure there is no pressure increase in this compartment.

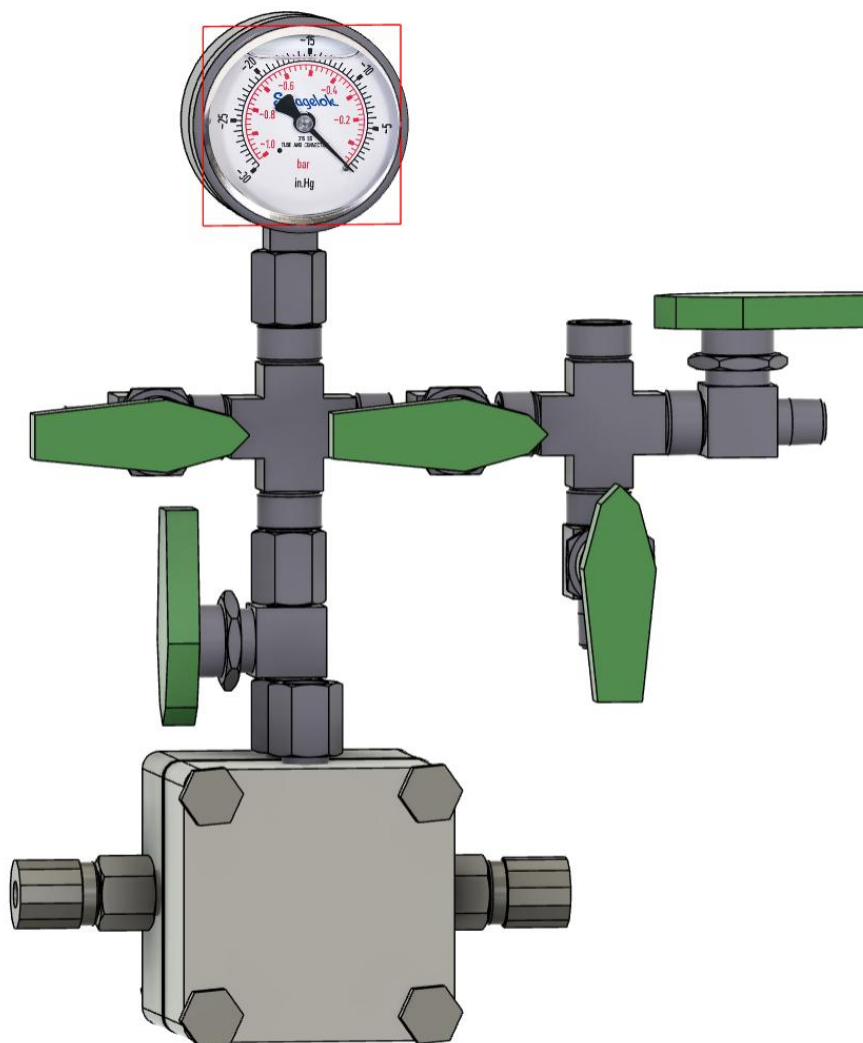


Figure 5.10 - 3D render of ZHEC2 modelled in Fusion360

5. The central tap is opened for the electrolysis to begin. As gas is evolved during the reaction, the internal pressure may increase and can be monitored via the internal pressure gauge.
6. Upon completion of the reaction, the cell can be sonicated to promote any dissolved gasses to release from the solution.

5.4.2.5 Preliminary Batch Electrolysis Testing

MXene - $\text{Ti}_3\text{C}_2\text{T}_x^{\text{NB}}$

To commence preliminary testing of the practical application of the ZHEC2, identical batch electrolysis experiments were conducted in the classic glass H-cell and in the newly designed ZHEC2 using MXene/Nafion-modified Sigracell electrodes. A potential of -1.8 V (vs Ag/AgCl) was chosen for initial testing as this negative potential

is likely to promote the hydrogen evolution reaction. Notably, the pressure gauge integrated into the ZHEC2 indicated an overpressure of 0.9 bar following electrolysis.

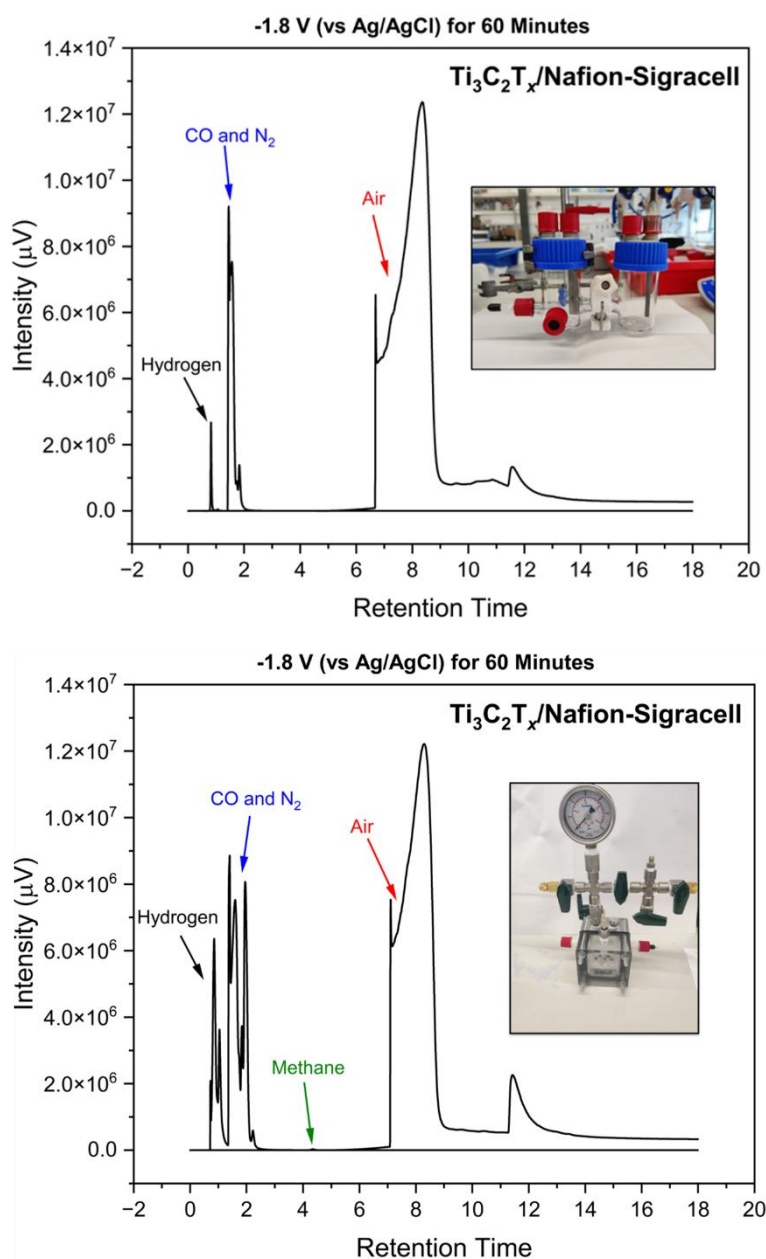


Figure 5.11 - Gas chromatograms for CO₂RR at -1.8 V (Ag/AgCl) for 60 minutes on a Ti₃C₂T_x/Nafion-modified sigracell electrode using a) top - Glass electrolysis cell [Inset] - Image of a traditional electrolysis H-cell. b) bottom - ZHEC2 [Inset] - Image of fully assembled ZHEC2

The resulting chromatograms have been presented in Figure 5.11. Firstly, considering the glass H-cell chromatograms, the predominant non-gaussian peak at a 6 - 10-minute retention time is attributed to the presence of air within the sample loop. This may be introduced at various points in the electrolysis including at the outset due to an insufficient purging of the cell, during sampling via gas-tight

syringe, or during sample injection. Notably, the peak height and area are not representative of the amount of air within the sample, as previous testing indicates this to be the upper detection limit of air. A peak for hydrogen is observed at around a 50-second retention time with an integrated peak area of 99,077 $\mu\text{V}/\text{min}$. Finally, a third region of peaks is identified between 1-3 minutes, correlating to CO and N_2 , further optimisation of the gas chromatographic method would allow the deconvolution of these peaks and their subsequent quantification.

In contrast, when observing the gas chromatogram presented for the ZHEC2, an identical air peak is observed between 6 and 10 minutes, indicating that the limit of detection for air has been reached. Due to extensive testing of the ZHEC2 prior to electrolysis, it is probable that the air is introduced into the GC during the sample submission stage, potentially via the GC inlet connections. Further optimisation of the sample submission will identify the source of air and implement measures to mitigate it. Interestingly, both the hydrogen peak and $\text{CO}_2 + \text{N}_2$ peak region have significantly higher peak areas suggesting a higher retention rate of the gaseous products. With hydrogen being the most challenging gas product to retain, an increase in peak area from 99,077 $\mu\text{V}/\text{min}$ to 1,201,770 $\mu\text{V}/\text{min}$ suggests a drastically higher retention rate for hydrogen. Finally, a final peak is identified in the ZHEC2 chromatograms at

While optimisations must be made to the system before any accurate gas quantification data can be obtained, the results reported herein provide solid justification for the newly designed ZHEC2 and its implemented features.

5.4 Conclusions

This chapter presented the rational design of a 3-electrode cell for the electrochemical evaluation of MXenes. Considerations were made to mitigate the complications of MXene electrochemistry outlined in Chapter 4, with a focus on the inversion of the working electrode to be facing upwards, thus mitigating the effects of gravity on the catalytic film. In addition, the newly designed 3EC allows the evaluation of modified electrodes with various geometries, with a glassy carbon plate being of particular interest due to its relevance to CO_2RR and this body of work.

The design, manufacture, and testing of a bespoke batch CO₂RR electrochemical cell was detailed herein. Multiple iterations were designed, tested, and optimised to achieve a final design capable of facilitating CO₂RR, capturing reaction products, and allowing facile sample submission. The inclusion of a pressure gauge in the cathodic compartment allows for the accurate quantification of gas-phase products. Finally, following comprehensive leak testing, the electrochemical cell was deemed capable of retaining evolved gases including hydrogen following electrolysis.

Only through intelligent reactor design can accurate CO₂RR catalyst evaluation be facilitated. The cells designed, prototyped, and evaluated herein provide a solid foundation for future studies on the complete quantification of CO₂RR reaction products.

6 Conclusions

6.1 Summary

To conclude, the electrochemical reduction of CO₂ (eCO₂RR) is a promising technology for mitigating climate change and producing value-added chemicals, thus closing the carbon cycle. However, the implementation of technology within a laboratory, and consequentially in industry, faces significant challenges. Currently, copper is the most widely reported eCO₂RR catalyst, boasting exceedingly high conversion rates, however, the range of products cu-based catalysts reportedly produce affords significant identification and separation challenges. To this end, the development of highly active, selective, and stable catalysts is crucial in achieving a commercially viable and scalable CO₂ reduction technology. Herein, Ti₃C₂T_x MXene has been extensively evaluated for its applications within efficient electrochemical CO₂RR technology, with a particular focus on the utilisation of commercial MXene powders. In addition, classic electrochemical cells have been optimised to tackle significant challenges associated with CO₂RR product analysis.

The introduction to the synthesis of MXene materials and their precursor MAX phases in Chapter 4 highlights the importance of high-purity MAX Phases and MXenes for electrochemical applications. The etching of Ti₃AlC₂ to Ti₃C₂T_x or Ti₃C₂T_{0,OH} was demonstrated via separate MXene etchants, using LiF + HCl, and NaOH respectively. Despite a successful synthesis, the resulting MXene purity was insufficient for electrochemical applications, thus highlighting the need for a direct HF etching. To avoid the handling of HF, a commercial Ti₃C₂T_x powder was procured and successfully ozone-treated to yield an increase in desired -O and -OH surface terminations, reportedly beneficial for CO₂RR.

Due to recent drastic reductions in the cost of commercial MXene samples, Chapter 5 details the handling and delamination of $\text{Ti}_3\text{C}_2\text{T}_x$ powder with a focus on the fabrication of MXene-based electrodes for eCO_2RR . Traditional methods for catalytic electrode manufacture were ineffective using the powder MXene, thus the fabrication of a $\text{Ti}_3\text{C}_2\text{T}_x$ composite electrode was reported via the electropolymerisation of EDOT. The resulting electrode showed excellent stability in aqueous conditions.

Next, inherent challenges associated with CO_2RR product quantification were tackled via the intelligent redesign of traditional electrochemical cells. A redesigned standard 3-electrode electrochemical cell afforded the inclusion of electrodes with varying morphologies while precisely controlling the exposed surface area. Additionally, the redesign of the classic electrochemical H-cell afforded the inclusion of a pressure gauge. Only by knowing the internal pressure of a reactor can accurate product quantification be achieved. The inclusion of a pressure gauge within a batch electrolysis reactor is exceedingly uncommon yet significant in CO_2RR applications. The manufactured cell was effective in retaining a gas mixture, including hydrogen which is notorious for leaking through fixtures and fittings thus depressurising reactors.

6.2 Retrospectives

In retrospect, this research has provided valuable insight into the handling, modification, and utilisation of powder $\text{Ti}_3\text{C}_2\text{T}_x$ MXene samples, highlighting the inherent challenges and promising solutions for applications within aqueous electrocatalysis.

The successful ozone treatment of a drop-cast $\text{Ti}_3\text{C}_2\text{T}_x$ electrode from a commercial powder is a significant finding in the context of electrocatalysis as the computationally rich literature identifies $-\text{O}$ and $-\text{OH}$ as terminations of great catalytic potential. The dry-ozone treatment of a commercial $\text{Ti}_3\text{C}_2\text{T}_x$ powder shows no evidence of surface oxidation, a process which is often observed when using aqueous acidic and alkaline chemical treatments for surface functionalisation.

Additionally, the fabrication of a $\text{Ti}_3\text{C}_2\text{T}_x$ /PEDOT-modified electrode from MXene powder is significant for the electrochemical evaluation of $\text{Ti}_3\text{C}_2\text{T}_x$. While the

stability of $\text{Ti}_3\text{C}_2\text{T}_x$ -modified electrodes from MXene powders has been demonstrated to be significantly challenging, the simple fabrication technique reported herein can be utilised for the rapid evaluation of $\text{Ti}_3\text{C}_2\text{T}_x$ for a range of aqueous applications.

Due to limitations experienced with CO_2RR product analysis, namely the appearance of split peaks in GC-BID chromatograms, the end goal of evaluating the CO_2RR activity of $\text{Ti}_3\text{C}_2\text{T}_x$ and its subsequent modified electrodes was regrettably not achieved. Additionally, the procurement of an HF-etched commercial MXene sample in June 2023 did not afford the time required to fully evaluate the sample and compare it to LiF + HCl-etched $\text{Ti}_3\text{C}_2\text{T}_x$ powder.

The current electrochemical literature for $\text{Ti}_3\text{C}_2\text{T}_x$ has a significant focus on dry applications, such as supercapacitors and solid-state batteries. While there are several reports highlighting $\text{Ti}_3\text{C}_2\text{T}_x$ as a promising material for electrocatalysis, the overwhelming majority are computationally founded, with few reports detailing the extensive experimental evaluation of $\text{Ti}_3\text{C}_2\text{T}_x$ as a catalyst in aqueous media. When considering those few reports, in almost all cases, the MXenes reported are synthesised by the authors and used directly following synthesis. Several papers have highlighted the stark contrast in behaviour, especially regarding delamination, between freshly synthesised MXenes and MXene powders, including those commercially available. With recent price decreases, MXenes have now become more accessible than ever before, which will likely lead to a surge in the popularity of commercial MXene offerings. This means that the comprehensive evaluation of commercial samples is of paramount importance for informing the future of MXene developments.

6.3 Future Work

While this study has provided valuable insight into the fabrication of $\text{Ti}_3\text{C}_2\text{T}_x$ -modified electrodes from powder MXenes, the further optimisation of the methods detailed herein would work towards achieving highly active and selective MXene-based electrocatalysts.

Due to the drastically reduced cost in MXene materials over the course of this work, it would be advantageous to utilise commercially available samples for future testing

and development. However, should the optimisation of the in-situ HF etching of Ti_3C_2 be necessary in future studies, it would be recommended that the precursor MAX phase particles be of significant, uniform size.¹⁸³ As oxidation of a MXene typically occurs at the edge plane of the flake, utilising larger MAX phase particles would increase the size of the resulting MXene flakes, thus reducing the number of edges, presenting less opportunity for oxidation.¹⁷³ Alternatively, should a fluorine-free synthesis be necessary, a key engineering challenge must be met in the design of a chemically resistant alkaline reactor with an internal pressure gauge. While the PPL liner used in this work was stable under the harsh reaction conditions, engineering a corrosion resistant reactor system, with an internal pressure gauge, would allow conformation that the high pressure necessary for the etching was maintained throughout the reaction.

When attempting to surface functionalise a Ti_3C_2 powder, a drastic increase in -O and -OH terminations was achieved in addition to a reduction in -Cl and -F terminations. Despite this success, the specific quantification of these surface terminations is yet to be evaluated and would be advantageous in fully characterising the surface chemistry of the Ti_3C_2 MXene. The optimisation of surface functionalisation treatments, achieving a near complete surface of oxygen-containing functional groups while preserving the MXene structure, could achieve an unprecedented number of active sites capable of catalysing CO_2RR .

While the incorporation of Ti_3C_2 in an electropolymerized matrix was achieved, the optimisation of these experimental parameters would allow a complete control over the thickness and porosity of the resulting film EPOL film.¹⁷¹ Additionally, the incorporation of PSS (polystyrene sulfonate) into the PEDOT film would act as a counter-ion, thus enhancing the stability and conductivity of the electropolymerised film.⁴ Finally, the MXene-incorporated film must be assessed for its stability under various reaction conditions in order to be deemed suitable for CO_2RR evaluation.

Regarding cell design, further development and optimisation of the ZHEC2 is necessary for implementation into traditional batch CO_2RR set-ups. While the gas-tightness calibrations of the ZHEC2 proved effective for a mixture of gases, air peaks present in the gas-chromatographs indicate that the initial gas purging and/or sample submission is ineffective in restricting air from the system. This would be a

significant challenge to overcome, potentially via a redesign of the purging inlets and outlets, but would be necessary for complete gas quantification. Once this system is optimised, the benchmarking of a known copper catalyst should be conducted prior to the evaluation of novel electrodes. While the implementation of the working electrode is currently effective, the system does not allow a rapid exchange of working electrodes and instead requires the system to be drained and disassembled. To address this, a redesign of the working compartment to accommodate a working electrode window and backplate, similar to that used in the redesigned 3-electrode cell, would allow a rapid exchange of working electrode without the necessity of a fully system disassembly.

Finally, should efforts be made to action those optimisations detailed herein, the ultimate end-goal of this work would be to evaluate a fully -O and -OH terminated MXene/PEDOT:PSS electrode in a ZHEC2 facilitated batch CO₂RR electrolysis.

Ultimately, the drastic price reduction of commercial MXene powders affords many more researchers the opportunity to evaluate MXenes without the high costs previously associated with them. Due to their lower cost, MXenes can also be more readily explored for more innovative applications where cost restrictions were previously inhibiting their advancements.

References

- 1 C. D. Keeling, S. C. Piper, R. B. Bacastow, M. Wahlen, T. P. Whorf, M. Heimann and H. A. Meijer, in *Scripps Institution of Oceanography*, San Diego, 2001.
- 2 United Nations Framework Convention on Climate Change, *Paris Agreement*, 2015. <https://unfccc.int> (accessed 12 August 2024)
- 3 J. Jung, Y. S. Jeong, Y. Lim, C. S. Lee and C. Han, in *Energy Procedia*, Elsevier Ltd, 2013, vol. 37, pp. 1778–1784.
- 4 Dina G. Boer, Jort Langerak, and Paolo P. Pescarmona *ACS Applied Energy Materials* 2023 6 (5), 2634-2656
- 5 A. A. Abd, M. R. Othman and J. Kim, *Environmental Science and Pollution Research*, 2021, **28**, 43329–43364.
- 6 J. Hong, W. Zhang, J. Ren and R. Xu, *Anal. Methods*, 2013, **5**, 1086–1097.
- 7 S. Wang, M. Xu, T. Peng, C. Zhang, T. Li, I. Hussain, J. Wang and B. Tan, *Nat. Commun.*, 2019, 10.
- 8 V. P. Indrakanti, J. D. Kubicki and H. H. Schobert, *Energy Environ Sci*, 2009, **2**, 745–758.
- 9 T. Inoue, A. Fujishima, S. Konishi and K. Honda, *Nature*, 1979, **277**, 637–638.
- 10 Y. Chen, D. Wang, X. Deng and Z. Li, *Catal Sci Technol*, 2017, **7**, 4893–4904.
- 11 K. Sun, Y. Qian and H.-L. Jiang, *Angewandte Chemie International Edition*, 2023, **62**, e202217565.
- 12 P. Xia, B. Zhu, J. Yu, S. Cao and M. Jaroniec, *J Mater Chem A Mater*, 2017, **5**, 3230–3238.
- 13 A. M. Sadanandan, J.-H. Yang, V. Devtade, G. Singh, N. Panangattu Dharmarajan, M. Fawaz, J. Mee Lee, E. Tavakkoli, C.-H. Jeon, P. Kumar and A. Vinu, *Prog Mater Sci*, 2024, **142**, 101242.
- 14 J. Wu, Y. Huang, W. Ye and Y. Li, *Adv. Sci.*, 2017, 4, 1700194.
- 15 S. Gorthy, S. Verma, N. Sinha, S. Shetty, H. Nguyen and M. Neurock, *ACS Catal*, 2023, **13**, 12924–12940.
- 16 D. Pabsch, C. Held and G. Sadowski, *J Chem Eng Data*, 2020, **65**, 5768–5777.
- 17 L. B. T. de Kam, T. L. Maier and K. Krischer, *Electrochim Acta*, 2024, **497**, 144530.
- 18 Y. Tomita, S. Teruya, O. Koga and Y. Hori, *J Electrochem Soc*, 2000, **147**, 4164.
- 19 C. Deacon-Price, A. H. M. da Silva, C. S. Santana, M. T. M. Koper and A. C. Garcia, *The Journal of Physical Chemistry C*, 2023, **127**, 14518–14527.
- 20 M. Ding, Z. Chen, C. Liu, Y. Wang, C. Li, X. Li, T. Zheng, Q. Jiang and C. Xia, *Materials Reports: Energy*, 2023, **3**, 100175.

- 21 R. V. Mom, L. E. Sandoval-Diaz, D. Gao, C. H. Chuang, E. A. Carbonio, T. E. Jones, R. Arrigo, D. Ivanov, M. Hävecker, B. Roldan Cuenya, R. Schlögl, T. Lunkenbein, A. Knop-Gericke and J. J. Velasco-Vélez, *ACS Appl Mater Interfaces*, 2023, **15**, 30052–30059.
- 22 B.-X. Dong, S.-L. Qian, F.-Y. Bu, Y.-C. Wu, L.-G. Feng, Y.-L. Teng, W.-L. Liu and Z.-W. Li, *ACS Appl Energy Mater*, 2018, **1**, 4662–4669.
- 23 Z. Xin, Y.-R. Wang, Y. Chen, W.-L. Li, L.-Z. Dong and Y.-Q. Lan, *Nano Energy*, 2020, **67**, 104233.
- 24 N. Kornienko, Y. Zhao, C. S. Kley, C. Zhu, D. Kim, S. Lin, C. J. Chang, O. M. Yaghi and P. Yang, *J Am Chem Soc*, 2015, **137**, 14129–14135.
- 25 N. Zhang, X. Zhang, L. Tao, P. Jiang, C. Ye, R. Lin, Z. Huang, A. Li, D. Pang, H. Yan, Y. Wang, P. Xu, S. An, Q. Zhang, L. Liu, S. Du, X. Han, D. Wang and Y. Li, *Angewandte Chemie International Edition*, 2021, **60**, 6170–6176.
- 26 N. Han, Y. Wang, L. Ma, J. Wen, J. Li, H. Zheng, K. Nie, X. Wang, F. Zhao, Y. Li, J. Fan, J. Zhong, T. Wu, D. J. Miller, J. Lu, S.-T. Lee and Y. Li, *Chem*, 2017, **3**, 652–664.
- 27 K. Sun, Y. Ji, Y. Liu and Z. Wang, *J Mater Chem A Mater*, 2020, **8**, 12291–12295.
- 28 H. Xie, Y. Wan, X. Wang, J. Liang, G. Lu, T. Wang, G. Chai, N. M. Adli, C. Priest, Y. Huang, G. Wu and Q. Li, *Appl Catal B*, 2021, **289**, 119783.
- 29 L. Wan, X. Zhang, J. Cheng, R. Chen, L. Wu, J. Shi and J. Luo, *ACS Catal*, 2022, **12**, 2741–2748.
- 30 Z. Wu, H. Wu, W. Cai, Z. Wen, B. Jia, L. Wang, W. Jin and T. Ma, *Angewandte Chemie - International Edition*, 2021, **60**, 12554–12559.
- 31 G. Wen, D. U. Lee, B. Ren, F. M. Hassan, G. Jiang, Z. P. Cano, J. Gostick, E. Croiset, Z. Bai, L. Yang and Z. Chen, *Adv Energy Mater*, 2018, **8**, 1802427.
- 32 X. Mei and W. Xu, *iScience*, 2023, **26**, 108499.
- 33 M.-D. Zhang, D.-H. Si, J.-D. Yi, S.-S. Zhao, Y.-B. Huang and R. Cao, *Small*, 2020, **16**, 2005254.
- 34 Q. Miao, C. Lu, Q. Xu, S. Yang, M. Liu, S. Liu, C. Yu, X. Zhuang, Z. Jiang and G. Zeng, *Chemical Engineering Journal*, 2022, **450**, 138427.
- 35 M. Asadi, K. Kim, C. Liu, A. V. Addepalli, P. Abbasi, P. Yasaei, P. Phillips, A. Behranginia, J. M. Cerrato, R. Haasch, P. Zapol, B. Kumar, R. F. Klie, J. Abiade, L. A. Curtiss and A. Salehi-Khojin, *Science (1979)*, 2016, **353**, 467–470.
- 36 L. Verger, V. Natu, M. Carey and M. W. Barsoum, *Trends Chem*, 2019, **1**, 656–669.
- 37 J. L. Hart, K. Hantanasirisakul, A. C. Lang, B. Anasori, D. Pinto, Y. Pivak, J. T. van Omme, S. J. May, Y. Gogotsi and M. L. Taheri, *Nat. Commun.*, 2019, **10**.
- 38 M. Pogorelov, K. Smyrnova, S. Kyrylenko, O. Gogotsi, V. Zahorodna and A. Pogrebnjak, *Nanomaterials*, 2021, **11**, 3412.

- 39 M. Khazaei, A. Ranjbar, M. Arai, T. Sasaki and S. Yunoki, *J. Mater. Chem. C*, 2017, **5**, 2488–2503.
- 40 W. Jeitschko, H. Nowotny and F. Benesovsky, *Monatshefte für Chemie und verwandte Teile anderer Wissenschaften*, 1963, **94**, 844–850.
- 41 M. W. Barsoum, L. Farber, I. Levin, A. Procopio, T. El-Raghy and A. Berner, *Journal of the American Ceramic Society*, 1999, **82**, 2545–2547.
- 42 M. Dahlgqvist, M. W. Barsoum and J. Rosen, *Materials Today*, 2024, **72**, 1–24.
- 43 P. Eklund, M. Beckers, U. Jansson, H. Högberg and L. Hultman, *Thin Solid Films*, 2010, **518**, 1851–1878.
- 44 L. Fu and W. Xia, *Advanced Engineering Materials*, 2021, **23**.
- 45 R. Benitez, W. H. Kan, H. Gao, M. O’Neal, G. Proust and M. Radovic, *Acta Mater*, 2016, **105**, 294–305.
- 46 B. Anasori, M. Dahlgqvist, J. Halim, E. J. Moon, J. Lu, B. C. Hosler, E. N. Caspi, S. J. May, L. Hultman, P. Eklund, J. Rosén and M. W. Barsoum, *J Appl Phys*, 2015, **118**, 094304.
- 47 V. Desai, A. Shrivastava, A. Zala, T. Parekh, S. Gupta and N. I. Jamnapara, *Vacuum*, 2023, **214**, 112221.
- 48 M. Naguib, M. Kurtoglu, V. Presser, J. Lu, J. Niu, M. Heon, L. Hultman, Y. Gogotsi and M. W. Barsoum, *Advanced Materials*, 2011, **23**, 4248–4253.
- 49 M. Naguib, O. Mashtalir, J. Carle, V. Presser, J. Lu, L. Hultman, Y. Gogotsi and M. W. Barsoum, *ACS Nano*, 2012, **6**, 1322–1331.
- 50 K. S. Novoselov, A. K. Geim, S. V. Morozov, D. Jiang, Y. Zhang, S. V. Dubonos, I. V. Grigorieva and A. A. Firsov, *Science (1979)*, 2004, **306**, 1–12.
- 51 The Royal Swedish Academy of Sciences, *The Nobel Prize in Physics 2010*, 2010. <https://www.nobelprize.org/prizes/physics/2010/press-release>, (accessed 14th August 2024)
- 52 Y. Gogotsi and B. Anasori, *ACS Nano*, 2019, **13**, 8491–8494.
- 53 M. Pahlevaninezhad, R. Sadri, D. Momodu, K. Eisawi, M. Pahlevani, M. Naguib and E. P. L. Roberts, *Batter Supercaps*, 2024
- 54 F. Liu, A. Zhou, J. Chen, J. Jia, W. Zhou, L. Wang and Q. Hu, *Appl Surf Sci*, 2017, **416**, 781–789.
- 55 M. Ghidui, M. R. Lukatskaya, M.-Q. Zhao, Y. Gogotsi and M. W. Barsoum, *Nature*, 2014, **516**, 78–81.
- 56 M. Alhabeib, K. Maleski, B. Anasori, P. Lelyukh, L. Clark, S. Sin and Y. Gogotsi, *Chemistry of Materials*, 2017, **29**, 7633–7644.
- 57 K. Arole, J. W. Blivin, S. Saha, D. E. Holta, X. Zhao, A. Sarmah, H. Cao, M. Radovic, J. L. Lutkenhaus and M. J. Green, *iScience*, 2021, **24**, 103403.
- 58 L. Liu, M. Orbay, S. Luo, S. Duluard, H. Shao, J. Harmel, P. Rozier, P. L. Taberna and P. Simon, *ACS Nano*, 2022, **16**, 111–118.

- 59 Y. Li, H. Shao, Z. Lin, J. Lu, L. Liu, B. Duployer, P. O. Å. Persson, P. Eklund, L. Hultman, M. Li, K. Chen, X. H. Zha, S. Du, P. Rozier, Z. Chai, E. Raymundo-Piñero, P. L. Taberna, P. Simon and Q. Huang, *Nat Mater*, 2020, **19**, 894–899.
- 60 P. Zhang, X. Nan, K. Wang, Y. Wang, T. Wang, C. Wang, J. Guo, X. Chen and J. Zhu, *J Electrochem Soc*, 2022, **169**, 043506.
- 61 W. Sun, S. A. Shah, Y. Chen, Z. Tan, H. Gao, T. Habib, M. Radovic and M. J. Green, *J Mater Chem A Mater*, 2017, **5**, 21663–21668.
- 62 S. Yang, P. Zhang, F. Wang, A. G. Ricciardulli, M. R. Lohe, P. W. M. Blom and X. Feng, *Angewandte Chemie - International Edition*, 2018, **57**, 15491–15495.
- 63 T. Li, L. Yao, Q. Liu, J. Gu, R. Luo, J. Li, X. Yan, W. Wang, P. Liu, B. Chen, W. Zhang, W. Abbas, R. Naz and D. Zhang, *Angewandte Chemie - International Edition*, 2018, **57**, 6115–6119.
- 64 B. Sarfraz, M. T. Mehran, M. M. Baig, S. R. Naqvi, A. H. Khoja and F. Shahzad, *Int J Energy Res*, 2022, **46**, 10942–10954.
- 65 M. Benchakar, L. Louprias, C. Garnerero, T. Bilyk, C. Morais, C. Canaff, N. Guignard, S. Morisset, H. Pazniak, S. Hurand, P. Chartier, J. Pacaud, V. Mauchamp, M. W. Barsoum, A. Habrioux and S. Célérier, *Appl Surf Sci*, 2020, **530**, 147209.
- 66 S. Munir, A. Rasheed, T. Rasheed, I. Ayman, S. Ajmal, A. Rehman, I. Shakir, P. O. Agboola and M. F. Warsi, *ACS Omega*, 2020, **5**, 26845–26854.
- 67 N. Khatun and S. C. Roy, *Micro and Nanostructures*, 2022, **167**, 207256.
- 68 M. Tahir, *Energy and Fuels*, 2021, **35**, 6807–6822.
- 69 J. E. von Treifeldt, K. L. Firestein, J. F. S. Fernando, C. Zhang, D. P. Siriwardena, C.-E. M. Lewis and D. V. Golberg, *Mater Des*, 2021, **199**, 109403.
- 70 T. Schultz, N. C. Frey, K. Hantanasirisakul, S. Park, S. J. May, V. B. Shenoy, Y. Gogotsi and N. Koch, *Chemistry of Materials*, 2019, **31**, 6590–6597.
- 71 B. Anasori, C. Shi, E. J. Moon, Y. Xie, C. A. Voigt, P. R. C. Kent, S. J. May, S. J. L. Billinge, M. W. Barsoum and Y. Gogotsi, *Nanoscale Horiz*, 2016, **1**, 227–234.
- 72 H. Chen, A. D. Handoko, J. Xiao, X. Feng, Y. Fan, T. Wang, D. Legut, Z. W. Seh and Q. Zhang, *ACS Appl Mater Interfaces*, 2019, **11**, 36571–36579.
- 73 A. D. Handoko, H. Chen, Y. Lum, Q. Zhang, B. Anasori and Z. W. Seh, *iScience*, 2020, **23**, 101181.
- 74 L. Meng, L.-K. Yan, F. Viñes and F. Illas, *J. Mater. Chem. A*, 2024
- 75 V. Parey, B. M. Abraham and J. K. Singh, *Mater Chem Phys*, 2023, **310**, 128444.
- 76 Z. Wei, Z. Peigen, T. Wubian, Q. Xia, Z. Yamei and S. ZhengMing, *Mater Chem Phys*, 2018, **206**, 270–276.
- 77 M. Peng, M. Dong, W. Wei, H. Xu, C. Liu and C. Shen, *Carbon N Y*, 2021, **179**, 400–407.
- 78 S. Shah, I. Mubeen, E. Pervaiz and H. Nasir, *FlatChem*, 2023, **41**, 100544.

- 79 J. Yang, A. Wang, S. Zhang, H. Wu and L. Chen, *Comput Mater Sci*, 2018, **153**, 303–308.
- 80 V. Kamysbayev, A. S. Filatov, H. Hu, X. Rui, F. Lagunas, D. Wang, R. F. Klie and D. V. Talapin, *Science (1979)*, 2020, **369**, 979–983.
- 81 X. Sang, Y. Xie, M.-W. Lin, M. Alhabeab, K. L. Van Aken, Y. Gogotsi, P. R. C. Kent, K. Xiao and R. R. Unocic, *ACS Nano*, 2016, **10**, 9193–9200.
- 82 S. Doo, A. Chae, D. Kim, T. Oh, T. Y. Ko, S. J. Kim, D.-Y. Koh and C. M. Koo, *ACS Appl. Mater. & Interfaces*, 2021, **13**, 22855–22865
- 83 A. Shayesteh Zeraati, S. A. Mirkhani, P. Sun, M. Naguib, P. V Braun and U. Sundararaj, *Nanoscale*, 2021, **13**, 3572–3580.
- 84 A. Lipatov, M. Alhabeab, M. R. Lukatskaya, A. Boson, Y. Gogotsi and A. Sinitskii, *Adv Electron Mater*, 2016, **2**, 1600255.
- 85 A. Lipatov, A. Goad, M. J. Loes, N. S. Vorobeve, J. Abourahma, Y. Gogotsi and A. Sinitskii, *Matter*, 2021, **4**, 1413–1427.
- 86 B. C. Wyatt, A. Rosenkranz and B. Anasori, *Advanced Materials*, 2021, **33**, 2007973.
- 87 M. Shekhirev, C. E. Shuck, A. Sarycheva and Y. Gogotsi, *Prog Mater Sci*, 2021, **120**, 100757.
- 88 Clarivate™ (Web of Science™), <https://www.webofscience.com>, (accessed August 2024)
- 89 Y. Li, S. Vallem and J. Bae, *Current Applied Physics*, 2023, **53**, 142–164.
- 90 H. Wang, M. Ning, M. Sun, B. Li, Y. Liang and Z. Li, *RSC Adv*, 2024, **14**, 26837–26856.
- 91 J. Wen, L. Huang, Y. Huang, W. Luo, H. Huo, Z. Wang, X. Zheng, Z. Wen and Y. Huang, *Energy Storage Mater*, 2022, **45**, 934–940.
- 92 A. Liu, X. Liang, Q. Yang, X. Ren, M. Gao, Y. Yang and T. Ma, *ChemPlusChem*, 2021, **86**, 166–170.
- 93 J. Xia, S.-Z. Yang, B. Wang, P. Wu, I. Popovs, H. Li, S. Irle, S. Dai and H. Zhu, *Nano Energy*, 2020, **72**, 104681.
- 94 Y. Ding, J. Zhang, A. Guan, Q. Wang, S. Li, A. M. Al-Enizi, L. Qian, L. Zhang and G. Zheng, *Nano Conver*, 2021, **8**, 14.
- 95 S. Li, P. Tuo, J. Xie, X. Zhang, J. Xu, J. Bao, B. Pan and Y. Xie, *Nano Energy*, 2018, **47**, 512–518.
- 96 A. D. Handoko, K. D. Fredrickson, B. Anasori, K. W. Convey, L. R. Johnson, Y. Gogotsi, A. Vojvodic and Z. W. Seh, *ACS Appl Energy Mater*, 2018, **1**, 173–180.
- 97 Y. Jiang, T. Sun, X. Xie, W. Jiang, J. Li, B. Tian and C. Su, *ChemSusChem*, 2019, **12**, 1368–1373.
- 98 H. Chen, A. D. Handoko, J. Xiao, X. Feng, Y. Fan, T. Wang, D. Legut, Z. W. Seh and Q. Zhang, *ACS Appl Mater Interfaces*, 2019, **11**, 36571–36579.

- 99 L. Meng, L.-K. Yan, F. Viñes and F. Illas, *J Mater Chem A Mater*, 2024, **12**, 7856–7874.
- 100 Y. Xiao and W. Zhang, *Nanoscale*, 2020, **12**, 7660–7673.
- 101 N. Li, X. Chen, W.-J. Ong, D. R. MacFarlane, X. Zhao, A. K. Cheetham and C. Sun, *ACS Nano*, 2017, **11**, 10825–10833.
- 102 A. D. Handoko, H. Chen, Y. Lum, Q. Zhang, B. Anasori and Z. W. Seh, *iScience*, 2020, **23**, 101181
- 103 S. Popović, M. Smiljanić, P. Jovanović, J. Vavra, R. Buonsanti and N. Hodnik, *Angewandte Chemie International Edition*, 2020, **59**, 14736–14746.
- 104 S. J. Raaijman, N. Arulmozhi and M. T. M. Koper, *ACS Appl Mater Interfaces*, 2021, **13**, 48730–48744.
- 105 S. Lee and J. Lee, *ChemElectroChem*, 2018, **5**, 558–564.
- 106 F. Yang, W. Fang, Q. Wang, P. Deng and B. Y. Xia, *ACS Sustain Chem Eng*, 2022, **10**, 4677–4682.
- 107 J. Huang, N. Hörmann, E. Oveisi, A. Loiudice, G. L. De Gregorio, O. Andreussi, N. Marzari and R. Buonsanti, *Nat Commun*, 2018, **9**, 3117.
- 108 C. F. Holder and R. E. Schaak, *ACS Nano*, 2019, **13**, 7359–7365.
- 109 F. A. Stevie and C. L. Donley, *Journal of Vacuum Science & Technology A*, 2020, **38**, 063204.
- 110 R. R. Jones, D. C. Hooper, L. Zhang, D. Wolverson and V. K. Valev, *Nanoscale Res. Lett.*, 2019, **14**.
- 111 A. Barhoum and M. Luisa García-Betancourt, in *Emerging Applications of Nanoparticles and Architecture Nanostructures*, eds. A. Barhoum and A. S. H. Makhoulouf, Elsevier, 2018, pp. 279–304.
- 112 Y. Wang, W. Bury, D. A. Gómez-Gualdrón, N. A. Vermeulen, J. E. Mondloch, P. Deria, K. Zhang, P. Z. Moghadam, A. A. Sarjeant, R. Q. Snurr, J. F. Stoddart, J. T. Hupp and O. K. Farha, *J Am Chem Soc*, 2015, **137**, 3585–3591.
- 113 R. Bottom, in *Principles and Applications of Thermal Analysis*, 2008, pp. 87–118. ISBN:978-1-405-13171-1
- 114 P. Gabbott, in *Principles and Applications of Thermal Analysis*, 2008, pp. 51–86. ISBN:978-1-405-13171-1
- 115 R. G. Compton and C. E. Banks, *Understanding Voltammetry*, Imperial College Press, 2010. ISBN: 978-1-84816-587-8
- 116 A. J. Bard and L. R. Faulkner, *Electrochemical Methods: Fundamentals and Applications*, Wiley, 2nd edn., 2001. ISBN: 978-0-471-04372-0
- 117 A. B. Littlewood, *Gas chromatography : principles, techniques, and applications*, Academic Press, New York, New York, ; 2nd ed., 1970. ISBN: 978-1483-26098-3

- 118 S. Munir, A. Rasheed, T. Rasheed, I. Ayman, S. Ajmal, A. Rehman, I. Shakir, P. O. Agboola and M. F. Warsi, *ACS Omega*, 2020, **5**, 26845–26854.
- 119 C. Li, S. Kota, C. Hu and M. W. Barsoum, *Journal of Ceramic Science and Technology*, 2016, **7**, 301–306.
- 120 A. Hendaoui, M. Andasmas, A. Amara, A. Benaldjia, P. Langlois and D. Vrel, *International Journal of Self-Propagating High-Temperature Synthesis*, 2008, **17**, 129–135.
- 121 E. Drouelle, V. Brunet, J. Cormier, P. Villechaise, P. Sallot, F. Naimi, F. Bernard and S. Dubois, *Journal of the American Ceramic Society*, 2020, **103**, 1270–1280.
- 122 P. Maughan, Lancaster University, 2020. Doctoral Thesis. doi.org/10.17635/lancaster/thesis/842
- 123 T. Kim and J.-W. Lim, *Journal of the American Ceramic Society*, 2023, **106**, 7311–7321.
- 124 C. Peng, C.-A. Wang, Y. Song and Y. Huang, *Materials Science and Engineering: A*, 2006, **428**, 54–58.
- 125 N. Shahin, A. Heidarpour and S. Kazemi, *Engineering Reports*, 2024, **6**, e12814.
- 126 D.-H. Menz, N. Feltgen, T. Lechner, H. Menz, B.-K. Müller, J. Dresp and H. Hoerauf, *Transl Vis Sci Technol*, 2019, **8**, 24.
- 127 D. K. Horton, M. Orr, T. Tsongas, R. Leiker and V. Kapil, *Disaster Med. Public Health Prep.*, 2008, **2**, 104–113
- 128 M. Özcan, A. Allahbeickaraghi and M. DüNDAR, *Clin Oral Investig*, 2012, **16**, 15–23.
- 129 M. Ghidui, M. R. Lukatskaya, M.-Q. Zhao, Y. Gogotsi and M. W. Barsoum, *Nature*, 2014, **516**, 78–81.
- 130 T. Habib, X. Zhao, S. A. Shah, Y. Chen, W. Sun, H. An, J. L. Lutkenhaus, M. Radovic and M. J. Green, *NPJ 2D Mater. Appl.*, 2019, **3**.
- 131 J. Björk and J. Rosén, *Chemistry of Materials*, 2021, **33**, 9108–9118.
- 132 C. Eames and M. S. Islam, *J Am Chem Soc*, 2014, **136**, 16270–16276.
- 133 C. Peng, C. A. Wang, Y. Song and Y. Huang, *Materials Science and Engineering: A*, 2006, **428**, 54–58.
- 134 D. J. Myers, A. J. Kropf, E. C. Wegener, H. Mistry, N. Kariuki and J. Park, *J Electrochem Soc*, 2021, **168**, 044510.
- 135 A. Z. Taning, S. Lee, S. Woo, S.-H. Park, B. Bae and S.-D. Yim, *J Electrochem Soc*, 2021, **168**, 104506.
- 136 B. A. W. Mowbray, D. J. Dvorak, N. Taherimakhsoosi and C. P. Berlinguette, *Energy & Fuels*, 2021, **35**, 19178–19184.

- 137 Y. Guo, D. Yang, B. Li, D. Yang, P. Ming and C. Zhang, *ACS Appl Mater Interfaces*, 2021, **13**, 27119–27128.
- 138 L. Qin, Q. Tao, A. El Ghazaly, J. Fernandez-Rodriguez, P. O. Å. Persson, J. Rosen and F. Zhang, *Adv Funct Mater*, 2018, **28**, 1703808.
- 139 S. Cho, J. Lim and Y. Seo, *ACS Omega*, 2022, **7**, 37825–37833.
- 140 C. J. Zhang, S. Pinilla, N. McEvoy, C. P. Cullen, B. Anasori, E. Long, S.-H. Park, A. Seral-Ascaso, A. Shmeliov, D. Krishnan, C. Morant, X. Liu, G. S. Duesberg, Y. Gogotsi and V. Nicolosi, *Chemistry of Materials*, 2017, **29**, 4848–4856.
- 141 J. E. Heckler, G. R. Neher, F. Mehmood, D. B. Lioi, R. Pachter, R. Vaia, W. J. Kennedy and D. Nepal, *Langmuir*, 2021, **37**, 5447–5456.
- 142 Q. Qing, X. Shi, S. Hu, L. Li, T. Huang, N. Zhang and Y. Wang, *Langmuir*, 2023, **39**, 9453–9467.
- 143 P. Zhang, L. Wang, Z. Huang, J. Yu, Z. Li, H. Deng, T. Yin, L. Yuan, J. K. Gibson, L. Mei, L. Zheng, H. Wang, Z. Chai and W. Shi, *ACS Appl Mater Interfaces*, 2020, **12**, 15579–15587.
- 144 A. Thakur, N. Chandran B.S., K. Davidson, A. Bedford, H. Fang, Y. Im, V. Kanduri, B. C. Wyatt, S. K. Nemani, V. Poliukhova, R. Kumar, Z. Fakhraai and B. Anasori, *Small Methods*, 2023, **7**, 2300030.
- 145 A. Ashok, S. B. Saseendran and A. Arackal Sukumaran, *ACS Appl Energy Mater*, 2024, **7**, 5050–5063.
- 146 B. Anasori, C. Shi, E. J. Moon, Y. Xie, C. A. Voigt, P. R. C. Kent, S. J. May, S. J. L. Billinge, M. W. Barsoum and Y. Gogotsi, *Nanoscale Horiz.*, 2016, **1**, 227–234.
- 147 S. Seyedin, J. Zhang, K. A. S. Usman, S. Qin, A. M. Glushenkov, E. R. S. Yanza, R. T. Jones and J. M. Razal, *Global Challenges*, 2019, **3**, 1900037.
- 148 K. Maleski, V. N. Mochalin and Y. Gogotsi, *Chemistry of Materials*, 2017, **29**, 1632–1640.
- 149 E. Saita, M. Iwata, Y. Shibata, Y. Matsunaga, R. Suizu, K. Awaga, J. Hirotsu and H. Omachi, *Front. Chem.*, 2022, **10**.
- 150 Z. Zhang, S. Yang, P. Zhang, J. Zhang, G. Chen and X. Feng, *Nat Commun*, 2019, **10**, 2920.
- 151 P. Srimuk, J. Halim, J. Lee, Q. Tao, J. Rosen and V. Presser, *ACS Sustain Chem Eng*, 2018, **6**, 3739–3747.
- 152 Y. Dall'Agnese, M. R. Lukatskaya, K. M. Cook, P.-L. Taberna, Y. Gogotsi and P. Simon, *Electrochem Commun*, 2014, **48**, 118–122.
- 153 X. Wang, S. Kajiyama, H. Iinuma, E. Hosono, S. Oro, I. Moriguchi, M. Okubo and A. Yamada, *Nat Commun*, 2015, **6**, 6544.
- 154 M. Naguib, R. R. Unocic, B. L. Armstrong and J. Nanda, *Dalton Trans.*, 2015, **44**, 9353–9358.
- 155 A. F. Michels, T. Menegotto and F. Horowitz, *Appl. Opt.*, 2004, **43**, 820–823.

- 156 S. Han, J. Derksen and J.-H. Chun, *IEEE Transactions on Semiconductor Manufacturing*, 2004, **17**, 12–21.
- 157 A. Kaliyaraj Selva Kumar and R. G. Compton, *ACS Catal*, 2022, **12**, 4754–4764.
- 158 Z. Wang, R.-M. Latonen, C. Kvarnström, A. Ivaska and L. Niu, *Materials*, 2010, **3**, 672–681.
- 159 I. Brook, G. Mechrez, R. Y. Suckeveriene, R. Tchoudakov, S. Lupo and M. Narkis, *Polym Compos*, 2014, **35**, 788–794.
- 160 A. Kaliyaraj Selva Kumar, Y. Zhang, D. Li and R. G. Compton, *Electrochem commun*, 2020, **121**, 106867.
- 161 J. Zhang, N. Kong, S. Uzun, A. Levitt, S. Seyedin, P. A. Lynch, S. Qin, M. Han, W. Yang, J. Liu, X. Wang, Y. Gogotsi and J. M. Razal, *Advanced Materials*, 2020, **32**, 2001093.
- 162 Y. Wang, X. Wang, B. Ge, J. Guo, C. Fernandez and Q. Peng, *ACS Appl Energy Mater*, 2021, **4**, 9961–9968.
- 163 Z. Ling, C. E. Ren, M.-Q. Zhao, J. Yang, J. M. Giammarco, J. Qiu, M. W. Barsoum and Y. Gogotsi, *Proceedings of the National Academy of Sciences*, 2014, **111**, 16676–16681.
- 164 P. Flouda, A. Inman, M. Gumenna, D. Bukharina, V. V. Shevchenko, Y. Gogotsi and V. V. Tsukruk, *ACS Appl Mater Interfaces*, 2023, **15**, 53776–53785.
- 165 S. Lin, Q. Wu and Y. Lu, *ChemElectroChem*, 2024, **11**, e202300776.
- 166 S. M. Link, M. Scheuble, M. Goll, E. Muks, A. Ruff, A. Hoffmann, T. V. Richter, J. T. Lopez Navarrete, M. C. Ruiz Delgado and S. Ludwigs, *Langmuir*, 2013, **29**, 15463–15473.
- 167 C. Esen, M. Antonietti and B. Kumru, *ChemPhotoChem*, 2021, **5**, 857–862.
- 168 W. Xiao, D. Hu, C. Peng and G. Z. Chen, *ACS Appl Mater Interfaces*, 2011, **3**, 3120–3129.
- 169 N. German, A. Popov, A. Ramanaviciene and A. Ramanavicius, *Nanomaterials*, 2019, **9**, 806.
- 170 E. B. Boz, M. Fritz and A. Forner-Cuenca, *Adv Mater Interfaces*, 2023, **10**, 2202497.
- 171 Y. Seki, M. Takahashi and M. Takashiri, *RSC Adv*, 2019, **9**, 15957–15965.
- 172 D. Jayaprakash, S. Takizawa, T. Arai and H. Sasai, *J Exp Nanosci*, 2006, **1**, 477–510.
- 173 A. Iqbal, J. Hong, T. Y. Ko and C. M. Koo, *Nano Converg.*, 2021, **8**
- 174 S. Jambhulkar, S. Liu, P. Vala, W. Xu, D. Ravichandran, Y. Zhu, K. Bi, Q. Nian, X. Chen and K. Song, *ACS Nano*, 2021, **15**, 12057–12068.
- 175 S. A. Shchukarev and T. A. Tolmacheva, *Journal of Structural Chemistry*, 1968, **9**, 16–21.

- 176 S. Liang, N. Altaf, L. Huang, Y. Gao and Q. Wang, *Journal of CO2 Utilization*, 2020, **35**, 90–105.
- 177 M. Mandal, *ChemElectroChem*, 2021, **8**, 36–45.
- 178 K. C. Poon, W. Y. Wan, H. Su and H. Sato, *RSC Adv.*, 2022, **12**, 22703–22721
- 179 M. Wagner, I. von Harbou, J. Kim, I. Ermatchkova, G. Maurer and H. Hasse, *J Chem Eng Data*, 2013, **58**, 883–895.
- 180 J. S. Diercks, B. Pribyl-Kranewitter, J. Herranz, P. Chauhan, A. Faisnel and T. J. Schmidt, *J Electrochem Soc*, 2021, **168**, 064504.
- 181 J. M. Mora-Hernandez, W. I. González-Suárez, A. Manzo-Robledo and M. Luna-Trujillo, *Journal of CO2 Utilization*, 2021, **47**, 101504.
- 182 E. L. Clark and A. T. Bell, *J Am Chem Soc*, 2018, **140**, 7012–7020.
- 183 A. Lipatov, M. Alhabeab, M. R. Lukatskaya, A. Boson, Y. Gogotsi and A. Sinitskii, *Adv Electron Mater*, 2016, **2**, 1600255.